A Comprehensive Global Modelling Assessment of Nitrate Heterogeneous Formation on Desert Dust

Rubén Soussé Villa[1], Oriol Jorba[1], María Gonçalves Ageitos[1], Dene Bowdalo[1], Marc Guevara[1], and Carlos Pérez García-Pando[1,2]

[1]Barcelona Supercomputing Center, Barcelona, Spain
[2]Catalan Institution for Research and Advanced Studies (ICREA), Barcelona, Spain

Correspondence: Rubén Soussé (ruben.sousse@bsc.es), Oriol Jorba (oriol.jorba@bsc)

Abstract.

Desert dust undergoes complex heterogeneous chemical reactions during atmospheric transport, forming nitrate coatings that ~~impact~~ influences hygroscopicity, gas ~~species~~ partitioning, optical properties, and aerosol radiative forcing. Contemporary atmospheric chemistry models show significant disparities in aerosol nitrogen species due to ~~varied~~ varying parameterizations and inaccuracies in representing heterogeneous chemistry and dust alkalinity. This study investigates key processes in nitrate formation over dust and evaluates their representation in models. We incorporate varying levels of dust heterogeneous chemistry complexity into the MONARCH model, assessing sensitivity to ~~key~~ critical processes. Our analyses ~~focus on~~ address the condensation pathways of gas species onto dust (irreversible and reversible), the influence of nitrate representation on species ~~' burdensand lifetimes,~~ burdens, lifetimes and size distribution, and the ~~alkalinity role~~ role of alkalinity. Using annual global simulations, we compare particulate and gas species surface concentrations against observations, and evaluate global budgets and spatial distributions. Findings show significant outcome dependence on methodology, particularly on ~~the reversible or irreversible condensation of gas species on particles, with a wide range of burdens~~ reversible vs. irreversible gas condensation on dust, with wide ranges for particulate nitrate burdens (0.66 to 1.93 Tg) and correlations with observations (0.66 to 0.91). ~~Particulate ammonium burdens display less~~ In contrast, particulate ammonium burdens show lower variability (0.19 to 0.31 Tg). Incorporating dust ~~and~~ (together with sea-salt~~alkalinity yields results more consistent~~) alkalinity improves consistency with observations, ~~and assuming reversible gas condensation over dust,~~ with reversible condensation along with alkalinity representation ~~, aligns best with observations, while providing~~ yielding the best agreement, while showing consistent gas and particle partitioning. In contrast, irreversible uptake reactions overestimate coarse particulate nitrate formation. Our ~~analysis provides~~ findings offer guidelines for integrating nitrate heterogeneous formation on dust in models, paving the road for improved estimates of aerosol radiative effects.

1 Introduction

Desert dust is produced by wind erosion of arid and semi-arid surfaces, contributing approximately 40% of the total dry aerosol mass globally, and between 70% and 80% if sea-salt aerosol (SS) is not considered (Boucher et al., 2013; Adebiyi and Kok, 2020). Dust interacts with ~~solar radiation(direct climate forcing), affects clouds (indirect climate forcing)~~ shortwave

and longwave radiation, affects cloud formation and alters atmospheric composition, modifying the Earth's energy and water cycles (Pérez et al., 2011; Boucher et al., 2013; Randall et al., 2013). When deposited, dust also affects biogeochemical cycles both on ocean and continental areas (Mahowald et al., 2014; Li et al., 2016; Bergas-Massó et al., 2023). If inhaled, dust can be potentially harmful for animal and human health (Usher et al., 2003). Temporal variations in dust emissions, from interannual to geological time scales, have been a key driver of the past climate of the Earth, as observed in ice cores and ocean sediment samples (Rea, 1994). All these considerations make desert dust particles a key component of the Earth system influencing climate (Semeniuk and Dastoor, 2020).

Climate perturbations by dust depend fundamentally upon dust particles' physical and chemical properties. These properties are mainly the particle size distribution (PSD), shape, surface characteristics, mineral composition, and mixing state (Usher et al., 2003; Riemer et al., 2019). These characteristics depend on the dust source region and on its chemical transformations while transported in the atmosphere (Claquin et al., 1999). These two factors determine the final dust optical properties, and consequently its radiative forcing.

~~Among the factors~~ A particularly significant factor driving the chemical evolution of dust in the atmosphere ~~, heteregeneous reactions —those~~ is *heterogeneous chemistry*: Chemical reactions involving more than one matter phase ~~—are particularly significant (Schwartz, 1986; Dentener et al., 1996; Bauer et al., 2004, 2007; Riemer et al., 2019).~~ (e.g. gas, liquid and solid particles) that might occur in the surfaces of aerosol particles or within their liquid phases (Schwartz, 1986; Dentener et al., 1996; Usher et al., 2003; [illegible]).

For example, the condensation of atmospheric gas species on liquid or solid particles are key for particle growth and changes in optical properties during atmospheric transport (Vlasenko et al., 2009; Fairlie et al., 2010; Karydis et al., 2016). Heterogeneous reactions involving nitrogen, for example, can even cause dust to act as a transport medium of nitrates from nitrate-rich areas to regions downwind of dust sources (Ma et al., 2021).

Heterogeneous reactions mainly occur when dust mixes with anthropogenic pollutants emitted in urban and industrial areas. Nitric acid ($HNO_{3(g)}$), ammonia ($NH_{3(g)}$), sulfur dioxide ($SO_{2(g)}$) and sulfuric acid ($H_2SO_{4(g)}$) are the most important anthropogenic species that react with dust (Usher et al., 2003; Yue et al., 2022). These interactions lead to: 1) the formation of aqueous coatings around the particles (Usher et al., 2003; Krueger et al., 2003, 2004; Fountoukis and Nenes, 2007; Li and Shao, 2009) and 2) the reaction of gases with the non-volatile cations (NVC) present both at the ~~minerals~~particles' surfaces and dissolved in ~~the~~ their liquid envelope (Dentener et al., 1996; Goodman, 2000; Usher et al., 2003; Li and Shao, 2009). These processes transfer mass from the gas to the aerosol phase, either through irreversible reactions of low volatile gas vapors with the bulk material of the particle or reversible condensation-evaporation processes between the gas phase and the liquid coating (Usher et al., 2002, 2003; Krueger et al., 2003; Crowley et al., 2010).

Each gas species' chemical transformation follows a distinct pathway depending on its solubility and reactivity with other atmospheric species dissolved in the particle's liquid coating and with the NVC in dust. Among these, $HNO_{3(g)}$ plays a major role in dust heterogeneous chemistry due to its relatively high solubility and reactivity with ammonium (NH_4^+) from dissolved $NH_{3(g)}$, leading to the formation of ammonium nitrate (NH_4NO_3) (Metzger et al., 2002; Usher et al., 2003). Aqueous $H_2SO_{4(g)}$ is also paramount, competing with dissolved $HNO_{3(g)}$ to neutralize NH_4^+. However, the neutralization by $H_2SO_{4(g)}$

predominates due to its very low vapor pressure, preventing its evaporation back to the gas phase and resulting in the formation of ammonium sulfate ($(NH_4)_2SO_4$) (Usher et al., 2003; Uno et al., 2020). These are the main formation pathways of particulate nitrate (NO_3^-), particulate ammonium (NH_4^+) and particulate sulfate (SO_4^{2-}) from the HNO_3-NH_3-H_2SO_4 neutralization system in the particles' liquid coating. Additionally, $SO_{2(g)}$ is relevant in the aqueous medium as it converts to $H_2SO_{4(g)}$ through oxidation with O_3 and H_2O_2 (Seinfeld and Pandis, 1998; Usher et al., 2002).

The dust minerals also provide additional reactive surfaces to neutralize $HNO_{3(g)}$, with their reactivity depending on their solubility and environmental relative humidity (RH). Under low RH, solid minerals may serve as active sites for reactions with gas species on the particle surfaces (Usher et al., 2003). Conversely, at high RH, minerals can dissociate in the aqueous medium, releasing NVC such as Ca^{2+}, K^+, Mg^{2+} and Na^+. The active sites in dust minerals and NVC play a key role in neutralizing dissolved $HNO_{3(g)}$ and forming NO_3^- compounds (i.e. $Ca(NO_3)_{2(a)}$, $Mg(NO_3)_{2(a)}$, $KNO_{3(a)}$ and $NaNO_{3(a)}$) (Fenter et al., 1995; Krueger et al., 2004). Consequently, these nitrate salts may form on the surface of the dust under low RH or dissociate in the particle's liquid coating (Usher et al., 2003; Jones et al., 2021). These reactions represent the primary pathways for NO_3^- formation in the presence of dust, and are highly sensitive to NO_x and sulfate concentrations (Fenter et al., 1995; Riemer et al., 2003). For instance, the combination of reduced sulfate emissions along with unchanged or even enhanced $NH_{3(g)}$ emissions, as predicted by 21st century emission scenarios, implies a reduction in particle acidity (Bauer et al., 2007; Bellouin et al., 2011; Boucher et al., 2013; Hauglustaine et al., 2014; Bian et al., 2017; Karydis et al., 2021). This scenario, alongside a potential rise in dust (Usher et al., 2002; Adebiyi et al., 2023), would lead to an increase in NO_3^- formation, especially in the fine mode, if NO_x emissions are not concurrently reduced (Bauer et al., 2016; Bian et al., 2017; Zaveri et al., 2021). Therefore, accurate modelling of dust heterogeneous chemistry in atmospheric models is important for present and future air quality control (Myhre et al., 2006).

In the last decades, several approximations have been introduced in atmospheric chemistry models to address nitrate heterogeneous reactions on both dust and SS, with a particular focus on $HNO_{3(g)}$ condensation. These approaches range from ~~the~~ dynamic mass transfer (DMT) calculations between gas and aerosol phases (Meng and Seinfeld, 1996; Lurmann et al., 1997; Song and Carmichael, 2001; Feng and Penner, 2007; Zaveri et al., 2008; Trump et al., 2015), to the assumption that the bulk gas-aerosol phases instantly reach thermodynamic equilibrium (TEQ) and calculating their correspondent concentrations (Lurmann et al., 1997). While DMT can accurately capture processes far from TEQ (e.g. the condensation of gas species at low temperatures, under extreme ~~relative humidity (RH)~~ RH conditions or onto coarse particles), the inherent stiffness of inorganic heterogeneous chemistry renders DMT a rigorous but computationally-expensive methodology (Feng and Penner, 2007; Zaveri et al., 2008; Trump et al., 2015; Benduhn et al., 2016). On the other hand, assuming instantaneous TEQ is more efficient and has gained popularity despite its tendency to overestimate coarse nitrate formation (Nenes et al., 1998; Feng and Penner, 2007; Bauer et al., 2007; Hauglustaine et al., 2014; Paulot et al., 2016; Bian et al., 2017). To balance accuracy and computational cost, several intermediate strategies have been developed, including 1) simplifying the DMT equations to a first-order irreversible uptake reaction (UPTK), which ignores the evaporation of ~~uptaken~~ taken up species back to the gas phase (Jacob, 2000; Bauer et al., 2004; Feng and Penner, 2007; Fairlie et al., 2010), 2) ~~calculating TEQ concentrations~~ the double call of the TEQ concentrations calculation for both fine (diameter up to 2.5μm) and coarse (diameter above 2.5μm) modes of dust and SS

(double call method, DBCLL), either after kinetically limiting the gas condensing on each bin or mode (Pringle et al., 2010) or redistributing the condensed mass from the bulk TEQ using kinetic coefficients (Karydis et al., 2016), and 3) employing ~~a~~ an hybrid approach (HYB) that applies TEQ to the fine bins or modes and UPTK to the coarse ones (Capaldo et al., 2000; Hodzic et al., 2006; Hauglustaine et al., 2014; Trump et al., 2015). Overall, methods involving DMT or TEQ calculations allow to simulate the reversible heterogeneous reactions (condensation-evaporation dynamics), and the UPTK calculates the irreversible uptake of gas species, accounting for gas specifications, particle's alkalinity and environmental RH (Fairlie et al., 2010; Paulot et al., 2016).

~~Despite~~ Despite these efforts to incorporate nitrate heterogeneous reactions on coarse particles, atmospheric models still significantly diverge in their predictions of the tropospheric burden of oxidized ($HNO_{3(g)}$+NO_3^-) and reduced nitrogen ($NH_{3(g)}$+NH_4^+), often struggling to reproduce observational data of these species (Fairlie et al., 2010; Hauglustaine et al., 2014; Paulot et al., 2016; Zakoura and Pandis, 2018; Luo et al., 2019; Jones et al., 2021; Rémy et al., 2022). For instance, the particulate nitrate AeroCom phase III experiment (Bian et al., 2017), an extensive intercomparison study of atmospheric models incorporating NO_3^- formation processes on dust and SS, highlights substantial disagreements. The average NO_3^- atmospheric burden among models is 0.63 Tg, with a standard deviation of 0.56 Tg, nearly 90% of the mean value. Similar variability is observed for NH_4^+ (0.32 ± 0.20 Tg). The study also highlights the general inaccuracy of current models in reproducing observations of NO_3^- concentrations after long-range transport of precursor species, indicating that nitrogen heterogeneous chemistry processes on dust and SS are often misrepresented in models.

~~In this work , we systematically investigate the~~ The scope of the present work is to understand the role of dust in NO_3^- formation through a systematic investigation of the underlying processes governing ~~heterogeneous chemistry that lead to formation. We study the pathways driving nitrate formation on dust.~~ dust heterogeneous chemistry. To achieve this goal, we incorporate a variety of mechanisms of different complexities into a global model. This enables a comprehensive analysis of the partitioning between gas and aerosol phases, the suitability of irreversible and reversible parameterizations for the ~~gas species condensation on coarse~~ condensation of gas species on dust, and the role of explicit representation of alkalinity. While our primary emphasis is on the heterogeneous chemistry on dust surfaces, we also account for nitrate formation on SS and its alkalinity.

This paper is structured as follows. Section 2 introduces the MONARCH atmospheric chemistry model (2.1), detailing the specific developments implemented for this study (2.2), the setup of the simulations conducted (2.5) and the datasets used for evaluation (2.6). Section 3 presents an analysis of the global simulations and their evaluation against observational data. This section includes a comparison of the spatial distributions and an examination of the total nitrogen burden and ~~its~~ gas/particle partitioning. Additionally, we discuss the budgets of reduced and oxidized nitrogen species, depositions, production/loss rates and lifetimes. Our results are contextualized with findings from previous studies, providing a comprehensive understanding of the results. Section 4 provides a summary of our key findings.

2 Methods

2.1 The MONARCH model

MONARCH is an atmospheric chemistry model developed at the Earth Sciences department of the Barcelona Supercomputing Center (Pérez et al., 2011; Jorba et al., 2012; Badia et al., 2017; Klose et al., 2021; Gonçalves Ageitos et al., 2023; Navarro-Barboza et al., 2024). It simulates the atmospheric life cycle of aerosol and gas-phase species ~~in the atmosphere, utilizing~~ through an online coupling with the Nonhydrostatic Multiscale Model on the B-grid (NMMB) (Janjic and Gall, 2012). NMMB allows running both global and regional ~~domains~~ atmospheric simulations with embedded telescoping nests. The Arakawa B grid is used in the horizontal direction and the Lorenz hybrid pressure-sigma coordinate in the vertical direction. MONARCH ~~works on a~~ global simulations use a regular latitude-longitude ~~discretization~~ grid with polar filtering and a rotated longitude-latitude grid is adopted for regional applications. The NMMB numerical schemes are based on principles described in Janjic and Gall (2012). The physical parameterizations used in the model include (1) a surface layer scheme based on the Monin-Obuknov similarity theory (Monin and Obukhov, 1954) combined with a viscous sublayer on continental and water surfaces (Zilitinkevich, 1965; Janjic, 1984, 1996), (2) the Mellor–Yamada–Janjic (MYJ) planetary boundary layer and the free troposphere turbulence scheme (Janjić, 2001), (3) the Unified NCEP-NCAR-AFWA Noah land surface model (Ek et al., 2003) to compute the surface heat and moisture fluxes, (4) the 1D Rapid Radiative Transfer Model for Global circulation Models (RRTMG) (Iacono et al., 2008) for the calculation shortwave and longwave radiative fluxes, (5) the Ferrier microphysics scheme (Ferrier et al., 2002) for grid-scale clouds, and (6) the Betts–Miller–Janjic convective clouds scheme (Betts and Miller, 1986; Emanuel and Živković Rothman, 1999; Janjić, 2000). The same advection and vertical mixing schemes formulated in NMMB are used for both meteorological and chemistry species for consistency.

MONARCH includes a gas-phase module combined with a hybrid sectional–bulk multi-component mass-based aerosol module. The gas-phase chemistry is based on the Carbon Bond 2005 (CB05) chemical mechanism extended with chlorine chemistry (Yarwood et al., 2005; Whitten et al., 2010) designed to describe urban to remote tropospheric conditions. The photolysis rates are computed using the Fast-J scheme (Wild et al., 2000) accounting for aerosols, clouds, and absorbers such as ozone. A resistance approach is adopted for dry deposition (Wesely, 1989), and in-cloud and below-cloud scavenging and wet deposition ~~follows~~ follow Byun (1999) and Foley et al. (2010).

The aerosol representation in MONARCH considers 8 main components, namely dust, SS, black carbon, organic matter (both primary and secondary), SO_4^{2-}, NH_4^+, NO_3^- and unspeciated aerosol mass. Mineral dust and SS are described with a sectional size distribution of 8 bins spanning from $0.2\mu m$ to $20\mu m$ and $30\mu m$ in diameter, respectively. All the other aerosol components are represented by a fine mode, except NO_3^- ~~which is extended with a coarse mode~~ , represented with both fine and coarse modes to consider the condensation of $HNO_{3(g)}$ on coarse particles. Table S2 in the Supplementary material reports the bin volumetric and effective radii, density and ~~the bin or mode~~ their fractional contribution to $PM_{2.5}$ and PM_{10} ~~for , , .~~

Black carbon is ~~considered~~ represented in two primary ~~hydrophobic/hydrophilic modesand emitted as~~ modes: hydrophobic and hydrophilic, with 80% ~~hydrophobic. An ageing process during its transport~~of its emitted mass initially classified as hydrophobic. During atmospheric transport, an aging process with an e-folding time of 1.2 days ~~transfers mass from hydrophobic~~

~~to hydrophilic modes~~ facilitates the transition of mass from the hydrophobic to the hydrophilic mode (Chin et al., 2002). Organic aerosols ~~follow the simple scheme of Pai et al. (2019) assuming~~ are represented using the simplified scheme of Pai et al. (2020), which assumes fixed secondary organic aerosol (SOA) yields ~~adjusted to match more complex approaches (i. e. volatility based schemes). Similar~~ calibrated to align with more complex volatility-based approaches. For primary organic aerosols, a dual-mode representation—hydrophobic and hydrophilic—is adopted, similar to black carbon~~, primary organic emissions are emitted as~~ . In this scheme, 50% ~~hydrophobic with an ageing~~ of the emitted mass is classified as hydrophobic, with an aging e-folding time of 1.15 days ~~. Designed~~ transitioning it to the hydrophilic mode. Originally designed for global models, this approach has also ~~shown good results at regional scale~~ demonstrated strong performance at regional scales (Navarro-Barboza et al., 2024).

A simplified gas–aqueous–aerosol mechanism accounts for sulfur chemistry through the oxidation of $SO_{2(g)}$ and dimethyl sulfide (DMS) ~~and assuming complete nucleation for the remaining~~ to $H_2SO_{4(g)}$ ~~as after the~~ . At the end of each chemistry integration time step, the remaining $H_2SO_{4(g)}$ that has not formed aqueous sulfate is assumed to fully nucleate into fine particulate SO_4^{2-} (Spada, 2015). The heterogeneous hydrolysis of $N_2O_{5(g)}$ on aqueous sulfate particles ~~accounts~~ is included to account for additional $HNO_{3(g)}$ formation, following the formulation of Riemer et al. (2003). Prior to this study, secondary nitrate–ammonium ~~aerosol was solved using TEQ model~~ aerosols were modeled using the TEQ module EQuilibrium Simplified Aerosol Model version v03b (EQSAM v03b, Metzger et al. (2002)) for fine particles. ~~Note~~ It is important to note that EQSAM v03b ~~only considers the partitioning of~~ exclusively considers sulfate-nitrate-ammonium ~~without considering~~ partitioning and does not account for the presence of other species (i.e. Dust or SS alkalinity). ~~(Below we describe~~ In Section 2.2.2 we detail the adoption of ISORROPIA-II v1 ~~(Milousis et al., 2024) for the purpose of~~ (Fountoukis and Nenes, 2007) for this study. ~~)~~ To account for secondary nitrate aerosol formation on coarse dust and SS particles, an hybrid (HYB) approach ~~is~~ was employed through an uptake reaction (UPTK) of $HNO_{3(g)}$. The reaction uses the uptake rate (K) defined by Jacob (2000) as a first-order function (Schwartz, 1986):

$$K = \left(\frac{r}{D_g} + \frac{4}{v\gamma} \right)^{-1} \cdot S \tag{1}$$

where r is the aerosol bin radius, D_g ~~is~~ the gas-phase diffusion coefficient, v the mean molecular speed, S the aerosol specific surface area, and γ the uptake coefficient, defined as the ratio of the number of gas molecules reacting with the particle's surface over the fraction of molecules being absorbed by the given surface (i.e. the accommodation coefficient) (Phadnis and Carmichael, 2000; Guimbaud et al., 2002). A γ value of 0.1 ~~is~~ was assumed for dust (Hanisch and Crowley, 2001; Vlasenko et al., 2006) and 0.01 for SS (Tolocka et al., 2004). The production of fine and coarse NO_3^- ~~is~~ was traced in separated bins.

Finally, MONARCH includes meteorology-driven emission modules for key species. Emissions of biogenic non-methane volatile organic compounds (NMVOC) and NO are calculated from the Model of Emissions of Gases and Aerosols from Nature (MEGAN) v2.04 (Guenther et al., 2006). Several SS source functions are available in the model (Spada et al., 2013); here we use the Jaeglé et al. (2011) formulation. Similarly, different parameterizations for dust emissions are available ranging from more simplified to more physics-based descriptions (Klose et al., 2021). Following Gonçalves Ageitos et al. (2023), the

G01-UST scheme based on Ginoux et al. (2001) described in Klose et al. (2021) is used in this work. ~~For dust emission, the topography-based source function from Ginoux et al. (2001) is used to scale the dust flux from available sources and to set its dependency on surface friction velocity.~~ Dust emission is limited to areas presenting a frequency of occurrence of dust optical depth above 0.2, identified using maps created from Moderate Resolution Imaging Spectroradiometer (MODIS) Deep Blue retrievals (Hsu et al., 2004; Ginoux et al., 2012). Surface roughness influence on dust emission is parameterized based on ~~Raupach et al. (1993)~~Raupach et al. (1993), whose vegetation cover is determined using surface reflectance from Landsat and MODIS monthly data (Raupach et al., 1993; Guerschman et al., 2015).

For the evaluation of the model's dust cycle, the reader is referred to Klose et al. (2021) and Gonçalves Ageitos et al. (2023), and for SS to Spada et al. (2013).

2.2 Model updates

In this study, we investigate the primary chemical pathways responsible for NO_3^- formation on ~~coarse particles~~ preexisting particles, with a particular focus on coarse dust particles, by integrating mechanisms of varying complexity within the global model MONARCH (~~Figure~~ Fig. 1). Table 1 lists the irreversible and reversible heterogeneous reactions considered in our analysis. Here, we detail the enhancements implemented in MONARCH to address partially or fully the array of reactions of interest, with a primary focus on maintaining a balance between complexity, accuracy, and computational efficiency in the resulting solution.

To trace the formation of fine and coarse NO_3^-, NH_4^+, and SO_4^{2-} ~~,~~ under moist conditions — the primary regime where these formation pathways occur (Usher et al., 2003; Jordan et al., 2003) — an additional hydrophilic bin for the coarse mode of these ~~three~~ species is added to the default MONARCH size ~~parameterization, as reported in the~~ parametrization, as detailed in Supplementary Table S2. The new bins account for the total mass of NO_3^-, NH_4^+, and SO_4^{2-} formed on both dust and SS particles indiscriminately. Sensitivity tests, with and without dust and SS in the UPTK and TEQ processes, assess their relative contributions (see Section 2.4).

2.2.1 Irreversible heterogeneous chemistry of nitrate and sulfate

A widely adopted method to simulate NO_3^- and SO_4^{2-} formation on coarse particles involves incorporating irreversible heterogeneous reactions of gas species on dust and SS through a first-order uptake parameterization. Specifically, the uptake of $HNO_{3(g)}$ on coarse particles is commonly assumed to drive coarse NO_3^- formation (Jacob, 2000; Hodzic et al., 2006; Bauer et al., 2004; Feng and Penner, 2007; Fairlie et al., 2010; Hauglustaine et al., 2014; Paulot et al., 2016; Jones et al., 2021), while the uptake of $SO_{2(g)}$ is known to lead to the formation of coarse SO_4^{2-} (Phadnis and Carmichael, 2000; Song and Carmichael, 2001; Usher et al., 2002; Prince et al., 2007; Fairlie et al., 2010; Li et al., 2012; Liu and Abbatt, 2021; Yue et al., 2022). Most models assume constant uptake coefficients (γ) for these reactions, for example $\gamma = 0.1$ for $HNO_{3(g)}$ uptake on dust (Dentener et al., 1996; Hanisch and Crowley, 2001, 2003; Bauer et al., 2004; Hodzic et al., 2006; Wei, 2010)). However, recent studies have shown that using this value tends to overestimate NO_3^- formation (Vlasenko et al., 2006; Mashburn et al., 2006; Fairlie et al., 2010). This suggests that the uptake coefficient for $HNO_{3(g)}$ should be lower and that it is highly influenced by RH

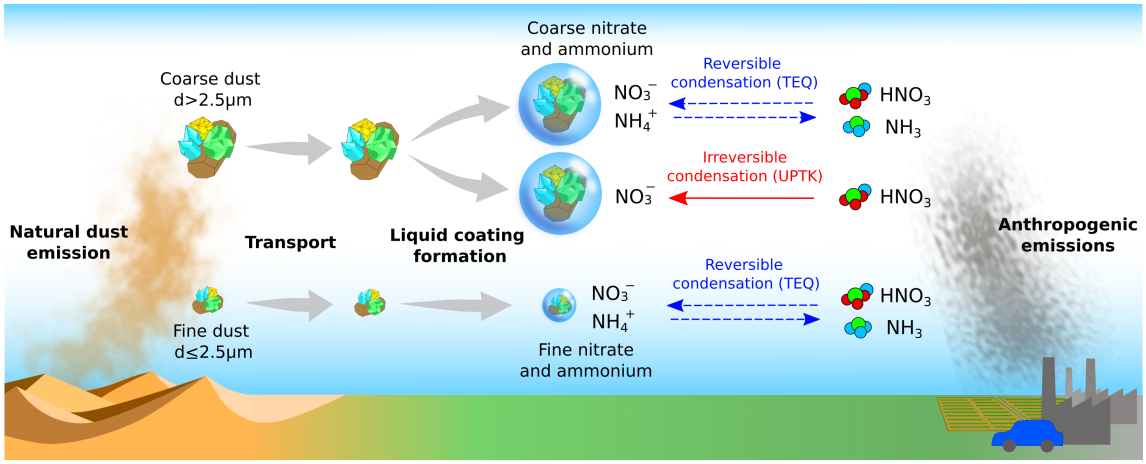

Figure 1. ~~Graphical illustration~~ Illustration of the respective mineral dust heterogeneous chemistry mechanisms implemented in this work for fine and coarse particles. Fine dust aqueous coating is assumed to reach thermodynamic equilibrium (TEQ) with anthropogenic gas species to form fine particulate nitrate (NO_3^-). Conversely, coarse particulate nitrate is formed either through also the reversible condensation (TEQ) of $HNO_{3(g)}$ and $NH_{3(g)}$ after kinetic limitation, or through the irreversible uptake reaction (UPTK) of $HNO_{3(g)}$ on coarse dust particles. Particulate ammonium (NH_4^+) is formed in both modes ~~if~~ in those mechanisms assuming TEQ~~is assumed~~.

(Goodman, 2000; Krueger et al., 2003; Vlasenko et al., 2006, 2009; Fairlie et al., 2010; Wei, 2010) and dust alkalinity (Goodman, 2000; Hanisch and Crowley, 2001; Krueger et al., 2004; Liu et al., 2007; Prince et al., 2007; Wei, 2010; Crowley et al., 2010). Recent studies increasingly implement γ as a function of RH and employ different parameterizations of this function to account for dust alkalinity.

For our study, we extended the chemical mechanism of MONARCH to incorporate pathways for the formation of coarse NO_3^- and sulfate aerosols (~~Figure~~ Fig. 2). This extension involved refining irreversible heterogeneous parameterizations within the model, specifically the uptake of $HNO_{3(g)}$ on dust and SS particles (R4-5 in Table 1), as well as the uptake of $SO_{2(g)}$ on dust particles (R3 in Table 1). No additional heterogeneous chemistry, such as the transformation of $NO_{2(g)}$ to $HNO_{3(g)}$ on the surface of dust particles, was considered due to its relatively low significance (Jacob, 2000; Jordan et al., 2003; Liao et al., 2003; Li et al., 2

Our implementation incorporates dependencies of γ on RH and the alkalinity of dust (Vlasenko et al., 2006, 2009; Liu et al., 2007, 2008; Crowley et al., 2010; Fairlie et al., 2010; Wei, 2010).

The γ dependency on RH is modeled akin to a Brunauer–Emmett–Teller (BET) isotherm, which characterizes water adsorption on dust particles (Vlasenko et al., 2006). We employed a modified BET function to formulate γ, extending it to account for dust alkalinity. This formulation is represented by the following equation:

$$\gamma = Sc \cdot \frac{|c_1 \cdot RH|}{(1 - RH)|1 + c_2 \cdot RH|} \tag{2}$$

Table 1. Heterogeneous reactions implemented in MONARCH. Dust and sea-salt particles are referred as *DU* and *SS*, respectively.

Irreversible reactions			
	Reaction	Process	Notes
(R1)	$\mathrm{DU_{(aer)}} + \mathrm{H_2SO_{4(g)}} \rightarrow \mathrm{SO^{2-}_{4(aq)}}$	condensation	1
(R2)	$\mathrm{SS_{(aer)}} + \mathrm{H_2SO_{4(g)}} \rightarrow \mathrm{SO^{2-}_{4(aq)}}$	condensation	1
(R3)	$\mathrm{DU_{(aer)}} + \mathrm{SO_{2(g)}} \rightarrow \mathrm{SO_{4(aer)}}$	UPTK (γ_1)	2
(R4)	$\mathrm{CaCO_{3(aer)}} + 2\mathrm{HNO_{3(g)}} \rightarrow \mathrm{Ca(NO_3)_{2(aer)}} + \mathrm{H_2O} + \mathrm{CO_2}$	UPTK (γ_2)	3, 4
(R5)	$\mathrm{SS_{(aer)}} + \mathrm{HNO_{3(g)}} \rightarrow \mathrm{NaNO_{3(aer)}} + \mathrm{HCl_{(g)}}$	UPTK (γ_3)	4, 5

Gas-particle equilibrium reactions			
	Reaction	Process	Notes
(R6)	$\mathrm{HNO_{3(g)}} + \mathrm{NH_{3(g)}} \rightleftharpoons \mathrm{NH^{+}_{4(aq)}} + \mathrm{NO^{-}_{3(aq)}}$	TEQ	6
(R7)	$\mathrm{H_2SO_{4(g)}} + \mathrm{NH_{3(g)}} \rightleftharpoons \mathrm{NH^{+}_{4(aq)}} + \mathrm{SO^{2-}_{4(aq)}}$	TEQ	6, 7
(R8)	$\mathrm{CaCO_{3(aq)}} + 2\mathrm{HNO_{3(g)}} \rightleftharpoons \mathrm{Ca^{2+}_{(aq)}} + 2\mathrm{NO^{-}_{3(aq)}} + \mathrm{H_2O} + \mathrm{CO_2}$	TEQ	4, 8
(R9)	$\mathrm{MgCO_{3(aq)}} + 2\mathrm{HNO_{3(g)}} \rightleftharpoons \mathrm{Mg^{2+}_{(aq)}} + 2\mathrm{NO^{-}_{3(aq)}} + \mathrm{H_2O} + \mathrm{CO_2}$	TEQ	4, 8
(R10)	$\mathrm{K_2CO_{3(aq)}} + 2\mathrm{HNO_{3(g)}} \rightleftharpoons 2\mathrm{K^{+}_{(aq)}} + 2\mathrm{NO^{-}_{3(aq)}} + \mathrm{H_2O} + \mathrm{CO_2}$	TEQ	4, 8
(R11)	$\mathrm{Na_2CO_{3(aq)}} + 2\mathrm{HNO_{3(g)}} \rightleftharpoons 2\mathrm{Na^{+}_{(aq)}} + 2\mathrm{NO^{-}_{3(aq)}} + \mathrm{H_2O} + \mathrm{CO_2}$	TEQ	4, 8
(R12)	$\mathrm{NaCl_{(aq)}} + \mathrm{HNO_{3(g)}} \rightleftharpoons \mathrm{Na^{+}_{(aq)}} + \mathrm{NO^{-}_{3(aq)}} + \mathrm{HCl_{(g)}}$	TEQ	4, 9

1. Sulfuric acid ($\mathrm{H_2SO_{4(g)}}$) is assumed to completely condense on fine and coarse dust and SS, transferring mass to the respective size mode. The condensation reaction does not depend on dust and SS alkalinity, but solely on their specific surface area based on Pringle et al. (2010).

2. Sulfur dioxide ($\mathrm{SO_{2(g)}}$) uptake coefficient on dust (γ_1) is a function of RH as defined in Fairlie et al. (2010) and based on experimental studies performed on calcite particles by Prince et al. (2007). However, to account for $\mathrm{SO_{2(g)}}$ oxidation by deliquesced $\mathrm{O_3}$ and $\mathrm{NO_2}$, the UPTK reaction of $\mathrm{SO_{2(g)}}$ is performed even in the absence of alkalinity. That is why this reaction is considered to happen over $\mathrm{DU_{(aer)}}$ and not only over $\mathrm{CaCO_{3(aq)}}$, although it assumes same dust alkalinity as in nitric acid uptake (R4).

3. Nitric acid ($\mathrm{HNO_{3(g)}}$) uptake coefficient on $\mathrm{CaCO_{3(aq)}}$ (γ_2) is a function of RH as defined by Fairlie et al. (2010) based on experimental studies performed on calcite particles by Liu et al. (2008). $\mathrm{CaCO_{3(aq)}}$ concentration is used instead of $\mathrm{DU_{(aer)}}$ concentration because the uptake coefficient is scaled for alkalinity as shown in Eq. 2.

4. $\mathrm{CaCO_{3(aq)}}$, $\mathrm{MgCO_{3(aq)}}$, $\mathrm{K_2CO_{3(aq)}}$, $\mathrm{Na_2CO_{3(aq)}}$ and $\mathrm{NaCl_{(aq)}}$ refers to the NVC content derived from the $\mathrm{DU_{(aer)}}$ and $\mathrm{SS_{(aer)}}$ concentrations using fractions from Gonçalves Ageitos et al. (2023) for dust and from Seinfeld and Pandis (2006) for SS (Section 2.2.3).

5. $\mathrm{HNO_{3(g)}}$ uptake coefficient on SS (γ_3) is based on the experimental study Liu et al. (2007), that reports $\mathrm{HNO_{3(g)}}$ uptake kinetics for different RH and sea-salt particles sizes. The average value $\gamma_3 = 0.05$ for particles from 2.5 to 10 μm (coarse mode) is assumed, considering ambient RH=80%.

6. Neutralization of $\mathrm{HNO_{3(g)}}$ and $\mathrm{H_2SO_{4(g)}}$ by ammonia is calculated through TEQ with ISORROPIA-II. It is assumed to happen in the fine mode for all mechanisms, and additionally in the coarse mode over coarse particles in those mechanisms considering coarse $\mathrm{NO_3^-}$ and $\mathrm{NH_4^+}$ formation (Myhre et al., 2006; Usher et al., 2003; Uno et al., 2020). All reactants and products are assumed to remain in the aqueous phase (metastable assumption).

7. The result of the neutralization of $\mathrm{H_2SO_{4(g)}}$ can be $\mathrm{(NH_4)_2SO_{4(aer)}}$, $\mathrm{NH_4HSO_{4(aer)}}$ or $\mathrm{(NH_4)_3H(SO_4)_{2(aer)}}$ if solid results were assumed (Liu et al., 2022), but under metastable assumption only aqueous ions of $\mathrm{SO_4^{2-}}$ are considered.

8. Calcium, magnesium, potassium and sodium (NVC) deliquesced from carbonates present in the bulk of dust particles neutralize $\mathrm{HNO_{3(g)}}$ in the liquid coating of dust aerosols (Usher et al., 2003; Krueger et al., 2004; Fountoukis and Nenes, 2007; Hauglustaine et al., 2014). Dust NVC content (i.e. alkalinity) is dependent on particle size and globally averaged from Journet et al. (2014) mineral data.

9. Sodium chloride from sea-salt particles dissolves and reacts with $\mathrm{HNO_{3(g)}}$ in the liquid coating of sea-salt particles (Myhre et al., 2006). Sea-salt also presents other NVC that are included in reactions R8-11, which are assumed globally homogeneous from Seinfeld and Pandis (2006) and Karydis et al. (2016).

where RH is the relative humidity (ranging from 0 to 1), c_1 and c_2 denote the water adsorption scaling factors (Vlasenko et al., 2006), and *Sc* is a factor dependent on dust alkalinity. For the uptake of $HNO_{3(g)}$ on dust (~~R4-5~~ R4 in Table 1), typical values assumed for c_1 and c_2 are ~~8 and 7~~8.0 and 7.0, respectively (Li et al., 2012; Paulot et al., 2016; Wang et al., 2017). ~~However,~~ For *Sc*, however, literature reports varying values ~~for *Sc*~~ based on dust alkalinity assumptions, ranging from $Sc=\frac{1}{30}$ for the industrially-standardized Arizona Test Dust (Möhler et al., 2006; Herich et al., 2009; Suman et al., 2024) to $Sc=0.018$ for samples from the China Loess ~~(~~with 39% $CaCO_3$ content ~~)~~ (Krueger et al., 2004; Wei, 2010).

We adopt the uptake RH functions for both $HNO_{3(g)}$ and $SO_{2(g)}$ on dust from Fairlie et al. (2010). To fit experimental data from Song et al. (2007) and the RH function reported by Fairlie et al. (2010), for $\gamma(HNO_3)$ (Reaction R4 in Table 1) we determine $c_1=3.84 \cdot 10^{-4}$ and $c_2=0.56$~~for $\gamma(HNO_3)$~~. Additionally, Fairlie et al. (2010) assumes a NVC content of 3.0% of Ca and 0.6% of Mg, which differs from the NVC values used in the present study. Therefore, we use the alkalinity scaling factor *Sc* to normalize the Fairlie et al. (2010) function accordingly~~, as described in Section 2.2.3~~. Specifically, values for *Sc* are defined as the ratio of Ca and Mg percentage used in our study relative to those assumed by Fairlie et al. (2010), resulting in $Sc = 1.80$ and $Sc = 1.52$ respectively for the two ~~alkalinity values~~ average alkalinity values derived from Journet et al. (2014) and Claquin et al. (1999) used in our experiments (see Section 2.2.3 below). Note that *Sc* is zero if no alkalinity is considered and that a constant value of $\gamma(HNO_3) = Sc \cdot 1.05 \cdot 10^{-3}$ is used for RH higher than 80%.

Similarly, we ~~determine incorporating~~ determined the $\gamma(SO_2)$ on dust (R3 in Table 1) fitting ~~equation~~ Eq. 2 to experimental data from Prince et al. (2007) and the RH function from Fairlie et al. (2010), yielding values of $c_1 = 2.7 \cdot 10^{-6}$ and $c_2 = -1.06$. The same *Sc* values as used for $\gamma(HNO_3)$ ~~is applied here.~~ are applied for $\gamma(SO_2)$: $Sc = 1.80$ and $Sc = 1.52$. However, if alkalinity is not considered, *Sc* is set to 1.0 (and not zero, as the case for $\gamma(HNO_3)$) to account for the oxidation of $SO_{2(g)}$ by deliquesced O_3 and NO_2 ~~(Usher et al., 2002; Prince et al., 2007)~~(Usher et al., 2002; Prince et al., 2007; Yu et al., 2017; Li et al., 2024). For RH above 90%, $\gamma(SO_2)$ remains constant at $\gamma(SO_2) = Sc \cdot 5.0 \cdot 10^{-4}$.

For the $HNO_{3(g)}$ uptake on SS (R5 in Table 1), we adopted the $\gamma(HNO_3)$ values of Liu et al. (2007), which provide experimental estimates of this factor for different particle sizes and RH. However, a clear uptake function on these parameters has not been found in the literature. Therefore, for the sake of simplicity, we defer an implementation of an uptake coefficient dependent on these metrics to future research. In this study, we did not account for the RH dependency of $\gamma(HNO_3)$, and instead we used average values at 80% RH resulting in $\gamma(HNO_3) = 0.15$ for SS particles in the range of 0.1 to 2.5 μm and $\gamma(HNO_3) = 0.05$ for particles larger than 2.5 μm. While larger values have been reported by Guimbaud et al. (2002), we opted for these values as they align with more widely accepted ranges found in the literature (Saul et al., 2006; Pratte and Rossi, 2006; Liu et al., 2007; Fagerli et al., 2015). Using higher values could potentially overestimate the uptake on SS particles.

The condensation of $H_2SO_{4(g)}$ (R1-2 in Table 1) on dust and SS is another relevant source of SO_4^{2-} introduced in our model. Due to the extremely low volatility of $H_2SO_{4(g)}$ at atmospheric temperatures, its condensation onto existing particles is assumed as irreversible and ~~nearly~~ complete. This process signifies a direct mass transfer from the gas to the aerosol phase (Zaveri et al., 2008; Hauglustaine et al., 2014). The amount of $H_2SO_{4(g)}$ that condenses in the fine and coarse modes is determined using kinetic diffusive coefficients calculated as described in ~~section~~ Section 2.3.

2.2.2 Reversible heterogeneous chemistry of nitrate and ammonium

The gas-aerosol partitioning of semivolatile inorganic aerosols in previous studies with MONARCH was based on the EQSAM v03b TEQ model. EQSAM provides a computationally efficient approach that bypasses the expensive iterative activity coefficient calculation employed in other thermodynamic models. EQSAM was originally designed to handle the partitioning of ammonium-sulfate-nitrate-water system excluding solid components and was extended to include solids, HCl and Cl-/Na+ in the version v03b, the one used in MONARCH. One of the limitations of such version is the lack of information on NVC and/or mineral species in traced species.

For this study, we implemented the ISORROPIA-II v1 (Fountoukis and Nenes, 2007) TEQ model as an additional option in MONARCH to investigate the sensitivity of the partitioning of semivolatile inorganic compounds to NVCs. While a more recent version of ISORROPIA-II (v2.3) exists, which improves aerosol pH estimations at near pH-neutral conditions (Song et al., 2018), global scale simulations have shown only minor differences when compared to ISORROPIA-II v1 (Milousis et al., 2024).

ISORROPIA-II v1 determines TEQ concentrations of gas, liquid and solid phases. It can assume either stable conditions, where compounds precipitate into solids, or metastable conditions, where compounds remain as supersaturated liquid solutions. To enhance computational efficiency, ISORROPIA-II employs a segmented approach for calculating TEQ concentrations. This approach defines five different regimes based on the ratios of precursor species (i.e. sulfate, sodium and crustal species), RH and temperature. Each regime addresses a specific subset of relevant species and equilibrium equations. Efficiency is further improved by retrieving species' activity coefficients from look-up tables (Fountoukis and Nenes, 2007; Milousis et al., 2024). The medium acidity is determined by the concentrations of acidic/basic gaseous species ($HNO_{3(g)}$, $NH_{3(g)}$, $H_2SO_{4(g)}$), particle (NH_4^+, SO_4^{2-}, NO_3^-), and crustal ions (K^+, Ca^{2+}, Mg^{2+}, Na^{2+}, Cl^-), which are inputs to ISORROPIA-II. After TEQ is calculated with these species, the resulting pH is provided by the thermodynamic model.

In this work, we use the metastable solution of ISORROPIA-II, assuming all the resulting particulate compounds from the TEQ computation to remain in the liquid phase. Previous studies comparing stable and metastable methodologies with ISORROPIA-II have reported only marginal differences in global nitrate budgets between both modes. ~~These~~ At global scales, these differences noted slightly ~~lower pH values~~ higher pH values (0.5) and nitrate formation (2%) when using the metastable assumption (Karydis et al., 2016, 2021; Milousis et al., 2024)~~. Furthermore, the metastable assumption~~ , although these differences are reported to be more important (<2 pH units and <60% nitrate concentrations) close to regions with low RH and high concentration of crustal species, or their downwind areas. However, given the global scale scope of the present study, we used the metastable assumption since it allows for full traceability of total aerosol nitrate, ammonium and sulfate formation (reactions ~~R5-8~~ R6-12 in Table 1).

We also adopt the temperature and pressure applicability range for ISORROPIA-II proposed by Sulprizio (2022), which highlights potential instabilities in reactions occurring below 250ºK and 200hPa. Consequently, ISORROPIA-II computations are limited to cells with temperature and pressure values above these thresholds.

2.2.3 Dust and sea-salt alkalinity

Alkalinity refers to the ability of a substance to neutralize acids and maintain a stable pH level. Both dust and SS particles contain NVCs that contribute to the overall alkalinity of the aerosol, thereby neutralizing gas acidic species such as $HNO_{3(g)}$ and sulfates.

To investigate the importance of representing dust ~~and SS~~ alkalinity, we derive a global average size-dependent NVCs content from 5-year long MONARCH simulations that explicitly track dust mineral species (Gonçalves Ageitos et al., 2023). To assess the uncertainty arising from our limited knowledge of the soil mineralogy of dust sources, we relied on two different MONARCH experiments detailed in Gonçalves Ageitos et al. (2023), which utilized the Claquin et al. (1999) and Journet et al. (2014) soil mineralogical datasets, respectively. The simulation based on Claquin et al. (1999) accounts for eight distinct minerals, whereas the simulations based on Journet et al. (2014) for twelve minerals (Table S3). The Claquin et al. (1999) dataset includes quartz, feldspar, illite, smectite, kaolinite, calcite, gypsum, and hematite. The Journet et al. (2014) dataset includes these minerals as well as chlorite, vermiculite, mica, and goethite (Table S5). In this study, we adopt an upper bound for the minerals' solubility and reactivity with gas species based on Hanisch and Crowley (2001). Moreover, we assume size-dependent but globally homogeneous values for dust mineralogy, and ~~therefore~~ consequently dust alkalinity and NVC, to focus on understanding heterogeneous reaction parameterizations. We defer the analysis of the potential importance of geographical dust mineralogical variations upon dust heterogeneous chemistry to a forthcoming study.

Based on the global average mineral mass fraction for each dust size bin derived from the mineralogy simulations and the elemental composition associated to each mineral (see the Supplementary Tables S4 and S6) we estimate the average NVC content per dust size bin at each time step following ~~equation~~ Eq. 3:

$$NVC_{i,j} = \left(\sum_k fNVC_{k,j} \cdot M_{i,k} \right) \cdot DU_i \tag{3}$$

where the NVC concentration for each element *j* (i.e., Ca, Mg, K, Na) and size bin *i* ($NVC_{i,j}$) at a given location is derived by considering the ~~NVC molar fraction~~ molar fraction of each element in each mineral *k* ($fNVC_{k,j}$), the global average mass fraction of each mineral and size bin ($M_{i,k}$) and the bin's dust concentration at the specified location (DU_i). $NVC_{i,j}$ serves as input to the TEQ calculation. We consider only minerals soluble in water or acids that may at least partly dissolve in the liquid coating of the particles (Usher et al., 2003), and only NVC reacting with the gas species in ISORROPIA-II are used (calcite, magnesium, potassium, sulfate, chlorite or sodium) for the calculation.

The dust NVC global average content ~~result~~ results in: 5.17% Ca^{2+}, 0.79% Na^{+}, 2.37% K^{+}, 1.32% Mg^{2+} for the Journet et al. (2014) dataset, and 3.68% Ca^{2+}, 0.87% Na^{+}, 3.15% K^{+}, 1.75% Mg^{2+} for Claquin et al. (1999). The size-resolved NVC percentages for each dust bin are reported in the Supplementary Tables S3, S4, S5 and S6. ~~These values~~

In most of the sensitivity runs, the Journet et al. (2014) global average is employed, if not stated otherwise (see Table 3). Values for Claquin et al. (1999) are used solely in one sensitivity test, as explained in Section 2.4. These values are within the range ~~of~~ reported by Karydis et al. (2016) (5.36±3.69% Ca^{2+}, 2.46±1.90% Na^{+}, 2.08±1.34% K^{+}, 1.96±2.20% Mg^{2+}). The

	t0: Fine SO4	t1: Fine DU	t2: Coarse DU	t3: Gas HNO3, NH3 and H2SO4	t4: Fine DU & SS	t5: Coarse DU	t6: Coarse SS	t7: Fine/Coarse SO4
fTEQ	Cond. (x1.0 H2SO4)	UPTK (SO2)	UPTK (SO2)	-	TEQ (NH3 & HNO3)	-	-	-
HYB				-		UPTK (HNO3)	UPTK (HNO3)	-
DBCLL	Cond. (x0.5 H2SO4)			DIFFLIM		TEQ (NH3 & HNO3)		Cond. H2SO4

Table 2. Sequence of reactions and calculations performed for each scheme (rows). In columns, the sequence order (t*N*) and the gas/aerosol mode of each process is indicated. Dust and sea-salt particles are referred as *DU* and *SS*, respectively, and condensation is abbreviated as *Cond.*.

Journet et al. (2014) dataset results in a higher proportion of Ca^{2+} compared with Claquin et al. (1999), while similar fractions for Na^{+} and K^{+} are reported.

Additionally, as discussed in ~~section~~ Section 2.2.1, the derived dust NVC implies the application of the scaling factors $Sc = 1.80$ and $Sc = 1.52$ in ~~eq~~ Eq. 2 for the irreversible uptake experiments, assuming the average alkalinity derived from the Journet et al. (2014) and Claquin et al. (1999) simulations, respectively.

Regarding SS, we use a global average composition from Seinfeld and Pandis (2006) with 55% Cl^{-}, 30.6% Na^{+}, 7.7% SO_4^{2-}, 3.7% Mg^{2+}, 1.2% Ca^{2+}, and 1.1% K^{+}.

2.3 Nitrate mechanisms under study

In atmospheric conditions, $HNO_{3(g)}$ and $NH_{3(g)}$ ~~do not exhibit as low volatility as~~ exhibit higher volatility compared to $H_2SO_{4(g)}$. ~~Consequently~~As a result, their condensation onto liquid coatings around particles is a reversible process and should not be assumed as irreversible uptake reactions (Usher et al., 2003). Different mechanisms have been proposed to model the partitioning of nitrate and ammonium across the entire aerosol size range, aiming to mitigate the computationally expensive cost of solving the dynamic mass transfer equations (Capaldo et al., 2000; Feng and Penner, 2007; Hauglustaine et al., 2014).

The assumption of TEQ between gas and aerosol phases provides a practical approximation to account for the potential evaporation of already dissolved molecules in the liquid coating of fine particles. Equilibrium timescales for fine ammonium nitrate (diameter less than $1\mu m$) are typically on the order of minutes under typical atmospheric conditions ~~(Wexler and Seinfeld, 1990; Dassios and Pandis, 1999)~~(Wexler and Seinfeld, 1990; Dassios and Pandis, 1999). However, in TEQ models, it is assumed that TEQ is reached within each model time-step (on the order of few minutes). This assumption is reasonable for fine particles, but less so for coarse particles, where achieving equilibrium can take minutes to hours (Feng and Penner, 2007).

To overcome this limitation, different approaches have been proposed in the literature to incorporate the condensation-evaporation of $HNO_{3(g)}$ and $NH_{3(g)}$ on coarse particles while minimizing computational costs. In this study, we explore two such methods. (1) The hybrid method (HYB) (Hodzic et al., 2006; Feng and Penner, 2007) solves the partitioning over fine particles using a TEQ model and employs a first-order irreversible uptake (UPTK) reaction for condensation over coarse particles (section 2.2.1). ~~More refined approaches treat~~ (2) A more refined approach treats the formation of coarse NO_3^{-} as a reversible process through the combination of a double call ~~to~~ of the TEQ calculation, one for the fine and one for the coarse mode (DBCLL), together with a kinetic limitation of the gas species involved in the partitioning ~~(DBCLL)~~ (Pringle et al.,

2010). These two mechanisms are evaluated in this study to assess their impact on the formation of coarse NO_3^- and NH_4^+, as illustrated in ~~Figure~~ Fig. 2. Additionally, for the purpose of comparison, a scheme neglecting coarse NO_3^- formation (fTEQ) is also employed. We briefly describe each approach below.

~~To assess the effect of neglecting coarse and formation on atmospheric composition, the~~ The fTEQ approach solves the partitioning of semivolatile inorganic species with ISORROPIA-II exclusively within the fine mode to assess the effect of neglecting coarse NO_3^- and NH_4^+ formation on atmospheric composition. This mechanism solves the nitric-ammonia-sulfate neutralization (R6-7 in Table 1), accounting for alkalinity effects (R8-12 in Table 1) if fine dust and SS are considered in the mixture. Since $H_2SO_{4(g)}$ and SO_4^{2-} influence the ambient pH, they are always involved in any TEQ calculation. As described in Section 2.1, aqueous sulfate formation is solved through the oxidation of $SO_{2(g)}$ and DMS. Here, however, only 50% of the remaining $H_2SO_{4(g)}$ is assumed to directly nucleate as fine SO_4^{2-} through the aqueous phase chemistry, while the rest condenses into fine SO_4^{2-} through reactions R1 and R2 in Table 1 (~~Figure~~ Fig. 2 (a)). While in our study fTEQ serves as a sensitivity test to assess the impact of neglecting coarse NO_3^- and NH_4^+ formation, the fTEQ approach may be appropriate in environments where coarse particles are sparse or in applications focusing primarily on fine particle formation (Bian et al., 2017).

Conversely, the HYB mechanism (~~Figure~~ Fig. 2 (a)) is a commonly employed strategy in atmospheric chemistry models to represent nitrate formation on coarse particles. It solves NO_3^- formation through a sequential implementation of 1) TEQ reaction between $HNO_{3(g)}$ and $NH_{3(g)}$ considering internal mixing with fine dust and SS modes (R6-12 in Table 1), and 2) an irreversible first-order UPTK reaction of the remaining $HNO_{3(g)}$ on the coarse modes of dust and SS, excluding its evaporation back to the gas phase (R4 and R5 in Table 1). The UPTK reaction of $HNO_{3(g)}$ follows the implementation detailed in ~~section~~ Section 2.2.1. Sulfate is treated in an analogous manner to the fTEQ mechanism.

Finally, the DBCLL mechanism (~~Figure~~ Fig. 2 (b)) (Pringle et al., 2010) treats coarse NO_3^- and NH_4^+ formation as a reversible condensation-evaporation process. Firstly, the DBCLL methodology involves the calculation of kinetic diffusion limitation coefficients (DIFFLIM) for both the fine and coarse size modes of each of the condensing gas species, which restricts the amount of gas available to condense on each mode (Table 2). DIFFLIM has been implemented based on the formulation by Vignati et al. (2004) for $H_2SO_{4(g)}$, and its extension to other gases by Pringle et al. (2010). Following DIFFLIM, sequential TEQ calculations are conducted over fine and coarse modes (double call of the TEQ model, reactions R8-12 in Table 1), using the DIFFLIM coefficients to limit the availability of gas condensing on each mode.

Regarding the sulfate treatment in DBCLL, ~~as~~ a similar approach to fTEQ is employed, but the DIFFLIM coefficients calculated for $H_2SO_{4(g)}$ are used to condense the available $H_2SO_{4(g)}$ into either fine or coarse modes of SO_4^{2-} (reactions R1 and R2 in Table 1 and ~~Figure~~ Fig. 2 (b)).

~~Sequence of reactions and calculations performed for each scheme (rows). In columns, the order (t*N*) and the mode (gas/aerosol) for each process is indicated. Dust and sea-salt particles are referred as *DU* and *SS*, respectively.~~

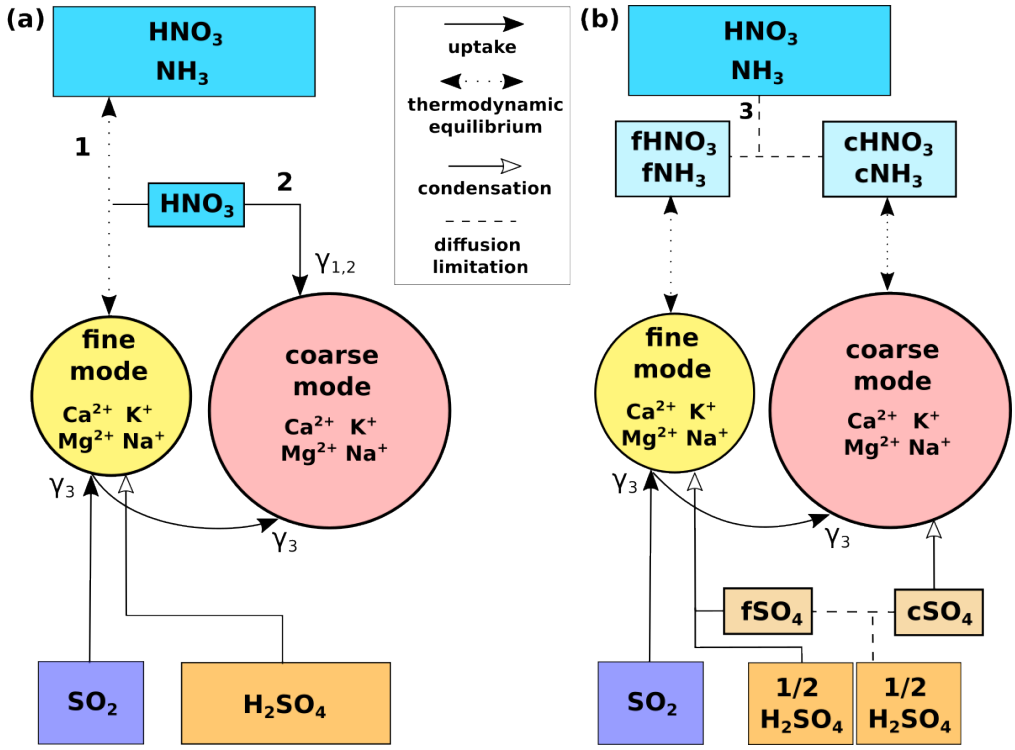

Figure 2. ~~Illustration~~ Scheme of the heterogeneous chemistry ~~schemes of~~ reactions on dust and SS developed in this work. (a) Schemes for the fTEQ and HYB mechanisms. (b) Scheme for DBCLL mechanism, that includes the kinetic diffusion limitation of gas species. The legend for line patterns is included on the center box. Numbers represent ~~fTEQ~~ (1) fTEQ, ~~HYB~~ (2) HYB and ~~DBCLL~~ (3) DBCLL. In the bottom~~part~~, the pathways for processing $SO_{2(g)}$ and $H_2SO_{4(g)}$ gases for each scheme are represented; ~~Namely,~~ $SO_{2(g)}$ is uptaken by fine particles and the remaining gas is uptaken by coarse particles~~, while 50% of~~. For $H_2SO_{4(g)}$ ~~is assumed to nucleate~~, (a) the fTEQ and HYB mechanisms assume that it nucleates directly as fine SO_4^{2-}, while (b) DBCLL mechanism assumes that 50% of its concentration nucleates, and the rest is ~~either condensed as fine or~~ divided by diffusion limitation between fine and coarse modes, completely condensing on each of them. The uptake coefficients used for each uptake process (solid arrows) are indicated as $\gamma_{1,2}$ for $HNO_{3(g)}$ uptake on dust ~~, for uptake on~~ and SS, and γ_3 for $SO_{2(g)}$ uptake on dust.

Experiment	Fine TEQ	Coarse TEQ	Coarse DU UPTK	Coarse SS UPTK	DIFFLIM	DU Alk.	SS Alk.
noHC							
fTEQ_noAlk							
fTEQ_du-ssAlk						J	
HYB_duUPTK						J	
HYB_du-ssUPTK						J	
HYB_DL						J	
HYB_g0p1						J	
DBCLL_noAlk							
DBCLL_duAlk						J	
DBCLL_du-ssAlk						J	
DBCLL_ClaqAlk						C	

Table 3. The sensitivity experiments conducted in this study and ~~their~~ the processes performed in each one of them (green boxes). *Fine TEQ* and ~~*coarse TEQ*~~ *Coarse TEQ* refer to the respective calculation of the TEQ on the fine and coarse modes of dust and SS, referred as *DU* and *SS*, respectively. *Coarse DU UPTK* and *Coarse SS UPTK* indicate the irreversible UPTK of $HNO_{3(g)}$ on coarse dust and SS, respectively. Alkalinity is denoted as *Alk.* and for the dust alkalinity column, alkalinity derived from the Journet et al. (2014) and Claquin et al. (1999) simulations is indicated by *J* and *C*, respectively.~~The experiments are grouped by sets of runs as described in Section 2.5.~~

2.4 ~~Experimental setup~~Sensitivity runs

We performed global simulations based on the mechanisms described in Section 2.3~~(Table 3)~~. Overall, ~~twelve different runs~~ eleven different runs (Table 3) are analyzed to test different degrees of complexity and sensitivity to parameterizations when simulating heterogeneous chemistry of dust~~and SS~~, such as the hypothesis on reversibility on nitrate formation, and the role that dust ~~and SS~~ (and SS) alkalinity play in the partitioning of gas and aerosol species. Unless stated to the contrary, all the experiments employ dust alkalinity derived from the average of the Journet et al. (2014) simulation, as explained in Section 2.2.3.

Three initial run sets are conducted ~~to establish reference results for comparison when~~ neglecting coarse NO_3^- formation, serving as a comparison reference for following experiments including coarse NO_3^- ~~formation is neglected;~~ . The noHC run assumes that there is no formation of NO_3^-, NH_4^+ or SO_4^{2-} aerosol through heterogeneous chemistry on ~~dust and SS~~any aerosol particle, serving as a baseline to estimate the burden of gas condensing in particles in other configurations and the influence of particle formation on nitrogen deposition rates. Additionally, two ~~fTEQ runs~~ sensitivity experiments with fTEQ are included to discuss the impact of ignoring the partitioning of semivolatile inorganic species on coarse particles~~. Specifically,~~ : fTEQ_noAlk neglects the presence of dust or SS in the aerosol mixture (R6-7 in Table 1), while fTEQ_du-ssAlk considers TEQ between gas and NVC in the fine modes of dust and SS particles (R6-12 in Table 1).

Next, we addressed the condensation of nitrate across the entire particle size range with runs employing the HYB and DBCLL mechanisms. ~~The HYB approach simplifies nitrate condensation on the coarse mode assuming an irreversible UPTK reaction.~~ We conducted two ~~runs~~ sensitivity runs with the HYB mechanism to explore the ~~sensitivity~~ impact of implementing

the $HNO_{3(g)}$ UPTK reaction on coarse dust only (HYB_duUPTK, reaction R4 from Table 1)) and on both coarse dust and SS (HYB_du-ssUPTK, reactions R4 and R5), comparing their results to assess the relative ~~contribution of~~ contributions of dust and SS in heterogeneous chemistry under the assumption of $HNO_{3(g)}$ irreversible UPTK on the coarse mode.

In the HYB approach, all $HNO_{3(g)}$ and $NH_{3(g)}$ concentrations are initially available to condense in the fine mode through TEQ reactions. Only the remaining $HNO_{3(g)}$ after the TEQ calculation is considered for UPTK reactions in the coarse mode. This assumption may potentially lead to a misrepresentation of fine and coarse NO_3^- formation, such as the underproduction of fine and overproduction of coarse NO_3^- (Feng and Penner, 2007; Hauglustaine et al., 2014; Bian et al., 2017; Jones et al., 2021). To address this potential limitation, an additional simulation (HYB_DL) was conducted using the DIFFLIM calculation to distribute the $HNO_{3(g)}$ and $NH_{3(g)}$ gas that is kinetically available for condensation in the fine mode through TEQ and the $HNO_{3(g)}$ that can form coarse NO_3^- through UPTK reactions.

Furthermore, to assess the influence of the ~~UPTK coefficient on~~ UPTK coefficient of $HNO_{3(g)}$ on the results, instead of using a RH function (see Section 2.2.1) we also conducted a simulation setting $\gamma(HNO_3) = 0.1$ for dust (HYB_g0p1), following experimental findings (Fenter et al., 1995; Hanisch and Crowley, 2001, 2003) and various modelling studies (Dentener et al., 1996; Liao et al., 2003; Bauer et al., 2004; Hodzic et al., 2006; Bauer et al., 2007; Feng and Penner, 2007).

Finally, we conducted four sensitivity simulations using the DBCLL mechanism, which accounts for reversible heterogeneous nitrate chemistry both on fine and coarse modes. These simulations evaluate the influence of alkalinity, including the DBCLL_noAlk run ~~excluding~~ that excludes both dust and SS NVC content ~~,~~ (reactions R6-7, Table 1), the DBCLL_duAlk run accounting ~~only~~ for dust alkalinity only (reactions R8-11), and the DBCLL_du-ssAlk run accounting for both dust and SS alkalinity (reactions R8-12). Additionally, since all three cases use dust alkalinity from the average of the Journet et al. (2014) simulation, an ~~extra~~ additional simulation was performed using the average dust alkalinity from ~~the average~~ Claquin et al. (1999) simulations (DBCLL_Claq), instead of Journet et al. (2014), to assess the effect of the specific dust alkalinity content used.

2.5 Experimental setup

The model simulations were conducted on a global domain at a spatial resolution of 1.4 degrees longitude by 1.0 degree latitude, utilizing 48 hybrid pressure-sigma vertical layers up to 5hPa. The dynamics timestep was set to 180s and results were stored every 6 hours. The analysis period is ~~the~~ year 2018 after a spin-up period of half a year to initialize the concentration fields. Meteorological variables were initialized from the ERA5 reanalysis (Hersbach et al., 2023) every 24h to keep the modeled circulation close to observations. A meteorological spin-up of 12h was used in each daily cycle before solving the chemistry. The initial state of the chemistry fields are those prognostically calculated by MONARCH the day before.

In addition to the meteorology-driven online emissions described in Sect. 2.1, the High-Elective Resolution Modelling Emission System version 3 (HERMESv3; Guevara et al., 2019) was employed to process both anthropogenic and biomass burning primary emissions. The global inventory CAMS-GLOB-ANT_v4.2 (Soulie et al., 2024) for 2016 was used for anthropogenic sources with updated temporal profiles that provide gridded monthly, day-of-the-year, day-of-the-week and hourly weight factors for the temporal disaggregation of emitted fluxes (Guevara et al., 2021). The biomass burning emissions are provided

by the GFASv1.2 dataset (Kaiser et al., 2012), which accounts for forest, grassland, and agricultural waste fires derived from satellite products. Oceanic natural emissions of DMS are provided by CAMS-GLOB-OCE_v3.1 (Lana et al., 2011; Denier van der Gon et al., 2023).

Table S1 summarizes the total emissions (anthropogenic, biogenic and biomass burning) used in this work. The emitted mass of the main anthropogenic aerosol precursors are 104.4 Tg for $SO_{2(g)}$, 93.8 Tg for $NO_{x(g)}$, and 61.8 Tg for $NH_{3(g)}$.

2.6 Model evaluation

The model results are evaluated against surface observational datasets from several networks sourced from the Globally Harmonised Observational Surface Treatment (GHOST) project, an initiative of the BSC's Earth Department dedicated to the harmonisation of publicly available global surface observations (Bowdalo et al., 2024). ~~Supplementary~~ Figure S13 in the Supplement shows the stations used for each of the species analyzed. For gas and aerosol nitrate, ammonia and sulfate species, GHOST include datasets from the Clean Air Status and Trends Network (US-EPA-CASTNET), the US EPA Air Quality System (US-EPA-AQS) and the Canada National Air Pollution Surveillance Program (NAPS) for North and Central America, the East Asia Acid Deposition Monitoring Network (EANET) for Asia, and the EBAS and the European Environmental Agency Air Quality (EEA AQ eReporting) for Europe.

These observations are filtered for rural and background sites only, in order to exclude stations near emission sources not representative of the background conditions depicted by the model resolution, which describes the long-range transport of NO_3^-, NH_4^+ and SO_4^{2-} formation. However, information on the station type was not available for the EANET and US-EPA-CASTNET data. For these networks, all stations were used, a factor that has to be accounted for when evaluating the results.

Regarding $PM_{2.5}$ and PM_{10}, GHOST includes data from the CHILE-SINCA network for Chile, the Beijing Municipal Ecological and Environmental Monitoring Center (BJMEMC), the China National Environmental Monitoring Centre (CNEMC), WMO World Data Center for Aerosols (EBAS-WMO-WDCA) for Europe, the Japan National Institute for Environmental Studies (NIES), the Ministerio de Transición Ecológica (MITECO) for Spain, the UK AIR network for United Kingdom, and the global AirNow DOS network (US-EPA-AirNow-DOS). For these networks, the station type was not included as a criteria to include it in the evaluation. The statistical metrics used in the evaluation are outlined in the Supplementary Section S3, and the quality flags for the selected stations in Table S8.

Additionally, we compare our model results with the budgets reported in the literature (Hauglustaine et al., 2014; Bian et al., 2017; Rémy et al., 2022). Namely, the AeroCom phase III nitrate experiment (Bian et al., 2017) intercompares global NO_3^- budgets from nine global models for the year 2008. Particular discussion is devoted to results shown there for the GMI Bian et al. (2009) and EMAC (Karydis et al., 2016) models, that introduce relevant approaches of interest to our work. ~~Complementary~~Complementarily, results from Hauglustaine et al. (2014) and Rémy et al. (2022) are also used. The comparison provides a qualitative view of current estimates of particulate NO_3^- formation in the atmosphere and the role of representing key processes in models. Since results from the literature are provided for different years, some of the differences may be attributed to changes in emissions and environmental conditions.

3 Results and discussion

3.1 Spatial distributions

The ~~global~~ spatial distribution of nitrate species ~~varies significantly based on the formation mechanisms assumed. We present the results by incrementally increasing complexity to assess the impact of each specific formation process on the global nitrate distribution. Initially, we neglect the formation of coarse~~ exhibits significant variability depending on the assumed formation mechanisms. Here, we analyze the results of the main sensitivity runs, arranged in order of increasing complexity as detailed in Section 2.4. These simulations range from a basic scenario that considers only fine NO_3^- ~~, focusing solely on nitrate formation in the fine mode. This is driven by pure nitrate-ammonia-sulfate neutralization (reactions R6-7 in Table 1), both with and without considering the effect of fine dust and SS alkalinity (reactions R8-12 in Table 1).We then discuss the formation of coarse~~ formation while excluding dust and sea-salt alkalinity (i.e. fTEQ), to a comprehensive approach that incorporates reversible NO_3^- ~~on dust and SS particles, considering both irreversible uptake processes (reactions R4-5) and reversible condensation processes (reactions R8-R12).~~ formation in both fine and coarse modes (i.e. HYB and DBCLL).

Spatial distributions of surface ~~concentrations, column loads~~ concentration, column load and zonal average ~~concentrations are~~ concentration for all sensitivity simulations (see Table 3) are averaged for 2018 and presented for $HNO_{3(g)}$ and particulate NO_3^- (~~Figure 3, Figure~~ Fig. 3, Fig. S1, and ~~Figure~~ Fig. S2 in the Supplement), $NH_{3(g)}$ and NH_4^+ (~~Figure~~ Fig. S4, ~~Figure~~ Fig. S5, and ~~Figure~~ Fig. S6 ~~), and~~ in the Supplement), as well as $SO_{2(g)}$ and SO_4^{2-} (~~Figure~~ Fig. S7, ~~Figure~~ Fig. S8, and ~~Figure~~ Fig. S9 ~~)~~in the Supplement). To facilitate readability, the analysis of the HYB_g0p1, DBCLL_duAlk and DBCLL_ClaqAlk runs is provided in Supplementary Section S5. ~~These results from the different sensitivity runs (see Table 3) are averaged for 2018.~~

3.1.1 Effects of omitting coarse nitrate formation

~~The~~ In the fTEQ_noAlk sensitivity run~~employs the TEQ model to form exclusively in the fine mode (fTEQ). In this scenario, and condensation is calculated without considering dust and SS alkalinity in the bulk aerosol phase, focusing only on pure nitrate-ammonia-sulfate neutralization (reactions R6-7 in Table 1). Fine~~ , fine particulate NO_3^- primarily forms ~~near~~ in regions with significant ~~anthropologic pollution,~~ anthropogenic pollution— areas where emissions of $NO_{x(g)}$, $NH_{3(g)}$, and $SO_{2(g)}$ are dominant~~, —~~such as Northern China, India, Europe and eastern North America~~, with concentrations ranging from~~ . In these regions, NO_3^- reaches average concentrations of 2 to 10 $\mu g\ m^{-3}$ (~~Figure~~ Fig. 3e). At the surface~~level~~ , NH_4^+ is mostly associated with fine NO_3^-, presenting concentrations ~~of 1-3~~ between 1 and 3 $\mu g\ m^{-3}$ (~~Figure~~ Fig. 3e and ~~Figure~~ Fig. S4e in the Supplement). At higher altitudes, fine NH_4^+ also forms in the presence of dust and SS, ~~with~~ resulting in column burdens ranging from 1 to 3 $mg\ m^{-2}$ (~~Figure~~ Fig. S5 and ~~Figure~~ Fig. S8 in the Supplement). This ~~is due to~~ occurs because NH_4^+ ~~neutralizing~~ neutralizes particulate SO_4^{2-}, which forms ~~from the condensation of~~ when $H_2SO_{4(g)}$ and $SO_{2(g)}$ condense on fine dust and SS ~~.~~ particles.

The omission of dust and SS alkalinity ~~results in very low values of aerosol pH globally;~~ leads to globally low pH values. Over oceanic and dusty regions, ~~pH values range~~ aerosol pH typically ranges from 1 to 2, while in industrialized regions, such as Europe and Asia, pH values can reach up to 5 (~~Figure~~ Fig. 4a).

~~Including~~ Aerosol pH increases significantly when dust and SS NVC ~~neutralization, along with the nitrate-ammonia-sulfate neutralization process (reactions R8-12 of Table 1), significantly increases aerosol pH~~ are included in the fTEQ_du-ssAlk run (~~Figure~~ Fig. 4b). This effect is especially pronounced over the open ocean, where pH increases from 1 to 5, and over dust source regions such as the Sahara desert, where pH increases from 1 to 9. ~~The elevated pH notably affects the partitioning~~

Column burdens of $HNO_{3(g)}$ ~~, reducing its column burdens throughout the Northern Hemisphere~~ are notably affected by the elevated pH, decreasing by approximately 5 $mg\ m^{-2}$ across the Northern Hemisphere compared to the fTEQ_noAlk scenario (~~Figure~~ Fig. S1d, g ~~).~~

~~The fTEQ_du-ssAlk run has minimal impact on surface concentrations over land (Figure 3d, g). The concentrations decrease only~~ in the Supplement). This decline predominantly happens in the upper troposphere (above 500hPa, ~~Figure~~ Fig. S2d, g) where concentrations decrease by about 0.5 $\mu g\ m^{-3}$ ~~. However, the~~ (Fig. S2 in the Supplement). Conversely, column burdens of fine NO_3^- increase ~~significantly~~substantially, by more than 5 $mg\ m^{-2}$ over dusty regions such as the Saharan desert and Middle East (~~Figure~~ Fig. S1e, h). ~~This suggests that the condensation of on dust and SS during long-range transport is a key driver of nitrate formation in this scenario.~~ In remote oceanic ~~areas~~regions, fine NO_3^- column burdens increase by approximately 1 $mg\ m^{-2}$, with transoceanic transport at low latitudes showing column loads ranging from 4 to 7 $mg\ m^{-2}$ (~~Figure~~ Fig. S1h ~~).~~ in the Supplement).

At the surface, the inclusion of dust and SS alkalinity has a minimal impact on continental $HNO_{3(g)}$ concentrations (Fig. 3d, g). Surface fine NO_3^- concentrations of about 0.5 $\mu g\ m^{-3}$ are present across the equatorial belt, with higher values~~over remote dusty regions (~~, up to 2 $\mu g\ m^{-3}$~~), though~~ , over remote dusty regions. However, no significant increase ~~is observed over~~ in fine NO_3^- concentrations is simulated in polluted areas such as Europe and Asia ~~. These results indicate that~~ (Fig. 3e, h and Fig. S2e, h).

These results suggest that the condensation of $HNO_{3(g)}$ on dust and SS happens mostly during long-range transport, representing a key driver of nitrate formation in this scenario. They also indicate that incorporating reactions R8-12 increases fine NO_3^- ~~form predominantly~~ concentrations, with the majority forming on dust rather than on SS~~,~~. This is attributed to the relatively higher alkalinity of dust compared to SS, as derived from the Journet et al. (2014) dataset (see Sect. 2.2.3). ~~Overall, incorporating reactions R8-12 increases fine concentrations by approximately 0.5 $\mu g\ m^{-3}$ beyond polluted areas at ground level and across the equatorial belt (Figure 3e, h and Figure S2e, h). This increase is noteworthy and highlights the sensitivity of nitrate formation to the alkalinity of dust and SS, as it will be further demonstrated in the surface observational evaluation in Section 3.2.~~

3.1.2 Effects of assuming irreversible formation of coarse nitrate

~~A commonly employed strategy in atmospheric chemistry models to represent nitrate formation on coarse particles in global simulations is the incorporation of irreversible heterogeneous reactions. In this study, we examine the results of the HYB~~

~~sensitivity runs (detailed in the second block of Table 3, where fine formation is simulated using fTEQ (reactions R6-12 in Table 1), while different irreversible uptake reactions (and rates) are explored to model coarse (UPTK reactions R4 and R5 in Table 1). The HYB method excludes~~

The HYB methods exclude the possibility of ~~particulate~~ coarse NO_3^- ~~evaporation, potentially leading~~ evaporating back to the gas phase, which may lead to positive biases in ~~its global burdens.~~ global NO_3^- burdens.

~~The sensitivity run~~ In the HYB_duUPTK ~~focuses on~~ sensitivity run, coarse NO_3^- ~~formation~~ forms exclusively on dust, ~~utilizing reaction R4 while disabling any process related with SS particles (R5 disabled). This results in the redistribution of~~ redistributing the available $HNO_{3(g)}$ towards ~~the production of~~ coarse NO_3^- ~~in regions predominantly~~ production in regions affected by dust, such as the Middle East and East Asia~~, where column loads range on~~ . Coarse NO_3^- column loads average between 0.5-4.0 $mg\ m^{-2}$ across the Northern Hemisphere, ~~peaking at~~ with peaks reaching 10-20 $mg\ m^{-2}$ (~~Figure~~ Fig. S1 ~~ll~~ in the Supplement). Notably, this impact is less pronounced in the Saharan dust belt, where ~~the availability of~~ limited $HNO_{3(g)}$ ~~for~~ availability constrains coarse NO_3^- formation~~is limited~~. The production of coarse NO_3^- ~~coincides with~~ is accompanied by a modest reduction in fine NO_3^- column loads over dusty regions (around 1 $mg\ m^{-2}$) compared to the fTEQ_du-ssAlk simulation, ~~attributed to diminished~~ driven by availability of $HNO_{3(g)}$ for ~~fTEQ reactions~~fine NO_3^- formation. ~~Surface concentrations of coarse range from 2 to 10 $\mu g\ m^-3$ over China, India, and the Middle East (Figure 3 l). Long-range~~ The uptake of $HNO_{3(g)}$ significantly influences the long-range transport of NO_3^- ~~is significantly influenced by dust NVC loads~~, showcasing notable transatlantic and transpacific transport ~~of coarse (Figure~~ (Fig. S1 in the Supplement). This transport predominantly occurs below 800hPa, with concentrations around 1$\mu g\ m^{-3}$, ~~while~~ although lower concentrations of coarse NO_3^- are also discernible at altitudes up to 400hPa (~~Figure~~ Fig. S2 ~~).~~ in the Supplement). At the surface, coarse NO_3^- concentrations also increase, ranging from 2 to 10 $\mu g\ m^-3$ over regions such as China, India, and the Middle East (Fig. 3 l).

The HYB_du-ssUPTK run investigates the role of SS ~~is investigated~~ by enabling both R4 and R5 ~~in the HYB_du-ssUPTK run. In reaction R5, a constant uptake coefficient of on coarse SS (γ_{SS})of 0.05 is used, while in R4, the uptake coefficient on coarse dust (γ_{dust}) is parameterized following Fairlie et al. (2010) as a function of RH with an average value of $\gamma_{dust} = 5.3 \cdot 10^{-4}$, as discussed in section 2.2.1.~~ (Table 1). The uptake of $HNO_{3(g)}$ on SS enhances the formation of coarse NO_3^- over open ocean and those coastal areas affected by SS outbreaks (~~Figure~~ Fig. S11 ~~). Notably, surface~~ in the Supplement). Surface concentrations in Europe and North-America reach 1-2 $\mu g\ m^{-3}$, with regions exceeding 5 $\mu g\ m^{-3}$ significantly ~~extended (Figure~~ expanding (Fig. 3o). Coarse NO_3^- becomes also notable over West Siberia, East South-America and South Africa (0.5-1 $\mu g\ m^{-3}$) and over remote oceanic regions (0.2 $\mu g\ m^{-3}$)~~, with its presence extended~~ . Its presence extends to high altitudes in the Southern Hemisphere (~~Figure~~ Fig. S2o ~~). The long-range~~ in the Supplement). Long-range transport of coarse NO_3^- is enhanced ~~, particularly~~ over oceans, ~~compared to the HYB_duUPTK case,~~ with column burdens increasing by approximately 3.5 $mg\ m^{-2}$ (~~Figure~~ Fig. S1o ~~)~~in the Supplement), compared to the HYB_duUPTK case. This increase is attributed to ~~a higher~~ greater depletion of $HNO_{3(g)}$ ~~by irreversible reactions R4 and R5 (Figure~~ through irreversible uptake over dust and SS (Fig. S1m ~~). Consequently, the HYB_du-ssUPTK sensitivity run exhibits~~ in the Supplement), resulting in lower $HNO_{3(g)}$ concentrations in the atmosphere compared to the other simulations.

As previously noted, the γ_{dust} values used in both HYB_duUPTK and HYB_du-ssUPTK runs are well below the value used for γ_{SS} and other studies in the literature (Hauglustaine et al., 2014; Rémy et al., 2022). To assess the sensitivity to more efficient R4 production rates, the Results obtained by increasing the value of $\gamma(HNO_3)$ in HYB_g0p1 run employs a constant value for γ_{dust} of 0.1, rather than utilizing the RH-dependent function proposed by (Fairlie et al., 2010). Results indicate an increase in coarse formation in regions rich in dust (Figure S10), such as the Sahara desert, the Persian Gulf and East Asia (Figure S3c). Furthermore, a slight enhancement in the transport of scenario (Supplementary Section S5 and Fig. S3) provide insights into the nature of the coarse NO_3^- across northern latitudes is observed, despite lower dust concentrations in that region. This can be attributed to the predominant production of coarse on dust across continental Eurasia, followed by its transoceanic transport. While the inclusion of UPTK on SS enhances long-range transportat high altitudes to North America. Although rising the value of $\gamma(dust)$ leads to a significant increase , the HYB_g0p1 run shows a slight increase in coarse NO_3^- compared to HYB_du-ssUPTK, the changes are not excessively substantial, suggesting particularly over the Sahara and across the Atlantic and Pacific oceans. Although these differences are not major, they suggest that the availability of $HNO_{3(g)}$ may be the limiting factor in R4. Furthermore, the HYB mechanisms preferentially condense via TEQ in the fine mode and over SS through R5 in the coarse mode, rather than over coarse dust through R4, as noted here and also assessed in next sections.

A possible explanation for the excessive condensation of over dust and SS in the HYB mechanism might be the unrestricted availability of act as a limiting factor for coarse NO_3^- formation. To address this potential issue, we performed a sensitivity test using the DIFFLIM calculation on the HYB_du-ssUPTK run(HYB_DL

To further explore this phenomenon, we used the HYB_DL run, which is equivalent to HYB_du-ssUPTK run but constrains the available gas using the DIFFLIM calculation (see Methods). This approach limits availability for fine TEQ and coarse UPTK based on the particulate surface for each mode. The DIFFLIM methodology redistributes column and surface concentrations from the fine to the coarse mode, resulting results in coarse NO_3^- column burdens slightly just below those obtained in HYB_g0p1. Coarse formation rises particularly over the Sahara and across the Atlantic and Pacific oceans. This can be explained by The similarity between HYB_DL and HYB_du-ssUPTK can be attributed to two possible factors: 1) HYB_DL preserving conserves more $HNO_{3(g)}$ for reaction via reactions on coarse dust during long-range transport via reactions R4 and R5 in the (Table 1) or 2) an intrinsic overestimation of the uptake coefficients, leading to similar coarse NO_3^- formation rates regardless of the $HNO_{3(g)}$ available. This is further discussed in Section 3.2.

Overall, results show that the HYB mechanisms preferentially condense $HNO_{3(g)}$ via TEQ in the fine mode and over SS through R5 in the coarse mode, thereby enhancing its condensation rather than over coarse dust . through R4, as noted here and also assessed in subsequent sections.

Comparing A comparison of the spatial distributions obtained by models the EMEP, INCA and GMI models in Bian et al. (2017), that use a similar HYB approach which employ HYB approaches similar to our HYB_du-ssUPTK runin MONARCH, reveals similar trends. Both studies , reveals comparable trends. All models show significant formation of total NO_3^- (fine + coarse) over polluted regions, although our results, ranging from 10 to 25 $mg\ m^{-2}$, generally exceed the column loads reported by AeroCom models, ranging that range from 7 to 16 $mg\ m^{-2}$ compared to 10-25 $mg\ m^{-2}$ (Figure (Fig. S1n, o in

the Supplement). AeroCom models do not show such ~~a prominent~~ the pronounced transport of coarse NO_3^- across the North Atlantic ~~as~~ observed in our study~~(~~, with column burdens of 0.2-0.5 $mg\ m^{-2}$ ~~vs.~~ , compared to 4 $mg\ m^{-2}$ ~~, respectively). In Section 3.4 we delve into~~ in our results. Section 3.4 further investigates the excessive formation of particulate NO_3^- ~~formation~~ in the HYB mechanism in terms of the total nitrogen budget.

A closer comparison with Hauglustaine et al. (2014), using the LMDz-INCA model with ~~similar UPTK coefficients~~ UPTK reactions on dust and SS~~as in MONARCH (also utilizing a function of RH as in Fairlie et al. (2010))~~, shows strong agreement ~~, particularly~~ with our HYB_duUPTK run but not with HYB_du-ssUPTK. For instance, concentrations of total NO_3^- over polluted areas ~~are similar in both cases in terms of~~ in Hauglustaine et al. (2014) align with HYB_duUPTK in both geographical distribution and magnitude (14-20 $mg\ m^{-2}$ in HYB_duUPTK ~~compared to~~ vs. 10-20 $mg\ m^{-2}$ in Hauglustaine et al. (2014), ~~Figure~~ Fig. S1 ~~l). Hauglustaine et al. (2014) also observes~~ *l*). Similarly, Hauglustaine et al. (2014) simulates fine NO_3^- transport downwind of the Sahara and coarse NO_3^- across the ~~northern~~ North Atlantic, with column burdens around 1-2 $mg\ m^{-2}$, slightly below our HYB_duUPTK results of 1-5 $mg\ m^{-2}$~~for HYB_duUPTK. This resemblance of Hauglustaine et al. (2014) with the~~ . This preferential similarity of Hauglustaine et al. (2014) to HYB_duUPTK ~~- and not with~~ rather than HYB_du-ssUPTK~~run - can~~ , may be attributed to the $HNO_{3(g)}$ UPTK coefficient for SS employed ~~by Hauglustaine et al. (2014): Instead~~ in Hauglustaine et al. (2014). For this reaction, instead of a constant value as ~~implemented~~ used in HYB_~~duUPTK, it~~ du-ssUPTK, Hauglustaine et al. (2014) uses a function of RH ranging from $1 \cdot 10^{-3}$ to 0.1, ~~therefore forming less~~ leading to a lower NO_3^- ~~over SS than our HYB_du-ssUPTK run~~formation over SS in their model. This comparison ~~with Hauglustaine et al. (2014) might point at~~ suggests a potential overestimation of the UPTK coefficient ~~of~~ for $HNO_{3(g)}$ on SS in the HYB_du-ssUPTK simulation~~, conclusion that~~ . This conclusion is further discussed in the observational evaluation (Section 3.2) and ~~in~~ the budgets analysis (Section 3.4). ~~Additionally, while Hauglustaine et al. (2014) attributes transatlantic transport of particulate to the UPTK of on SS, our study relates north Atlantic transport of coarse with UPTK on dust rather than on SS, as indicated by its increased presence in the HYB_g0p1 simulation.~~ As a final remark, it is important to ~~take into account that, as Hauglustaine et al. (2014), also~~ note that, similar to the findings of Hauglustaine et al. (2014) , the HYB_duUPTK simulations overestimates particulate NO_3^- ~~when compared to observations, as explained~~ concentrations compared to observational data, as discussed in Section 3.2.

To further ~~elucidate~~ investigate the source of the coarse NO_3^- overestimation in the HYB_du-ssUPTK ~~overestimation of coarse~~ simulation, we compare our spatial distributions with those from Jones et al. (2021), which employs a similar HYB mechanism using the Met Office ~~Unite~~ Unified Model (UM). ~~Jones et al. (2021) computes~~ In Jones et al. (2021), fine NO_3^- formation ~~with~~ is computed using adaptations from Hauglustaine et al. (2014)~~(~~, specifically by testing different accommodation coefficients for $HNO_{3(g)}$ onto preexisting ammonium-nitrate aerosols~~, although reporting almost negligible effects~~ —though this adjustment has minimal impact on coarse NO_3^- concentrations~~) and forms coarse~~ . Coarse NO_3^- ~~from the~~ is formed through the uptake of $HNO_{3(g)}$ ~~UPTK using coefficients~~ , with coefficients sourced from Fairlie et al. (2010) for dust and Burkholder et al. (2020) for SS. ~~Consequently, its~~ Despite using different uptake coefficients for $HNO_{3(g)}$ on SS, the resulting coarse NO_3^- distribution is broadly comparable to that ~~obtained from~~ of the HYB_du-ssUPTK ~~run, despite using different coefficients for the UPTK on SS. Some differences arise between both models:~~ simulation. However, key differences emerge between the two

models. Compared to Jones et al. (2021), HYB_du-ssUPTK ~~reports significantly lower sub-Saharan concentrations of~~ exhibits a stronger tendency for coarse NO_3^- ~~, while showing higher formation of coarse~~ formation over polluted areas such as Europe, ~~east~~ eastern North-America and Asia (~~4 vs.~~ 8-20 $mg\ m^{-2}$ in HYB_du-ssUPTK vs. 4 $mg\ m^{-2}$ in Jones et al. (2021)), as well as over ~~oceans (0.4-2.0 vs.~~ oceanic regions (1.5-3.0 vs. 0.4-2.0 $mg\ m^{-2}$), rather than over sub-Saharan areas. Remarkably, ~~the~~ significant North-Atlantic transport of coarse NO_3^- (2.0-4.0 $mg\ m^{-2}$) is only present in our ~~study with 2.0-4.0 $mg\ m^{-2}$. Their results, when compared with the HYB_duUPTK simulation , also show lower coarse concentrations over North-America (2-3 vs. 1-2 $mg\ m^{-2}$).~~

~~Furthermore, a~~ simulation and is absent in Jones et al. (2021). The global budget comparison ~~between HYB_duUPTK and Jones et al. (2021) indicates similar high coarse~~ in Section 3.4 and Table 5 further highlights that Jones et al. (2021) reports significantly lower global NO_3^- ~~formation in both models~~burdens compared to our HYB runs, including HYB_duUPTK. This suggests ~~a possible excessive formation of~~ that the HYB mechanisms in our simulations may excessively produce coarse NO_3^- ~~in HYB_duUPTK~~, as both ~~models exhibit similar~~ the burdens and distributions of coarse NO_3^- ~~, albeit Jones et al. (2021) also includes SS in its formation. However~~in Jones et al. (2021) are consistently lower, despite also accounting for SS in nitrate formation.

Nevertheless, several alternative explanations could account for the differences between ~~both modelscould be considered, including variations~~ the models. These include differences in the fine NO_3^- formation mechanism, ~~differences~~ variations in the study period (2018 ~~vs.~~ in our study vs. a 20-year ~~period~~average in Jones et al. (2021)), and ~~differences in the parameterization~~ differing parameterizations of $HNO_{3(g)}$ ~~UPTK~~ uptake on SS. ~~Detailed budget comparisons are presented in Section 3.4.~~

Overall, the comparison of spatial distributions between our HYB mechanisms and those reported in the literature support the initial hypothesis that the assumption of irreversible $HNO_{3(g)}$ uptake, and potentially the uptake coefficients used, may contribute to the overestimation of NO_3^- formation. This issue is examined in greater detail in Sections 3.2 and 3.4.

3.1.3 Effects of accounting for reversible formation of coarse nitrate

~~Advancing the representation of dust and SS heterogeneous chemistry in models involves incorporating the partitioning of semivolatile inorganic species as a fully reversible process across all particle sizes. To explore the implications of this advancement, we conducted sensitivity runs using the DBCLL mechanism, as introduced in Section 2.3. The DBCLL runs (outlined in Table 3) are designed to~~

The DBCLL simulations (described in Section 2.4 and Tables 2 and 3) assess the impact of ~~the~~ reversible chemistry and ~~sensitivities associated to~~ the role of dust and SS NVC ~~participation in the~~ in nitrate partitioning.

~~Firstly, in the~~ The DBCLL_noAlk ~~sensitivity run , formation is exclusively considered through reactions R6-7 (see Table 1). Here, the mass of dust and SS serves solely to determine the available particle surface area in the DIFFLIM calculation, with alkalinity not factored into the partitioning assessment. Notably, the~~ run produces spatial distributions of $HNO_{3(g)}$ and fine NO_3^- ~~in the DBCLL_noAlk run closely resemble~~ similar to those in the fTEQ_noAlk run. $HNO_{3(g)}$ remains predominantly in the gas phase across the Northern Hemisphere (~~Figure~~ Fig. S1p ~~). Fine~~ in the Supplement), while fine NO_3^- primarily associates with fine NH_4^+ ~~in regions without~~ over regions lacking dust or SS influence, such as parts of China, India, Europe

and ~~east~~ eastern North-America (~~Figure~~ Fig. 3q)~~, with minimal concentrations of~~ . Minimal concentrations of fine NO_3^- are simulated at higher altitudes (~~Figure~~ Fig. S2q ~~). Conversely,~~ in the Supplement), though fine NH_4^+ ~~is present at elevated altitudes alongside sulfate particles , similar to the findings~~ coexists with sulfate particles at elevated levels, as observed in the fTEQ_du-ssAlk case. In contrast, coarse NO_3^- is nearly absent in ~~the~~ DBCLL_noAlk~~run, with minimal concentrations observed at the surface level~~ , with only minimal surface concentrations over northern China ~~at~~ (0.4 $\mu g\ m^{-3}$~~, showing no apparent correlation with the presence of~~) and no clear correlation with dust and SS (~~Figure~~ presence (Fig. 3r). ~~Similarly, the formation of coarse~~ Coarse NH_4^+ ~~is very~~ formation is similarly limited, with ~~some~~ slight presence over the Persian Gulf and the Sahara (0.02-0.1 $mg\ m^{-2}$~~column loads~~), primarily in anthropologically polluted ~~areas,~~ regions where it forms alongside coarse SO_4^{2-} ~~at~~ (0.2 $mg\ m^{-2}$~~(Figure~~) (Fig. S5r and ~~Figure~~ Fig. S8r). The simultaneous formation of coarse NH_4^+ and SO_4^{2-} particles ~~can be~~ is attributed to diffusion limitation, ~~which allocates~~ where $NH_{3(g)}$ ~~to neutralize sulfate particlespresent in the coarse mode~~preferentially neutralizes coarse sulfate particles.

The differences between fTEQ_noAlk and DBCLL_noAlk illustrate the impact of ~~assuming the~~ diffusion limitation before the partitioning of semi-volatile species. While fine NO_3^- formation remains consistent between both runs, the assumption of allowing all acid species to ~~be available for partitioning~~ partition into the fine mode in fTEQ_noAlk ~~results in~~ leads to enhanced fine particle production and long-range transport~~, which is~~ —an effect not observed in DBCLL_noAlk. Consistently, the pH in the fine mode closely mirrors that of fTEQ_noAlk, while the pH of particles in the coarse mode indicates even greater acidity (~~Figure~~ Fig. 4f1, f2)).

~~The impact of dust NVC on the DBCLL mechanism is introduced through reactions R8-11 (Table 1) in the DBCLL_duAlk sensitivity run. Compared with DBCLL_noAlk, dust alkalinity significantly increases pH values (i.e. more basic) over the Sahara and continental Asia to a range of 6 to 8 (Figure 4g1, g2), thereby enhancing the formation of both fine and coarse as well as coarse in these regions. Additionally, fine formation is amplified in polluted areas, with surface concentrations rising beyond 5 $\mu g\ m^{-3}$ (an increase of 2-5 $\mu g\ m^{-3}$ relative to DBCLL_noAlk). This enhanced formation extends to regions rich in coarse dust, such as the Persian Gulf (surface concentrations of 1-3 $\mu g\ m^{-3}$) and central/downwind areas of the Saharan desert (surface concentrations of 0.2-0.5 $\mu g\ m^{-3}$ and loads of 2.0 $mg\ m^{-2}$), as shown in Figures 3u and S1u. Over these areas, DBCLL_duAlk nearly depletes gas (remaining surface concentrations of 0.01 to 0.05 $\mu g\ m^{-3}$). At high altitudes, both fine and coarse are distributed across the Atlantic and Pacific oceans with column loads of 1-2 $mg\ m^{-2}$ (Figure S1u), resembling the transoceanic patterns also observed in the HYB mechanisms. Conversely, compared to the DBCLL_noAlk run, fine increases over Europe and North-Central America (by at least 1 $mg\ m^{-2}$, discussed in Section 3.3.1), while it decreases over dusty areas (by 1.0 to 2.0 $mg\ m^{-2}$, Figure S5t, q). This pattern is consistent with the comparison between the fTEQ_noAlk and the fTEQ_du-ssAlk runs (Figure S5h, e). Concurrently, coarse formation increases significantly in transoceanic areas, reaching 0.08-0.1 $mg\ m^{-2}$ alongside coarse particles, although its formation is halted over dusty regions (i.e. Middle East and Sahara, Figure S5u). This inhibition can be attributed to the increased alkalinity of dust, which neutralizes and limits the condensation of . Lastly, the introduction of dust alkalinity strongly enhances the formation of coarse , both over polluted regions (5 $mg\ m^{-2}$) and remote areas (0.2-1.0 $mg\ m^{-2}$), as shown in Figure S8. The enhanced production of coarse particles (principally coarse) provides additional surface area for to condense on.~~

~~We also incorporated the effect of SS NVC into the nitrate formation adding reaction R12 (Table 1) in the~~ Including dust and SS alkalinity in DBCLL_du-ssAlk ~~run. Considering both dust and SS alkalinity~~ produces an important increase in ~~oceanic~~ ~~pH ,~~ the pH over arid regions and oceanic regions—from 1 to 5-6 in the fine mode and above 7 in the coarse mode~~(Figure —~~compared to DBCLL_noAlk (Fig. 4h1, h2)~~and redistributes the partitioning towards the coarse mode. Compared~~. Relative to DBCLL_du-Alk (~~which accounts only for dust alkalinity),~~ dust alkalinity only, see Supplementary Section S5), DBCLL_du-ssAlk redistributes the NO_3^- partitioning toward the coarse mode: fine NO_3^- concentrations ~~areapproximately halved across all~~ approximately halve across regions, while coarse NO_3^- surface concentrations and column loads roughly double ~~(Figure~~ over dusty regions but not over the ocean (Fig. 3w, x and ~~Figure~~ Fig. S1w, x). ~~Concentrations of coarse are remarkable in the~~ This shift leads to enhanced transatlantic and transpacific transport, with column loads of 2-4 $mg\ m^{-2}$, surface concentrations of 0.4 $\mu g\ m^{-3}$ and zonal ~~average~~ averages of 0.5-1.0 $\mu g\ m^{-3}$~~)~~. Over continental ~~areas with elevated coarse~~ regions with dust concentration, coarse NO_3^- ~~column loads reach~~ reaches column loads of 4-5 $mg\ m^{-2}$ and surface concentrations ~~are~~ of 0.5-1.0 $\mu g\ m^{-3}$. ~~This increase is accompanied by a rise in~~ Additionally, $HNO_{3(g)}$ surface concentrations ~~,~~ increase from 0.1 to 1.0 $\mu g\ m^{-3}$ in the ~~main~~ heavily polluted areas (~~Figure~~ Fig. 3s, v). The ~~inclusion of both dust and SS alkalinity in the coarse TEQ calculation enhances coarse~~ enhancement of coarse NO_3^- formation ~~directly over and downwind of dusty areas, compared to accounting for dust alkalinity alone (DBCLL_duAlk). This enhancement can be attributed by SS NVC - such as~~ is attributed to SS NVC (see Section 2.2.3)~~- halting~~ , with Cl^- suppressing fine NO_3^- formation ~~,~~ and leaving more $HNO_{3(g)}$ ~~in the gas phase to be transported over dusty regions, where it subsequently forms~~ available for transport and subsequent coarse NO_3^- ~~.~~ formation over dusty regions.

~~The spatial distributions of coarse in the DBCLL runs show a significant contrast compared to those obtained with the HYB runs. Formation is concentrated directly over and downwind of dusty areas, rather than over anthropologically polluted areas as seen when using HYB mechanisms. For example, in the DBCLL_du-ssAlk, surface concentrations over Europe do not exceed 0.5 $\mu g\ m^{-3}$ (Figure 3x).~~ Including SS alkalinity ~~causes~~ reduces fine NH_4^+ loads ~~to decrease~~ over Europe and Eastern ~~North America~~ North America from 3 to 1 $mg\ m^{-2}$ ~~, while slightly lower values are reported~~ and slightly lowers values over Asia (~~at~~ 2-3 $mg\ m^{-2}$)~~, likely due to the reduced presence of fine~~ . Conversely, coarse NH_4^+ ~~formation is substantially enhanced~~ increases over Europe and Eastern ~~North America~~ North America (0.1-0.2 $mg\ m^{-2}$), Asia (~~reaching~~ up to 1.0 $mg\ m^{-2}$), and transoceanic regions (0.1 $mg\ m^{-2}$) (~~Figure~~ Fig. S5x ~~). Although the presence of coarse increases over the Sahara and the Middle East, this may be a consequence of long-range transport from polluted areas. The decrease in fine and the increase in coarse are directly related to the~~ in the Supplement). This redistribution mirrors the particulate NO_3^- patterns, ~~outlining the strong correlation~~ highlighting the strong coupling between these species when TEQ is ~~employed for~~ applied to both fine and coarse ~~gas-aerosol partitioning. This emphasizes the important role of the basic NVC from SS particles (i. e.), illustrating the sensitivity of the results to the inclusion of SS alkalinity~~partitioning. These results emphasize the sensitivity of nitrate formation to SS alkalinity, particularly due to basic NVCs like Na^+.

Compared to the HYB_du-ssUPTK run, DBCLL_du-ssAlk shows lower coarse NO_3^- concentrations and shifts coarse NO_3^- formation toward dusty rather than anthropologically polluted areas. For example, over Europe, surface concentrations in DBCLL_du-ssAlk do not exceed 0.5 $\mu g\ m^{-3}$, while HYB_du-ssUPTK reports 1-2 $\mu g\ m^{-3}$ (Fig. 3x).

Overall, ~~the major sensitivity identified in the intercomparison of mechanisms is attributed to~~ regardless of the mechanism used, the results demonstrate the high sensitivity of NO_3^- formation to dust and SS alkalinity, significantly altering its spatial distribution (reactions R8 to R12, ~~where the alkalinity of dust and SS modifies dramatically spatial patterns. The changes observed across the different mechanisms analyzed are consistent and highly sensitive to the presence of NVC in the partitioning of semi-volatile species. The sole inclusion of the~~ Table 1). However, implementing the DIFFLIM calculation in the DBCLL mechanism has a ~~minor~~ limited impact, as shown by the comparison ~~of the~~ between fTEQ_noAlk and DBCLL_noAlk~~runs. An additional simulation was conducted to explore the sensitivity of formation specifically on dust alkalinity using a different mineralogical dataset. Specifically, we derived the average alkalinity of dust from Claquin et al. (1999) mineralogical dataset instead of Journet et al. (2014), DBCLL_ClaqAlk run (Table 3), as detailed in Section 2.2.3. The results of this run show significant differences in specific arid regions compared with DBCLL_du-ssAlk. Notably, load increases substantially over the Middle East and northern India, while a slight reduction is observed over northern Africa. These changes are significant enough to impact the long-range transport of both fine and coarse across the northern hemisphere (Figure S3k, l). Coarse decreases by about 1-2 $mg\ m^{-2}$ over and downwind of dusty areas, while fine increases by 2-5 $mg\ m^{-2}$ along the equatorial belt and over polluted regions. Similar differences are found in particulate , although with an order of magnitude lower. Notably, distributions report negligible differences between both runs. The lower alkalinity derived from the Claquin et al. (1999) dataset accounts for these differences, primarily affecting the formation of during long-range transport of dust. This is further discussed in the following section 3.4.~~ .

~~It is insightful to compare the~~

We compare DBCLL_du-ssAlk and the results from the ~~DBCLL_du-ssAlk run with those from the~~ EMAC model (Karydis et al., 2016), which ~~employs a similar configuration to DBCLL, but first performing the~~ similarly employs TEQ for the bulk gas and aerosol mass, ~~and subsequently redistributing the concentrations with the DIFFLIMcalculation~~followed by DIFFLIM. Additionally, EMAC makes use of globally heterogeneous dust alkalinity based on 12 mineralogy source data points. Results from the EMAC model are reported in Bian et al. (2017) and Karydis et al. (2016) (Table 5 and Supplementary Section S4). Surface distributions of aerosol NO_3^- are closely aligned in both models over Europe and North America, with surface concentrations ranging from 1 to 3$\mu g\ m^{-3}$. However, DBCLL_du-ssAlk ~~tends to present higher~~ shows higher concentrations over Asia, India and Middle East compared to ~~the EMAC averages for those regions~~ EMAC (5-10$\mu g\ m^{-3}$ vs. 6-15$\mu g\ m^{-3}$, respectively). Additionally, our results show some variations over secondary areas compared to Karydis et al. (2016). ~~For instance, Karydis et al. (2016) reports various deviations to observations, like~~ EMAC reports biases, such as underestimating coarse NO_3^- ~~underestimation over continental regions such as southern Europe ,~~ over southern Europe and central-east Asia, ~~Middle East, and south-west USA. In the study, these deviations to observations are attributed to high concentrations of condensed on dustparticles over those areas, a problem~~ attributed to excessive sulfate condensation on dust—a limitation mitigated in our study ~~since it presents lower sulfate concentrations over these regions (Figure S7). Another bias with observations noted in Karydis et al. (2016) is the elevated~~ due to lower sulfate levels (Fig. S7 in the Supplement). Additionally, while EMAC overestimates fine NO_3^- ~~formation~~ over the Arctic, ~~a phenomenon~~ this is not observed in our ~~case, likely~~ results due to the ~~restriction of~~ RH and temperature ~~when using~~ restrictions applied in ISORROPIA-II ~~for TEQ~~ (see Section 2.2.2).

~~Additionally, Karydis et al. (2016) noted that their results overestimated~~ Over central Africa, EMAC overpredicts coarse NO_3^- ~~in central Africa (1-2 $\mu g\ m^{-3}$ surface concentrations)~~ due to excessive $HNO_{3(g)}$ from biomass burning coupled with low ~~concentrations. They suggested that an~~ $H_2SO_{4(g)}$ concentrations, from where Karydis et al. (2016) suggested that a HYB approach could ~~solve this bias. In our case we report much lower values of coarse over central Africa, both with the~~ reduce the bias. Our DBCLL_du-ssAlk ~~(0.3-1.0 $\mu g\ m^{-3}$) and with the HYB mechanisms (0.3-0.8 $\mu g\ m^{-3}$). However, since we do not register high concentrationsover that region in the baseline simulation noHC (with 0.04-0.1 $\mu g\ m^{-3}$, Figure 3a) compared to Karydis et al. (2016), it indicates that we might be overestimating coarse over central Africa with both DBCLL and HYB mechanisms. This implies that the HYB mechanism might not be a solution to improve coarse predictions over that area. In this context, total~~ and HYB runs report lower concentrations, though still potentially overestimated due to too low $HNO_{3(g)}$ levels. Total particulate SO_4^{2-} and NH_4^+ are in close agreement in both EMAC and the DBCLL_du-ssAlk run (~~Figures~~ Fig. S4w, x and S7w in the Supplement, x), with only slightly higher formation of coarse NH_4^+ over the India peninsula in MONARCH compared to EMAC~~(2.5-3.0 $\mu g\ m^{-3}$ vs. 0.9-2.0 $\mu g\ m^{-3}$, respectively).~~ .

3.2 Evaluation with observations

~~We evaluate~~ To assess the performance of each sensitivity run~~by comparing with measured~~ , we compare simulated surface concentrations of ~~relevant~~ key species involved in nitrate formation ~~, as detailed~~ with observational data, as described in Section 2.6. This evaluation includes ~~an analysis of~~ analyses of both statistics and time series of monthly mean values, focusing on ~~the ability of the various mechanisms under study to capture~~ how effectively each modeled mechanism captures observed nitrate variability ~~across the globe. The globally~~ on a global scale. Globally averaged results are shown in ~~Figure~~ Fig. 5, while ~~regionalized results~~ regio-specific evaluations for Europe, Asia, and Central-North America are presented in ~~Figure~~ Fig. S12 in the Supplement. It is important to note that the number of stations and spatial coverage vary significantly ~~depending on the type of~~ by species, as illustrated in ~~Figure~~ Fig. S13. Consequently, certain evaluation metrics may not ~~be representative of the model 's performanceglobally, and might only reflect accuracy within specific regions. The correlation~~ fully reflect global model performance, and could instead represent accuracy in data-rich regions.

Correlation coefficients, bias and RMSE metrics ~~(Section S3)~~ for the different sensitivity simulations are reported in Table 4~~.~~ , with methodological details outlined in Supplementary Section S3. A detailed evaluation of the HYB_g0p1, DBCLL_duAlk and DBCLL_ClaqAlk simulations is available in Supplementary Section S5. Additionally, a similar evaluation for total reduced and oxidized nitrogen species is presented in Supplementary Section S6 and further discussed in Section 3.3.2.

3.2.1 Nitrate species

Fine particulate nitrate ($PM_{2.5}NO_3$) is ~~formed in the same way among~~ consistently formed across all mechanisms (through TEQ), with the exception of DBCLL ~~that implements~~ scheme, which incorporates a DIFFLIM coefficient to limit its formation. ~~The~~ Consequently, the fTEQ and HYB mechanisms ~~present~~ produce higher $PM_{2.5}NO_3$ from October to April (0.5-1.0 $\mu g\ m^{-3}$) than DBCLL, which reports approximately half of ~~the concentration. This gap~~ these values. This discrepancy is more pronounced over North and Central America than ~~over~~ in Europe, although both ~~present a similar pattern. Differences among~~

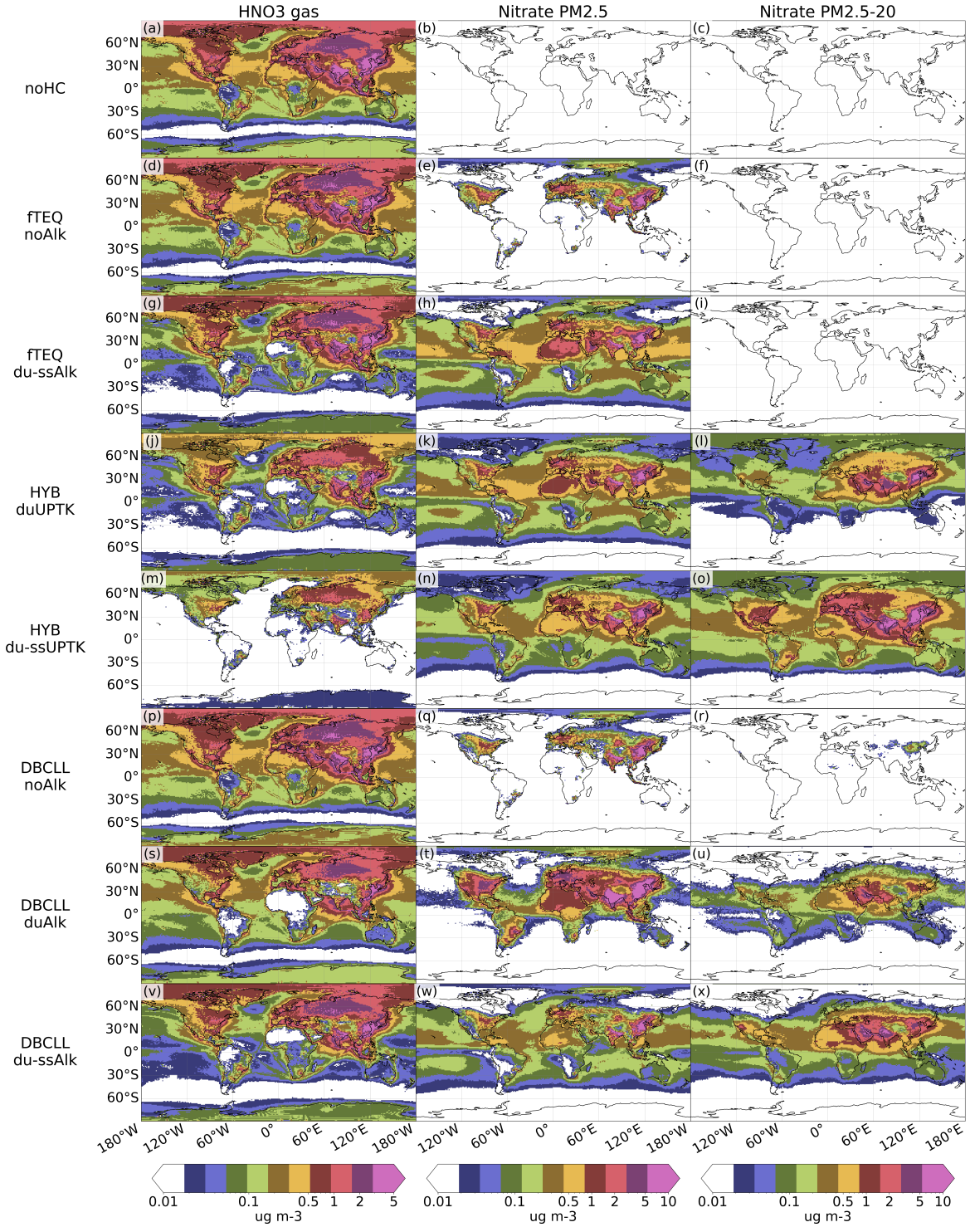

Figure 3. Surface ~~concentration~~ concentrations ($\mu g\ m^{-3}$) of $HNO_{3(g)}$, fine and coarse NO_3^- simulated by the different mechanisms, averaged for 2018.

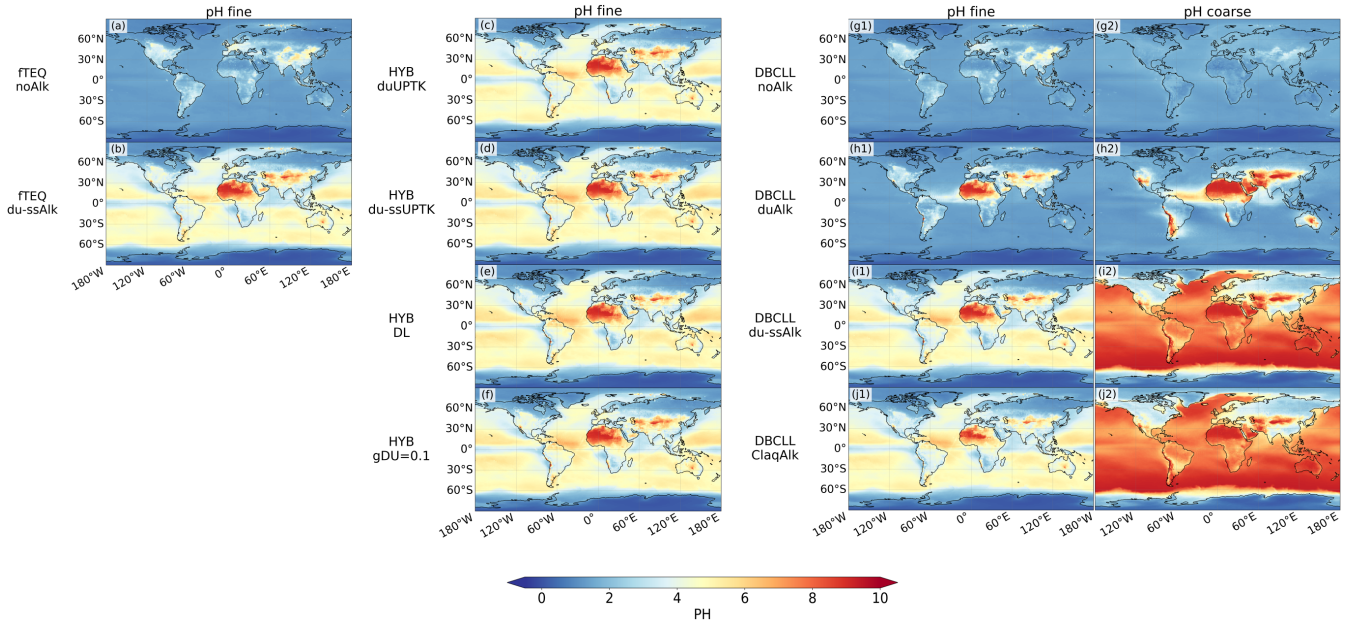

Figure 4. Surface ~~average~~ pH of the studied mechanisms for fine and coarse aerosol size modes, averaged for ~~the year~~ 2018.

~~mechanisms are reduced from~~ regions exhibit similar seasonal patterns. From April to October~~(summer and fall in northern hemisphere), with the exception of~~ , differences among mechanisms diminish, except for the HYB_du-ssUPTK~~that shows artefacts, significantly overestimating~~ , which significantly overestimates $PM_{2.5}NO_3$ during these months. Notably, the runs considering the effect of dust and SS alkalinity in the partitioning process reduce the negative bias of $PM_{2.5}NO_3$ significantly, especially during February. ~~Increased~~

Greater variability among experiments ~~is found in the evaluation of~~ emerges when evaluating $HNO_{3(g)}$ and Total NO_3^- ~~(~~, with more observational data available over North-Central America ~~compared to Europe and Asia)~~than Europe or Asia. This variability is highly influenced by ~~the pathway used for~~ how each mechanism models coarse NO_3^- formation~~in each mechanism. Specifically, larger variability is noted over Asia compared to Europe and North-Central America (Figure~~ , especially over Asia (Fig. S12 ~~).~~

~~From the various mechanisms analysed, the representation of coarse~~ in the Supplement). For example, the HYB runs, which rely on irreversible uptake reactions, consistently overestimate total NO_3^- ~~formation through an irreversible uptake reaction (HYB runs) consistently yield overestimated surface concentrations of Total in all the regionsanalyzed. Better agreement is found under the assumption of reversible partitioning(DBCLL)~~across all regions. In contrast, the DBCLL runs, which assume reversible partitioning, better align with observations.

~~Considering only the irreversible UPTK of over dust while neglecting its UPTK over SS (~~From the HYB simulations, the HYB_duUPTK ~~sensitivity run) shows very good~~ run demonstrates strong correlation coefficients for both fine and total NO_3^- concentrations (0.8 and 0.9, respectively). ~~Notably, the seasonal variability~~ The seasonal variability in this run closely resem-

bles that of ~~experiments that completely neglect coarse formation (~~the fTEQ_noAlk and fTEQ_du-ssAlk ~~). This indicates the important~~ experiments, which fully neglect coarse NO_3^- formation. This similarity suggests a limited amount of sites affected significantly by coarse NO_3^- formation, while highlighting the relevant role of the TEQ calculation in the fine mode~~, likely due to the limited amount of sites affected significantly by nitrate coarse formation. However,~~ . Despite showing a systematic positive bias ~~results under the UPTK assumption with values (~~of 0.03/0.04/0.29 $\mu g\ m^{-3}$ for $HNO_{3(g)}$, fine NO_3^-, and Total NO_3^-, respectively~~. The correlation for is much lower (0.23), but still within the upper range compared to all sensitivity runs. Results from ~~), HYB_duUPTK ~~show~~ maintains consistency across continents~~, with notable overestimation of~~ . However, it notably overestimates Total NO_3^- over Asia in November and over Europe from May to September, likely ~~influenced by~~ due to dust events affecting the monitoring sites.

~~By extending~~ Including the UPTK reactions ~~to include SS (sensitivity run~~ on SS in the HYB_du-ssUPTK ~~), the previously identified overestimation is exacerbated due to a~~ run exacerbates this overestimation ~~excessive condensation of~~ due to excessive $HNO_{3(g)}$ condensation into coarse NO_3^- ~~compared to observations~~. Specifically, the correlation for Total NO_3^- ~~decreases significantly~~ drops from 0.9 to 0.66~~. Under HYB_du-ssUPTK~~, $HNO_{3(g)}$ concentrations are underestimated ~~with a (~~bias of -0.10 $\mu g\ m^{-3}$~~, while~~), and Total NO_3^- surface concentrations are overestimated by 1.50 $\mu g\ m^{-3}$~~, which represents the largest bias among~~ —the highest bias among all sensitivity runs (~~as shown in~~ Table 4). This ~~positive bias in is mainly observed~~ overestimation is most pronounced over Asia (3-5 $\mu g\ m^{-3}$ vs. 1 $\mu g\ m^{-3}$) and North-Central America (1.5-2.5 $\mu g\ m^{-3}$ vs. 1.0 $\mu g\ m^{-3}$)~~, while differences~~ . Discrepancies in European sites are more pronounced during ~~the northern hemisphere~~ summer and fall (~~Figure~~ Fig. S12 ~~). Additionally, modifying the value of $\gamma(HNO_3)$ for dust and keeping it constant (run~~ in the Supplement).

To evaluate whether this overestimation results from unlimited $HNO_{3(g)}$, we examined the HYB_g0p1 and HYB_DL configurations (Supplementary Section S5). Increasing the uptake coefficient $\gamma(HNO_3)$ in HYB_g0p1 ~~)~~ further enhances the overestimation of total NO_3^- by an additional 30%~~.~~

, suggesting that $HNO_{3(g)}$ availability is not the limiting factor. ~~To evaluate whether the excessive overestimation is due to unlimited gas availability for condensation in each size mode, we evaluate the results obtained from the~~ Similarly, HYB_DL ~~configuration. Surface concentrations in HYB_DL show minimal change compared to HYB_du-ssUPTK, with the bias in~~ shows only a marginal reduction in total NO_3^- ~~decreasing marginally~~ bias (from 1.5 to 1.3 $\mu g\ m^{-3}$~~(see Table S7 and Figure S14). Overall, the adoption of large values for $\gamma(HNO_3)$ for SS particlesin this study may explain the overly efficient nitrate formation found in HYB_du-ssUPTK, which suggests the necessity for further refinement of~~), reinforcing that the overestimation stems from the overly high $\gamma(HNO_3)$ values for SS particles, as previously discussed in Section 3.1.2. This highlights the need for refining HYB schemes.

~~The systematic overestimation of in HYB schemes is markedly reduced when adopting a reversible partitioning of the semi-volatile inorganic species in the full range of particle sizes (DBCLL scheme). Specifically, the bias in~~ Conversely, DBCLL mechanisms markedly reduce surface concentration biases. Without alkalinity, the total NO_3^- ~~surface concentrations is shifted~~ bias shifts from 0.29 to -0.43 $\mu g\ m^{-3}$ between the HYB and DBCLL runs~~neglecting alkalinity, and remarkably reduced~~ . Incorporating dust and SS NVC further improves the bias, reducing it from 1.5 to -0.1 $\mu g\ m^{-3}$ between ~~HYB and DBCLL~~

runs incorporating dust and SS NVC the HYB_du-ssUPTK and DBCLL_du-ssAlk runs (Table 4), while maintaining a high correlation of around . All consistently achieve high correlation coefficients (aprox. 0.8).

If dust and SS NVC are excluded in the TEQ reactions in a DBCLLmechanism (DBCLLHowever, the DBCLL_noAlk run), tends to underestimate total NO_3^- (bias of -0.43$\mu g\ m^{-3}$) and overestimates $HNO_{3(g)}$ is generally overestimated with a bias of (bias of +0.13 $\mu g\ m^{-3}$and), failing to capture its seasonal cycle is poorly captured, with very low (correlations of 0.06). Surprisingly, fTEQ runs show better results despite completely the fTEQ runs outperform DBCLL_noAlk despite neglecting coarse NO_3^- formation. The positive biases in are particularly dominated by a consistent overprediction throughout the year over Asia and during specific periods over Europe and Central-North America. Excessive levels of are accompanied with a slight underprediction in total , with a bias of -0.43$\mu g\ m^{-3}$. Including solely dust alkalinity in the DBCLL mechanism by implementing reactions R6-11 from Table 1 (DBCLL_duAlk), results in opposite results: is underestimated with respect to observations from March to September by -0.1$\mu g\ m^{-3}$, while both fine and total particulate are overestimated with respect to observations by 1.5 and 2 $\mu g\ m^{-3}$ respectively (see Figure S14).

These biases for and particulate are improved when the effect of SS alkalinity is additionally considered in the formation of (R6-12 from Table 1; Including dust and SS alkalinity in DBCLL_du-ssAlk simulation). The presence of dust and SS NVC increases the condensation rates substantially improves these biases. Enhanced condensation of $HNO_{3(g)}$ towards into both fine and coarse particulate NO_3^- (Figure 5) , driving the results closer to observations. Namely, the DBCLL_du-ssAlk simulation reports a lower Fig. 5) yields a reduced bias in total NO_3^- of (-0.10 $\mu g\ m^{-3}$,while maintaining a good seasonal cycle) and a strong seasonal agreement, with correlation coefficients of 0.82 and 0.78 for fine and Total total NO_3^-, respectively. This These results also outperform the DBCLL_duAlk run, which excludes SS alkalinity (Supplementary Section S5 and Table S7).

The evaluation of the DBCLL experiments highlights the paramount importance of including accounting for NO_3^- formation on both dust and SS to accurately represent $HNO_{3(g)}$ and particulate NO_3^- concentrations.

The sensitivity to the treatment of dust NVCs in the model can be of model performance to the dust NVC representation is further assessed using the DBCLL_Claq run, where the Claquin et al. (1999) dataset is adopted which applies an average dust alkalinity based on Claquin et al. (1999) instead of Journet et al. (2014) (see Sect. 2.2.3). The evaluation revels Results show limited differences compared to DBCLL_du-ssAlk, although both with correlation and bias are slightly improved for total NO_3^- just slightly improved in DBCLL_Claq with 0.81 and -0.09 $\mu g\ m^{-3}$, respectively (Supplementary Section S5 and Table S7). Given Timeseries from Fig. S14, compared to Fig. 5, also shows comparably similar results when using DBCLL with Claquin et al. (1999) or Journet et al. (2014) mineral datasets. Overall, based on the limited number of observation sites used in our evaluation, the impact of dust NVC representation appears on surface NO_3^- concentrations does not appear to be significant . in the observational points.

3.2.2 Ammonia and particulate ammonium

Results for $NH_{3(g)}$ and particulate NH_4^+ are generally more consistent across all mechanisms compared to NO_3^- resultsoutcomes. This consistency is expectedsince in , as all sensitivity runs use the same condensation pathway for the conversion of $NH_{3(g)}$ to fine NH_4^+ (through reactions R6 and R7 in (Table 1). The seasonal cycle is reasonably well captured for All mechanisms

effectively capture the seasonal cycle of both $NH_{3(g)}$ ~~(with correlations~~ and fine NH_4^+. Correlation coefficients for $NH_{3(g)}$ range from 0.85 to 0.88~~) and~~ , while those for fine NH_4^+ ~~(with correlations~~ range from 0.59 to 0.77~~), although the results~~ . However, model performance is slightly weaker for total NH_4^+ ~~are slightly worse (correlations from~~ , with correlations between 0.41 ~~to~~ and 0.54~~)~~.

The DBCLL_du-ssAlk and DBCLL_Claq runs ~~present~~ yields the lowest errors for NH_4^+~~, with RMSEs of~~ . RMSEs are 0.17 ~~/~~$\mu g\ m^{-3}$ for fine and 0.12 $\mu g\ m^{-3}$ ~~and~~ for total concentrations, with corresponding biases of -0.02 ~~/~~$\mu g\ m^{-3}$ and 0.08 $\mu g\ m^{-3}$ ~~for fine and total concentrations, respectively. The sensitivity~~ (Tables 4 and S7). These results highlight the significant sensitivity of NH_4^+ predictions to the treatment of dust and SS ~~NVC is again found to be very significant~~non-volatile cations (NVCs). Including or ~~neglecting NVC representation exacerbates the biases found in the~~ omitting NVC representation notably affects the biases across different schemes. Unlike NO_3^-, ~~the increase in particle alkalinity limits~~ increased particle alkalinity reduces the condensation of $NH_{3(g)}$, thereby ~~reducing the formation of~~ limiting NH_4^+ ~~, which~~ formation. This effect helps mitigate biases ~~compared to observations~~when compared to observational data.

Overall, ~~the biases for~~ biases for both fine and total NH_4^+ remain ~~reasonably~~ relatively low in most experiments, ranging from -0.02 to 0.29 $\mu g\ m^{-3}$.

3.2.3 Sulfur species

~~The results~~ Results for $SO_{2(g)}$ ~~gas~~ and particulate SO_4^{2-} are consistent across all sensitivity simulations~~, as they are~~ . This consistency is expected since sulfate formation is independent of the pathways ~~implemented~~ used for coarse NO_3^- formation~~, with all of them forming~~ . In all cases, particulate SO_4^{2-} is produced from $SO_{2(g)}$ and $H_2SO_{4(g)}$ in a similar manner (see Section 2.3). Differences solely arise from variations in the treatment of the $\gamma(SO_2)$ coefficient when ~~considering alkalinity of dust~~ accounting for dust alkalinity, which introduces slight differences in SO_4^{2-} formation. Overall, the model slightly underestimates both $SO_{2(g)}$ and ~~Total~~ total SO_4^{2-}, particularly at European ~~stations, while it marginally overestimates~~ monitoring sites. In contrasts, fine SO_4^{2-} ~~, driven by~~ is marginally overestimated, mainly driven by observations from Central-North American sites. Temporal ~~correlations vary~~ correlation coefficients average around 0.6, ~~being slightly lower for Total~~ with slightly lower values for total SO_4^{2-}. For $SO_{2(g)}$, the ~~small misalignment with observations~~ slight mismatch with observational data primarily stems from the European evaluation, which presents a consistent negative bias of -0.5 $\mu g\ m^{-3}$ throughout the studied period (~~Figure~~ Fig. S12 in the Supplement). Fine and total SO_4^{2-} ~~results also show acceptable~~ concentrations also show generally good agreement with observations~~, with only a slight excess~~ . However, there is a modest overestimation in fine SO_4^{2-} concentrations~~(~~, with an average bias of 0.30 ~~$\mu g\ m^{-3}$ average bias)~~$\mu g\ m^{-3}$, particularly over Central and North America~~, and an underestimation of~~ . Conversely, total particulate SO_4^{2-} surface concentrations ~~(~~are underestimated over Europe, with an average bias of -0.43 ~~average bias) over Europe~~(Table 4 and ~~Figure~~ Fig. S12 ~~).~~ in the Supplement). The negative bias in SO_4^{2-} ~~may be linked~~ concentrations may be attributed to the sulfate formation scheme and sulfur ~~emissions~~ emission inventories employed in our runs. ~~Further investigation regarding the employed~~ Reevaluating the $SO_{2(g)}$ uptake coefficient could ~~be beneficial. Some alternatives to the~~ provide valuable insights. The current implementation uses the uptake coefficient function from Fairlie et al. (2010)~~have been proposed~~ . Alternative formulations have been suggested in the literature, ~~though~~

~~they lack a dependence with RH. Possible alternatives include~~ such as the uptake coefficient values proposed by Phadnis and Carmichael (2000) for $SO_{2(g)}$ uptake on dust, and by Song and Carmichael (2001) for uptake on SS, as reported in Li et al. (2012). Exploring these alternatives may help improve the model's representation of sulfur species.

3.2.4 Fine and total particulate matter

~~Regarding~~ Results for $PM_{2.5}$ and PM_{10} ~~, results~~ are consistent across the different sensitivity runs (~~Figure~~ Fig. 5), indicating that the total mass is ~~dominated by other aerosol~~ more influenced by components other than secondary inorganic species. ~~In all cases, the global seasonal cycles~~

Globally, the seasonal cycles of $PM_{2.5}$ are well reproduced ~~with similar correlation coefficients~~ across all sensitivity runs, with correlation coefficients consistently around 0.75. However, annual $PM_{2.5}$ concentrations are overestimated by an average of 20 $\mu g\ m^{-3}$ ~~on average~~ (Table 4). ~~Note that the comparison is clearly driven by the dominant presence of stations over Asia, where high concentrations are present. Conversely, results over Europe and North and Central America show a slight underestimation of~~ In contrast, PM_{10} concentrations over Asia show good agreement with observations, indicating that the model underestimates coarse particulate matter (PM), especially at monitoring sites in mainland China (Supplementary Figures S12 and S13). It is important to note that regions with significant $PM_{2.5}$ ~~concentrations.~~ overestimation do not overlap with the limited sites where chemical composition measurements are available—locations where the model accurately represents total particulate NO_3^- and NH_4^+ (Supplementary Fig. S12). Our results suggest that the absence of anthropogenic coarse dust emissions in the CAMS emission inventory may hinder the formation of coarse inorganic species, including NO_3^-. The formation of coarse NO_3^- is critical for scavenging $HNO_{3(g)}$ and suppressing the formation of fine particulate NO_3^-, by providing surfaces for heterogeneous reactions. The significant influence of typically neglected anthropogenic coarse PM emissions on nitrate formation has been emphasized in previous studies (e.g. Zhai et al. (2023)), highlighting the need for improved emission inventories to better capture the interactions between coarse particles and nitrogen species.

~~A similar pattern is found for~~ In contrast, $PM_{2.5}$ model results over Europe and North and Central America are well aligned with observations (Fig. S12). The evaluation of PM_{10} ~~, though North and Central America surface concentrations are underestimated, specially from April to September, which does not seem to be a caused by the underestimation of any secondary inorganic aerosol speciesstudied in this work. Consequently,~~ shows just slightly worsened RMSE (ranging from 22.49 to 30.42 $\mu g\ m^{-3}$) and correlation coefficients (from 0.36 to 0.46) ~~are slightly worsened~~ compared to $PM_{2.5}$ (RMSE from 24.74 to 26.16 $\mu g\ m^{-3}$ and correlations from 0.74 to 0.76, Table 4). ~~Consistent results have been reported by Jones et al. (2021) over Europe. We estimate that the~~ This is attributed to the PM_{10} ~~fraction of secondary inorganic aerosols condensing on dust and SS accounts for up to 25% of the total mass. This estimation is derived from noHC run, which excludes heterogeneous chemistry effects on nitrates and ammonia but includes secondary particles typical of other methodologies.~~ surface concentrations underestimation over North and Central America, specially from April to September, which does not seem to be caused by the underestimation of any secondary inorganic aerosol species studied in this work. Over Europe, our results are in agreement with those reported by Jones et al. (2021).

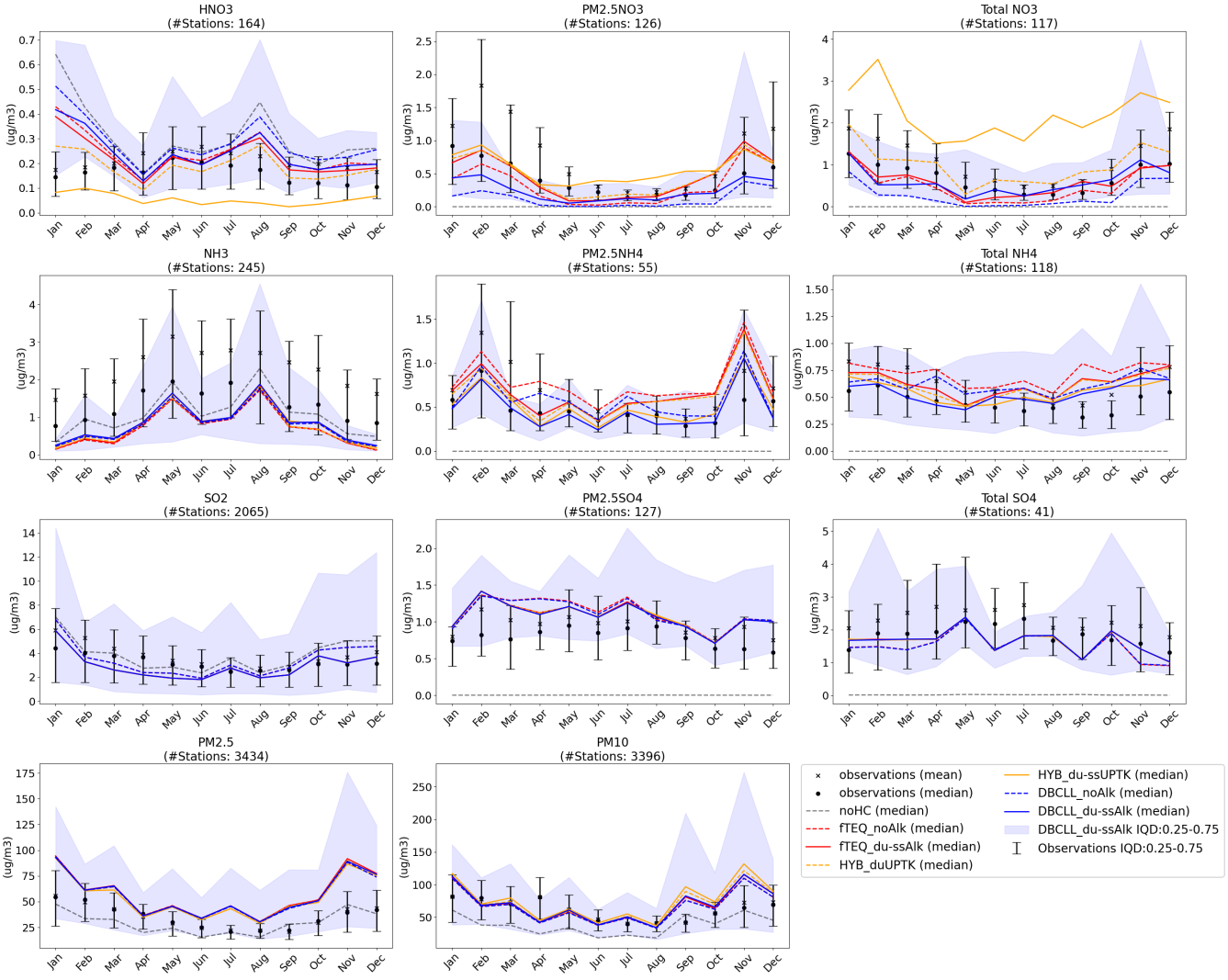

Figure 5. Observational evaluation of gas and particulate species surface concentrations. Black solid dots and crosses represent observations' monthly median and mean~~of observations~~, respectively. Colored lines represent each configuration's monthly median ~~surface concentrations~~ over the observational points. Error bars are the observational interquantile 0.25 to 0.75 distance. Blue shading is the interquantile 0.25 - 0.75 distance for the DBCLL_du-ssAlk simulation. For the Total NO_3^- modes, the available data from Europe, Asia and North-Central America stations have been averaged together, despite data from Asia and North-Central America ~~referring~~ refer to total particle concentration, while data from Europe is limited strictly to ~~below~~ particles with diameter up to 10 μm~~particle diameter~~.

Table 4: Correlation coefficients, bias ($\mu g\ m^{-3}$) and root mean square error (rmse, $\mu g\ m^{-3}$) of each configuration's median with respect to the median of observations, corresponding to the timeseries shown in Fig. 5.

	HNO_3			$PM_{2.5}NO_3$			Total NO_3		
	corr	**bias**	**rmse**	**corr**	**bias**	**rmse**	**corr**	**bias**	**rmse**
noHC	**0.03**	**0.15**	**0.20**	**0.00**	**-0.43**	**0.49**	**0.00**	**-0.70**	**0.77**
fTEQ_noAlk	**0.15**	**0.08**	**0.12**	**0.70**	**-0.10**	**0.23**	**0.91**	**-0.19**	**0.25**
fTEQ_du-ssAlk	**0.23**	**0.07**	**0.10**	**0.76**	**0.02**	**0.20**	**0.88**	**-0.09**	**0.19**
HYB_duUPTK	**0.23**	**0.03**	**0.06**	**0.80**	**0.04**	**0.18**	**0.90**	**0.29**	**0.36**
HYB_du-ssUPTK	**0.06**	**-0.10**	**0.11**	**0.77**	**0.14**	**0.21**	**0.66**	**1.50**	**1.56**
DBCLL_noAlk	**0.06**	**0.13**	**0.16**	**0.68**	**-0.31**	**0.36**	**0.86**	**-0.43**	**0.46**
DBCLL_du-ssAlk	**0.16**	**0.08**	**0.12**	**0.82**	**-0.18**	**0.24**	**0.78**	**-0.10**	**0.23**

	NH_3			$PM_{2.5}NH_4$			Total NH_4		
	corr	**bias**	**rmse**	**corr**	**bias**	**rmse**	**corr**	**bias**	**rmse**
noHC	**0.80**	**-0.29**	**0.44**	**0.00**	**-0.48**	**0.51**	**0.00**	**-0.45**	**0.46**
fTEQ_noAlk	**0.88**	**-0.65**	**0.69**	**0.64**	**0.29**	**0.35**	**0.41**	**0.26**	**0.28**
fTEQ_du-ssAlk	**0.87**	**-0.62**	**0.67**	**0.59**	**0.18**	**0.28**	**0.51**	**0.17**	**0.20**
HYB_duUPTK	**0.87**	**-0.61**	**0.66**	**0.56**	**0.16**	**0.27**	**0.48**	**0.15**	**0.18**
HYB_du-ssUPTK	**0.86**	**-0.55**	**0.60**	**0.70**	**0.03**	**0.16**	**0.54**	**0.10**	**0.13**
DBCLL_noAlk	**0.86**	**-0.58**	**0.62**	**0.66**	**0.10**	**0.20**	**0.51**	**0.16**	**0.18**
DBCLL_du-ssAlk	**0.85**	**-0.53**	**0.59**	**0.70**	**-0.02**	**0.17**	**0.47**	**0.08**	**0.12**

	SO_2			$PM_{2.5}SO_4$			Total SO_4		
	corr	**bias**	**rmse**	**corr**	**bias**	**rmse**	**corr**	**bias**	**rmse**
noHC	**0.61**	**0.65**	**1.24**	**0.59**	**-0.79**	**0.80**	**0.62**	**-1.91**	**1.93**
fTEQ_noAlk	**0.59**	**0.23**	**1.12**	**0.61**	**0.33**	**0.36**	**0.51**	**-0.47**	**0.58**
fTEQ_du-ssAlk	**0.63**	**-0.30**	**0.91**	**0.57**	**0.30**	**0.33**	**0.60**	**-0.38**	**0.49**
HYB_duUPTK	**0.63**	**-0.29**	**0.91**	**0.57**	**0.29**	**0.33**	**0.59**	**-0.38**	**0.50**
HYB_du-ssUPTK	**0.63**	**-0.29**	**0.91**	**0.57**	**0.29**	**0.33**	**0.60**	**-0.38**	**0.49**
DBCLL_noAlk	**0.59**	**0.23**	**1.12**	**0.58**	**0.32**	**0.36**	**0.49**	**-0.47**	**0.59**
DBCLL_du-ssAlk	**0.63**	**-0.29**	**0.91**	**0.56**	**0.29**	**0.32**	**0.69**	**-0.52**	**0.67**

Table 4 continued from previous page

	$PM_{2.5}$			PM_{10}		
	corr	**bias**	**rmse**	**corr**	**bias**	**rmse**
noHC	**0.75**	**-5.62**	**9.55**	**0.40**	**-23.16**	**28.42**
fTEQ_noAlk	**0.76**	**20.91**	**24.98**	**0.46**	**5.14**	**22.49**
fTEQ_du-ssAlk	**0.74**	**21.75**	**26.16**	**0.44**	**7.16**	**24.38**
HYB_duUPTK	**0.74**	**21.05**	**25.32**	**0.40**	**10.16**	**27.41**
HYB_du-ssUPTK	**0.76**	**19.59**	**23.91**	**0.36**	**13.92**	**30.45**
DBCLL_noAlk	**0.76**	**20.59**	**24.74**	**0.46**	**4.98**	**22.50**
DBCLL_du-ssAlk	**0.75**	**21.02**	**25.22**	**0.43**	**8.09**	**24.80**

3.3 Nitrogen partitioning

In this section, we explore the ~~influence~~ impact of coarse particulate NO_3^- formation on the overall partitioning of atmospheric nitrogen ~~into~~ between the gas and particle phases ~~, as well as its distribution between~~ (Section 3.3.1). Additionally, we analyze how this formation influences the distribution of nitrogen between its oxidized and reduced forms (Section 3.3.2). The observational evaluation of surface concentrations for total reduced and oxidized nitrogen is presented in Supplementary Section S6.

3.3.1 Partitioning between gas and particle phases

~~Simulated nitrogen compounds in the~~ The partitioning of atmospheric nitrogen species in gas and aerosol phases ~~in the atmosphere vary depending on the underlying chemistry~~ varies according to the underlying chemical assumptions. We analyze the average atmospheric burden and ~~the accumulated deposition of all nitrogen species considered~~ deposition of nitrogen species in the MONARCH model across ~~different sensitivity runs , as shown in Figure~~ sensitivity runs (Fig. 6 and Table S13 in the Supplement). The simulation labeled as noHC, ~~which excludes~~ excluding heterogeneous chemistry involving nitrate, serves as the baseline for understanding the distribution of nitrogen species in the gas phase. Under this ~~assumption, the predominant nitrogen species in the atmosphere include~~ configuration, the dominant nitrogen species are $HNO_{3(g)}$, peroxyacetly nitrate (PAN), $NH_{3(g)}$, and NO_x, with burdens of 1.06, 0.8, 0.71, and 0.38 TgN, respectively. ~~and are characterized by~~ The longer atmospheric lifetimes ~~compared to due to~~ of $HNO_{3(g)}$ and PAN result from their chemical stability ~~and lower reactivity. While other speciesshave a minor presence in the atmosphere~~compared to more reactive NO_x species. Notably, $N_2O_{5(g)}$ ~~is particularly relevant because it enhances the production of~~ plays a key role in nighttime $HNO_{3(g)}$ ~~during nighttime through~~ production via heterogeneous hydrolysis (Riemer et al., 2003). ~~Overall, the total nitrogen burden in the atmosphere~~

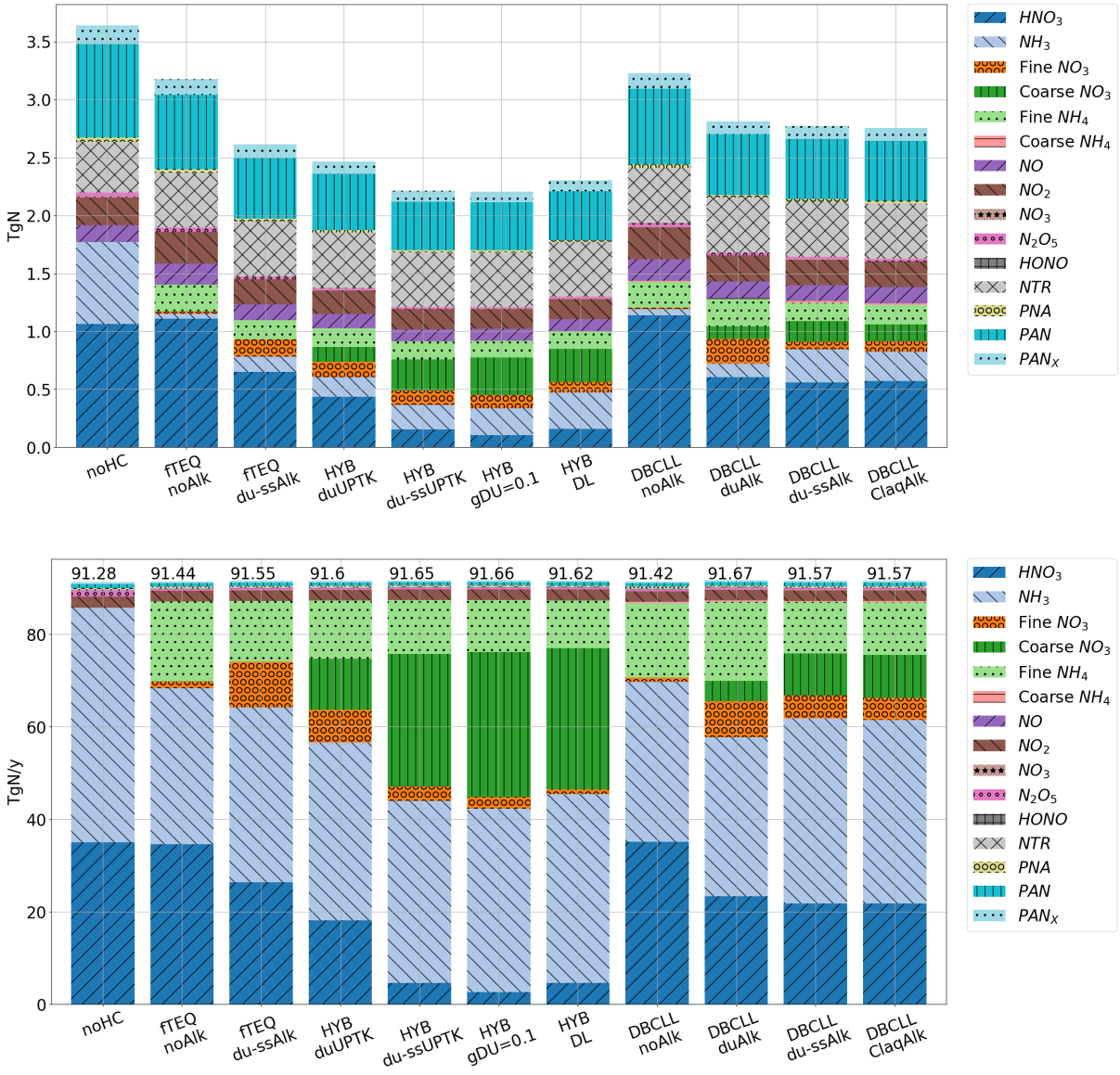

Figure 6. ~~Nitrogen atmospheric 2018~~ Atmospheric nitrogen average burdens (top) and accumulated depositions (bottom) ~~of the nitrogen-containing species simulated~~ in ~~MONARCH~~ Tg of nitrogen (TgN) for the different dust heterogeneous chemistry mechanisms. The corresponding fractions of the nitrogen-containing species simulated in MONARCH is shown in each bar plot. Total nitrogen deposition is reported on the top of each bar of the depositions plot.

Total nitrogen burden is highly sensitive to the ~~adopted nitrate mechanism, resulting in lower burdens in the schemes that are more efficient in producing~~ nitrate formation mechanism. Schemes promoting efficient coarse-mode NO_3^- ~~in the aerosol phase, particularly in the coarse mode~~formation significantly reduce nitrogen burdens.

~~Assuming~~ For example, assuming irreversible condensation of $HNO_{3(g)}$ ~~in coarse particles results in a reduction of the nitrogen load of~~ onto coarse particles reduces nitrogen load by 32% and 40% ~~compared to the baseline noHC if only dust~~ when considering dust only (HYB_duUPTK) ~~or~~ and both dust and SS (HYB_du-ssUPTK)~~are considered~~, respectively. In ~~particular, in the~~ HYB_duUPTK~~simulation, a significant portion of partitions into the particle phase, accounting for~~ , 0.13 TgN ~~of partitions into~~ fine and coarse NO_3^- on dust. ~~This amount increases significantly when SS is included, with an additional~~ Including SS (HYB_du-ssUPTK) further increases consumption of $HNO_{3(g)}$ ~~. Thus, the size distribution of particulate~~ and coarse NO_3^- ~~shifts towards the coarse mode (~~formation leading to a total NO_3^- burden 0.27 TgN~~), while~~ , while the fine NO_3^- ~~remains almost unaffected (~~burden remains unchanged at 0.12 TgN ~~) compared to HYB_duAlk (~~(Supplementary Table S13).

~~To elucidate the impact of UPTK by dust and SS particles, we compare the nitrogen burdens from HYB_duUPTK and HYB_du-ssUPTK runs against those from~~ Comparing HYB runs to fTEQ_du-ssAlk ~~: results remark the role of~~ reveals that dust and SS ~~in decreasing~~ uptake reduces $HNO_{3(g)}$ ~~gas phase~~ burdens by 0.21 TgN ~~on dust~~(dust) and 0.50 TgN ~~on dust and SS, compared to its sole condensation in the fine mode through TEQ, therefore driven by the irreversible UPTK of~~ (dust + SS) relative to TEQ-only partitioning. This is driven by irreversible uptake in the coarse mode. ~~In this context, budget analysis reveals that UPTK on SS significantly alters the deposition rates~~ Consequently, the deposition rate of NO_3^- ~~, increasing total deposition~~ increases from 80 to 140 Tg/y~~and reducing~~ , and its atmospheric lifetime decreases from 2.6 to 2.3 days (Table 5). The combined UPTK on dust and SS nearly depletes $HNO_{3(g)}$, leaving only 0.15 TgN~~remaining, which results in an~~ , which contributes to the overestimation of surface NO_3^- ~~as discussed in Sections 3.2~~(Sections 3.1 and 3.2). ~~In addition, the irreversible condensation of on dust and SS particles also affects other gas-phase spices. Specifically~~

Irreversible condensation also reduces $NO_{(g)}$, $NO_{2(g)}$, and $N_2O_{5(g)}$ burdens ~~decrease~~ to 0.11, 0.17, and 0.01 TgN, respectively, due to enhanced $N_2O_{5(g)}$ hydrolysis on increased particle surfaces. This reduction ~~in~~ can be attributed to increased NO_3^- particle formation, ~~which enhances the total particle concentration and , consequently, the~~ and consequently, available surface where hydrolysis of $N_2O_{5(g)}$ can take place. Ultimately, ~~it~~ this produces more $HNO_{3(g)}$ available for partitioning into the particle phase. ~~Among the mechanisms analyzed, HYB_g0p1 shows the most efficient depletion of , achieved by using a constant value of $\gamma = 0.1$ instead of the RH-dependent dust uptake coefficient from Fairlie et al. (2010). In this scenario, is further reduced to 0.46 TgN, accompanied by an increase in coarse formation up to 1.93 Tg. Furthermore, the deposition rates rise from 140 to 149 Tg/y, as shown in Table 5.~~

Conversely, nitrogen loads increase when reversible condensation of $HNO_{3(g)}$ and $NH_{3(g)}$ is considered in the fTEQ and DBCLL sensitivity simulations. A larger proportion of nitrogen remains in the gas phase compared to HYB schemes. Notably, ~~load slightly increases relative to the noHC baseline (from 1.11 to 1.14 Tg N) when~~ neglecting dust and SS alkalinity ~~is neglected in the partitioning~~ (fTEQ_noAlk~~and~~ , DBCLL_noAlk~~runs) . Furthermore,~~) slightly increases $HNO_{3(g)}$ burdens (from 1.11 to 1.14 TgN) and elevates $NO_{(g)}$ and $NO_{2(g)}$ ~~increase~~ by 0.29% and 0.12%~~respectively, and PAN decreases by nearly 25%~~, respectively. ~~Conversely, accounting for the alkalinity in the reversible partitioning~~ When dust and SS alkalinity

are considered (fTEQ_du-ssAlk, DBCLL_duAlk~~and~~ , DBCLL_du-ssAlk)~~generally results in higher condensation rates of~~ , $HNO_{3(g)}$ ~~(reducing its loads~~ burdens decrease by 40~~% and~~ –50%~~compared to noHC) to form~~ , enhancing particulate NO_3^- formation. This shift towards the aerosol phase ~~is an expected consequence of~~ results from the neutralization of NVC from dust and SS by $HNO_{3(g)}$. ~~Additionally~~In these cases, $NO_{(g)}$, $NO_{2(g)}$ and $N_2O_{5(g)}$ budgets decrease by approximately 20% compared to analogous mechanisms without alkalinity, driven by the more efficient $N_2O_{5(g)}$ aqueous dissociation due to the increased particle presence. SS alkalinity alters the partitioning of aerosol NO_3^- from fine (-72%) towards coarse mode (+63%) when comparing DBCLL_duAlk and DBCLL_du-ssAlk, resulting in 0.06 (fine) and 0.18 TgN ~~of , respectively (see DBCLL_du-ssAlk run in Figure~~ (coarse) burdens (Fig. 6). This surge in coarse NO_3^- formation with dust and SS alkalinity causes a 26% decrease ~~of~~ in total NO_3^- ~~burdens, corresponding to~~ burden and a 14% increase ~~in~~ deposition rates compared to the DBCLL_duAlk case, mainly driven by enhanced wet deposition of coarse NO_3^- from 11.0 to 27.5 Tg/y (Table 5). This can be attributed to the higher deposition efficiency of SS particles due their larger size ranges and abundance near the surface. Consequently, the presence of SS decreases the atmospheric lifetime of particulate NO_3^- from 4.9 to 3.1 days~~(Table 5)~~, contrasting with scenarios that consider only dust alkalinity~~in coarse formation~~. ~~Finally,~~

Additionally, SS NVCs (e.g., Na^+) inhibit $NH_{3(g)}$ ~~and partitioning are also very sensitive to the inclusion of SS NVC, leading to a partial inhibition of~~ condensation into NH_4^+~~(~~, reducing NH_4^+ burdens from 0.31 to 0.22 Tg ~~,~~(Table S11). ~~This effect is likely due to SS contributing additional basic NVC that hinders the formation of particulate .~~

3.3.2 Reduced and oxidized nitrogen

~~The~~

Figure 7 presents the annual averages burdens and depositions of oxidized ($HNO_{3(g)}$ + NO_3^-) and reduced ($NH_{3(g)}$ + NH_4^+) nitrogen for each sensitivity run. These results are compared with global estimates from the AeroCom phase III nitrate experiment (Bian et al., 2017)~~provides~~ , which offers a comprehensive range of budgets derived from different global aerosol models employing mechanisms similar to those analyzed in our study. ~~Here, we compare the partitioning sensitivities in terms of oxidized and reduced nitrogen with the global estimates reported in AeroCom. In particular, the results of~~ As additional references, the results from the EMAC model ~~from the nitrate phase III AeroCom experiment are reported separately~~ (Karydis et al., 2016) and the LMDz-INCA model (Hauglustaine et al., 2014) are shown separately from the average of AeroCom in Fig. 7 due to their similarity ~~to the DBCLL mechanism adopted in our analysis. Additionally, the study by Hauglustaine et al. (2014) , which utilizes the LMDz-INCA model with an irreversible uptake mechanism, provides a reference for the HYB runs. Figure 7 presents the annual averages of oxidized and reduced nitrogen burdens and deposition for each sensitivity run.~~ with the DBCLL and HYB mechanisms, respectively.

The HYB mechanisms yield ~~a total~~ an annual average burden of oxidized ~~species (~~nitrogen of 0.55 TgN~~) that is~~ , slightly below the ~~mean of AeroCom results but align well~~ AeroCom multi-model mean but in close agreement with Hauglustaine et al. (2014). ~~Oxidized nitrogen budgets in these mechanisms fall within the lower range compared to the~~ Compared to the fTEQ and DBCLL mechanisms that account for ~~alkalinity~~ dust and sea salt (SS) alkalinity, which show higher oxidized nitrogen burdens (0.6~~TgN vs. average~~ –0.8 TgN~~in fTEQ and DBCLL). This may be attributed to an~~), the HYB mechanisms fall on the lower end

of the distribution. This reduction is primarily due to the efficient deposition of ~~nitrogen in the form of~~ particulate NO_3^- and the limited ~~amount~~ atmospheric presence of $HNO_{3(g)}$ ~~left in the atmosphere under the irreversibility assumption already noted in previous~~ under the assumption of irreversible uptake, as discussed in Sections 3.2 and 3.3.1. ~~Regarding reduced nitrogen , the budgets from the HYB mechanisms (approx.~~

For reduced nitrogen species, the HYB mechanisms produce an average burden of approximately 0.3 TgN~~) align well with both~~ , aligning well with the AeroCom mean~~and Hauglustaine et al. (2014), although they present a relatively lower fraction of~~ . However, HYB configurations yield lower particulate NH_4^+ ~~. The~~ burdens (0.15 TgN, Table S11 in the Supplement) and higher $NH_{3(g)}$ levels in the gas phase compared to Hauglustaine et al. (2014) and other mechanisms. Among HYB cases, $NH_{3(g)}$ budgets show an inverse relationship with ~~the concentration of~~ $HNO_{3(g)}$, indicating that $HNO_{3(g)}$ acts as a limiting factor for the $NH_{3(g)}$ neutralization in the fine mode. ~~This relationship corresponds with the slightly lower~~ Given that most $HNO_{3(g)}$ is consumed by the UPTK reactions in the HYB mechanism, these results suggest that the NH_4^+ ~~budgets observed in HYB simulations (approx. 0.15 TgN, see also Table S11). Overall, this sheds light on the dynamics of with sulfate, suggesting that the mass of formed in the HYB mechanisms~~ mass formed with this configuration is mainly a product of $NH_{3(g)}$ neutralization with sulfate through the fTEQ calculation~~, given that most is consumed by the UPTK reactions~~.

The fTEQ and DBCLL mechanisms exhibit a high sensitivity in the partitioning of oxidized and reduced nitrogen to alkalinity, regardless of whether coarse NO_3^- formation is considered. When dust and SS alkalinity are neglected (fTEQ_noAlk and DBCLL_noAlk~~runs), the burdens of oxidized nitrogen are notably high (~~), oxidized nitrogen burdens rise significantly to 1.1 TgN~~). This primarily consists~~ , primarily due to the accumulation of unreacted $HNO_{3(g)}$, which ~~even slightly exceeds those obtained from the run without heterogeneous chemistry (noHC,~~ slightly exceeds the burden in the noHC run (1.05 TgN). This ~~result~~ is attributed to the sensitivity of $N_2O_{5(g)}$ hydrolysis ~~under different aerosol loadingconditions~~to aerosol loading. Conversely, ~~the burdens of reduced nitrogen~~ reduced nitrogen burdens in these schemes remain relatively low compared to other mechanisms ~~. This is mainly~~ due to the high consumption of $NH_{3(g)}$ by neutralization of $HNO_{3(g)}$, which acts as an important sink of reduced nitrogen as particulate NH_4^+. The introduction of dust and SS NVC in the reactions decreases oxidized nitrogen by an enhanced consumption of $HNO_{3(g)}$ to form NO_3^-. Furthermore, reduced nitrogen concentrations increase as a consequence of the lower availability of $HNO_{3(g)}$ to neutralize $NH_{3(g)}$. This phenomenon is similarly observed in simulations including TEQ calculations over fine (fTEQ_du-ssAlk) and over both fine and coarse modes (DBCLL_duAlk and DBCLL_du-ssAlk). Comparatively, the presence of dust and SS alkalinity decreases the oxidized nitrogen burdens by approximately 27% compared to analogous simulations neglecting NVC. However, contrasting the results between DBCLL_duAlk and DBCLL_du-ssAlk shows that while the presence of SS NVC further enhances the consumption of $HNO_{3(g)}$ by 20%, it concurrently reduces NO_3^- burdens by 5%. This is likely due to SS contributing with acidic ~~NVC~~ anions such as Cl^- and SO_4^{2-} (see Section 2.2.3), which hinders the formation of particulate NO_3^- ~~.~~ in the fine mode and leaves more $HNO_{3(g)}$ available to form coarse NO_3^- over dust. This is consistent with the spatial distributions discussed in Section 3.1.3 and the nitrogen budgets presented in Section 3.3.1 and Fig. 6.

Alkalinity leads to higher reduced nitrogen budgets due to enhanced basic conditions (high pH, as shown in ~~Figure~~ Fig. 4) facilitated by dust and SS NVC. This environment inhibits $NH_{3(g)}$ condensation over dust and SS particles, thereby increasing

the $NH_{3(g)}$ atmospheric lifetime (Table S10) and allowing it to mix with sulfate from polluted areas, as can be seen in the spatial correlation between particulate SO_4^{2-} and NH_4^+ (see discussion in Section 3.1 and Figures S4 and S7). Consequently, alkalinity facilitates the formation of NH_4^+ through the neutralization of $NH_{3(g)}$ with sulfate, contrasting with the neutralization process involving $HNO_{3(g)}$ observed in the DBCLL_noAlk simulation.

Overall, the DBCLL_du-ssAlk run aligns with the average of AeroCom in both oxidized and reduced partitions, although its reduced phase falls below EMAC levels. This discrepancy can be attributed to EMAC showing very low deposition rates of $NH_{3(g)}$ (see Table S10), which enhances its atmospheric burden.

The observational evaluation of both reduced and oxidized species, along with the monitoring stations used, can be found in the Supplementary Section S6. Overall, a general good agreement with observations is obtained. Oxidized nitrogen species exhibit low biases in all mechanisms except HYB_du-ssUPTK, which overestimates observations throughout the studied period, supporting the conclusion that UPTK coefficients used are excessively efficient. Reduced nitrogen species, while slightly underestimated, remain well within the observational variability range.

3.4 Nitrate budgets

The NO_3^- budgets from the sensitivity runs are summarized in Table 5, including burdens, wet and dry deposition, productivities, and lifetime of fine, coarse and total NO_3^-. Comparative data from previous studies (Bian et al., 2017; Karydis et al., 2016; Rémy et al., 2022; Hauglustaine et al., 2014; Jones et al., 2021) are also included. Analogous information on $HNO_{3(g)}$, $NH_{3(g)}$, ~~total~~ NH_4^+, and SO_4^{2-} can be found in ~~the~~ Supplementary Section S4 (Tables S9 to S12).

The sensitivity runs conducted in this study yield a wide range of total NO_3^- burdens, ranging from 0.09 to 1.93 Tg. Experiments neglecting coarse NO_3^- and the role of non-volatile components (NVC) fall on the lower end of this spectrum, while the HYB schemes consistently report higher burdens. The ~~fine to coarse ratio increases in those~~ coarse to fine ratio decreases in the mechanisms that neglect part or completely NVC in the nitrate partitioning, and HYB runs consistently simulate the highest coarse burdens (0.57 to 1.43 Tg). Compared with the reported values in the literature, both HYB (1.15 to 1.93 Tg) and DBCLL (1.04 to 1.44 Tg) schemes considering NVC fall within the ~~uper range of~~ upper range of the Aerocom total NO_3^- burden ~~intercomparison study~~ (Bian et al., 2017) and above specific global ~~systems~~ models such as IFS (Rémy et al., 2022) or MetOffice UM (Jones et al., 2021). Similar differences are found in total annual depositions with ranges that span a factor of two among schemes. For wet deposition, DBCLL mechanisms show values ranging from 37 to 45 Tg/y, within the lower half of the range found in the literature (45±30 Tg/y for AeroCom to 75 Tg/y for IFS), while HYB consistently ~~simulate~~ simulates higher estimates even beyond reported values (63 to 120 Tg). This feature is also seen in the dry deposition. ~~Interestingly~~Consequently, the lifetimes of total NO_3^- shown in Table 5 range from 2.3 to 2.6 days for ~~global models adopting~~ HYB schemes, systematically estimating the lowest lifetimes~~, while~~. Conversely, models introducing reversible partitioning provide longer lifetimes (2.6 to 4.9 days). To better understand the possible reasons for such a wide range of estimates, in the next lines we analyze some of our sensitivity runs compared to similar systems in the literature.

Figure 7. Average 2018 nitrogen budgets (top) and depositions (bottom) for the different dust heterogeneous chemistry mechanisms. ~~In each~~ Each plot ~~, reduced and~~ shows oxidized ~~species~~ (top rows) and reduced (bottom rows) mass for each mechanism (in columns). They are compared ~~to the~~ with literature references (three last right columns).

Table 5. Results for fine, coarse and total particulate NO_3^- obtained with the studied heterogeneous chemistry mechanisms. Results from the literature references are reported at the end of the ~~Table~~table: ~~the~~ The average of all the participating models in the intercomparison AeroCom phase III nitrate experiment for 2008 (*AeroCom*), specifying their standard deviation (~~*STD*~~*STD AeroCom*), ~~and~~ results from the GMI model (*GMI*, using a similar HYB approach with UPTK reactions on dust and SS), and results from the EMAC model (*EMAC 2008*, ~~that uses~~ using a similar approach to DBCLL_du-ssAlk). Also using the EMAC model, results obtained by the Karydis et al. (2016) study are reported as *EMAC 2005-2008*. Results from models using a similar approach to HYB_du-ssUPTK are reported as *IFS* for Rémy et al. (2022), *LMDz-INCA* for Hauglustaine et al. (2014) and *MetOffice UM* for Jones et al. (2021).

NO_3^-	**Burden (Tg)**			**Wet Dep. (Tg y-1)**			**Dry Dep. (Tg y-1)**			**Total Dep. (Tg y-1)**			**Production (Tg y-1)**			**Lifetime (days)**		
Experiment	Fine	Coarse	**Total**	Fine	Coarse	**Total**	Fine	Coarse	**Total**	Fine	Coarse	**Total**	Fine	Coarse	**Total**	Fine	Coarse	**Total**
fTEQ_noAlk	0.09	-	**0.09**	4.6	-	**4.6**	2.0	-	**2.0**	6.6	-	**6.6**	6.6	-	**6.6**	2.6	0.0	**2.6**
fTEQ_du-ssAlk	0.66	-	**0.66**	36.1	-	**36.1**	7.4	-	**7.4**	43.5	-	**43.5**	43.6	-	**43.6**	2.7	0.0	**2.7**
HYB_duUPTK	0.58	0.57	**1.15**	25.8	37.9	**63.7**	5.4	11.1	**16.5**	31.2	49.0	**80.2**	31.3	48.9	**80.2**	3.4	2.1	**2.6**
HYB_du-ssUPTK	0.55	1.20	**1.75**	10.7	103.4	**114.1**	2.9	23.6	**26.5**	13.6	127.0	**140.6**	13.6	126.9	**140.5**	7.4	1.7	**2.3**
HYB_gdust=0.1	0.50	1.43	**1.93**	8.4	111.9	**120.4**	2.3	27.0	**29.3**	10.7	138.9	**149.7**	10.8	138.9	**149.6**	8.5	1.9	**2.4**
HYB_DL	0.41	1.26	**1.68**	2.8	109.7	**112.6**	1.4	25.7	**27.1**	4.2	135.4	**139.6**	4.2	135.3	**139.5**	17.8	1.7	**2.2**
DBCLL_noAlk	0.06	0.00	**0.06**	2.5	0.0	**2.6**	1.6	0.1	**1.7**	4.1	0.1	**4.2**	4.2	0.1	**4.3**	2.6	2.8	**2.6**
DBCLL_duAlk	0.96	0.47	**1.44**	26.5	11.0	**37.5**	8.3	8.2	**16.5**	34.8	19.3	**54.0**	34.7	19.2	**53.9**	5.1	4.5	**4.9**
DBCLL_du-ssAlk	0.28	0.78	**1.07**	18.2	27.5	**45.7**	4.0	12.6	**16.5**	22.2	40.1	**62.3**	22.3	40.0	**62.2**	2.3	3.6	**3.1**
DBCLL_ClaqAlk	0.41	0.63	**1.04**	17.4	27.8	**45.2**	3.8	12.9	**16.7**	21.2	40.7	**61.9**	21.3	40.6	**61.9**	3.5	2.8	**3.1**
AeroCom	-	-	**0.63**	-	-	**45.9**	-	-	**20.7**	-	-	**66.6**	-	-	**60.6**	-	-	**5.0**
STD AeroCom	-	-	**±0.56**	-	-	**±30.7**	-	-	**±19.5**	-	-	**±50.2**	-	-	**±45.9**	-	-	**±2.3**
GMI	-	-	**0.97**	-	-	**43.3**	-	-	**14.8**	-	-	**58.1**	-	-	**59.3**	-	-	**6.0**
EMAC 2008[1]	-	-	**0.67**	-	-	**0.0**	-	-	**46.3**	-	-	**46.3**	-	-	**-**	-	-	**-**
EMAC 2005-2008[2]	-	-	**0.44**	-	-	**-**	-	-	**-**	-	-	**-**	-	-	**-**	-	-	**-**
IFS[3]	0.47	0.35	**0.82**	35.9	39.6	**75.5**	4.6	23.8	**28.4**	40.5	63.4	**103.9**	40.5	63.4	**103.6**	4.2	2.1	**3.0**
LMDz-INCA	0.22	0.58	**0.80**	-	-	**56.1**	-	-	**7.4**	-	-	**63.5**	14.1	49.5	**63.6**	-	-	**4.6**
MetOffice UM[4]	0.49	0.40	**0.89**	-	-	**63.3**	-	-	**39.4**	-	-	**102.8**	27.9	73.5	**101.4**	6.2	2.0	**3.2**

1. From Bian et al. (2017).
2. From Karydis et al. (2016).
3. Fine NO_3^- reported from neutralization of nitric acid, ammonia and sulfate. Coarse NO_3^- from heterogeneous chemistry. (Rémy et al., 2022).
4. Jones et al. (2021) performs two sensitivity tests to the accommodation coefficient used for NO_3^- formation in the fine mode: *FAST* with 0.193 and *SLOW* with 0.001. Here, results from the *FAST* test are reported on the basis that they present similar fine NO_3^- formation rates to our average fine NO_3^- results.

The assumption of irreversibility of ~~nitrate~~ $HNO_{3(g)}$ condensation onto dust and SS particles (HYB_du-ssUPTK run) produces the largest increase in coarse NO_3^- formation, exceeding values reported in the literature. For instance, the HYB_du-ssUPTK model reports a total NO_3^- burden of 1.75 Tg, which is higher than the AeroCom range (0.63 ± 0.56 Tg) and values from models such as EMAC in AeroCom (Bian et al., 2017), as well as findings from Bian et al. (2017), Jones et al. (2021), Rémy et al. (2022) and Hauglustaine et al. (2014) (0.67, 0.89, 0.82, and 0.80 Tg, respectively). ~~Additionally~~Interestingly, the results surpass those from three AeroCom models (EMEP, INCA, and GMI) using a similar HYB approach with UPTK reactions on dust and SS, which range from 0.26 to 0.95 Tg of total NO_3^- (see ~~(Bian et al., 2017)~~Bian et al. (2017)). Multiple reasons could explain ~~some of the disagreements~~ the excessive NO_3^- formation found in this comparison. For instance, Hauglustaine et al. (2014) employs a similar HYB implementation and UPTK coefficients for dust as the HYB_du-ssUPTK run, although a different parametrization for the $HNO_{3(g)}$ UPTK on SS. Despite Hauglustaine et al. (2014) also overestimating particulate NO_3^- with a global normalized mean bias of +68%, the HYB_du-ssUPTK simulation still reports higher burdens for NO_3^- (0.80 vs. 1.75 Tg~~vs 0.80 Tg~~) and lower burdens for $HNO_{3(g)}$ (~~0.69 vs~~ 1.35 vs. 0.69 Tg, Table S9)~~compared to Hauglustaine et al. (2014). The~~ . Our study also presents lower NO_x emissions ~~in our study~~ than Hauglustaine et al. (2014) , which would imply a reduced availability of precursor gases ~~, which~~ that would typically result in lower NO_3^- formation (40.8 vs. 46.TgN, Table S1 ~~). However, the high uptake coefficients employed for UPTK on SS may be excessively efficient as discussed previously in Section 3.1.2 and 3.2.~~ in the Supplement). ~~The~~ Additionally, the run neglecting the uptake on SS (HYB_duUPTK) reports values closer to observations (Section 3.2) and ~~reported~~ to the budgets in the literature. ~~Consequently, these results can be explained by the much lower UPTK coefficient for SS employed in the~~

This suggests that the high coefficients employed for $HNO_{3(g)}$ UPTK on SS may be excessively efficient. This conclusion is consistent with analyses discussed in previous Sections 3.1.2, 3.2 and 3.3. By comparison, other systems (Hauglustaine et al., 2014; Jones et al., 2021; Rémy et al., 2022) typically employ much lower UPTK coefficients for SS compared to our implementation.

Therefore, a function for the uptake coefficient on SS dependent on relative humidity and on SS particle size should be considered in future works, following the same approach as for dust (~~equation 2)and Hauglustaine et al. (2014)~~Eq. 2). However, such a function has not clearly been determined in the literature. While Hauglustaine et al. (2014) assumes a BET isotherm for the $HNO_{3(g)}$ UPTK on SS similar to the UPTK on dust (Fairlie et al., 2010), it remains unclear if this approach is suitable for SS as it is for dust. To our best knowledge, the most appropriate alternative to the assumption of averaged UPTK coefficients for SS would be to fit a function to the experimental values reported by Liu et al. (2007), which provides uptake coefficient dependencies with relative humidity and particle size. However, several discrepancies between Liu et al. (2007) and previous studies still remain unresolved (Tolocka et al., 2004; Saul et al., 2006), presenting difficulties in reaching a common agreement on ~~an~~ a $HNO_{3(g)}$ UPTK coefficient function on SS.

Beyond the excessive NO_3^- formation driven by the UPTK on SS, the sole implementation of $HNO_{3(g)}$ UPTK on dust (HYB_duUPTK run) still slightly exceeds particulate NO_3^- burdens and deposition rates reported by the references (Table 5). This is also observed when compared to observational surface concentrations (see Section 3.2), suggesting that the sole UPTK

on dust results in excessive NO_3^- formation. ~~.~~Given that previous studies have consistently shown non negligible $HNO_{3(g)}$ uptake on SS (Myhre et al., 2006; Athanasopoulou et al., 2008), these biases could be explained by 1) an excessive UPTK coefficient employed for $HNO_{3(g)}$ UPTK on dust, 2) the inherent inappropriateness of the irreversible condensation assumption of gas species on particles to simulate particulate NO_3^- formation, or 3) the different atmospheric lifetime of coarse particles among different systems. ~~Regarding~~ Regarding possible issues in the UPTK parameterization on dust adopted in our study, the inclusion of the scaling factor for alkalinity added to the dust uptake coefficients (*Sc* in ~~equation~~ Eq. 2) could contribute to excessively high UPTK rates. This alkalinity scaling factor is based on the NVC fractions provided by Fairlie et al. (2010), namely calcium and magnesium (see Section 2.2.1). Since our study includes additional NVC (i.e. potassium and sodium), this estimation might not be representative and could result in excessive condensation. However, additional information on the NVC content in Fairlie et al. (2010) is missing to refine our approach. Concerning the possible inappropriateness of the irreversible condensation assumption, indeed models implementing such an approach with similar UPTK coefficients tend to overestimate particulate NO_3^- formation (Hauglustaine et al., 2014; Jones et al., 2021; Rémy et al., 2022). This might point at the assumption of reversible evaporation-condensation of gas species or at the inclusion of alkalinity consumption as necessary implementations to improve the results.

Lastly, a longer lifetime of coarse particles such as dust or SS could contribute to enhance NO_3^- production regardless of the adopted mechanism. Spada et al. (2013) intercompared different SS emission schemes in the MONARCH model and reported lifetimes ranging from 4 to 12 days including results from literature. These findings highlight significant differences in emission, transport, and sedimentation schemes among global models, which are not negligible. Such differences could explain part of the variations identified in our analysis. For instance, if a model assumes a longer lifetime for coarse particles, it would result in a prolonged period during which $HNO_{3(g)}$ can condense onto these particles, thus increasing the overall burden of particulate NO_3^-. Understanding and standardizing these lifetimes could be crucial for achieving more consistent and accurate predictions of NO_3^- aerosol formation across different ~~modeling frameworks.~~modelling frameworks.

Linking with the limitations of irreversible approaches, we finally analyze the DBCLL runs to illustrate the paramount role of alkalinity in NO_3^- formation. Neglecting NVC in the partitioning (DBCLL_noAlk) results in negligible NO_3^- formation, with a burden of just 0.06 Tg in the fine mode (Table 5). In contrast, only considering dust alkalinity (DBCLL_duAlk) significantly increases the burden of both fine and coarse modes to 0.96 and 0.47 Tg, respectively, which exceeds estimates reported in other works (Hauglustaine et al., 2014; Jones et al., 2021; Rémy et al., 2022).

~~Comparing the obtained burdens and size distributions with those reported by Rémy et al. (2022), Hauglustaine et al. (2014), and Jones et al. (2021) (Table 5), we observe that the total values are notably high when only dust alkalinity is considered. This discrepancy can be attributed to excessive fine formation, as already noted in the observational evaluation (see Section 3.2). This indicates that while the DBCLL approach improves the representation of alkalinity effects compared to the irreversible mechanisms, it still tends to overestimate the fine mode , suggesting a need for further refinement in the parameterization of NVC effects to achieve more accurate nitrate aerosol predictions.~~

Additionally, accounting for SS alkalinity (reaction R12 from Table 1), the DBCLL_du-ssAlk run shifts particulate NO_3^- formation from fine towards the coarse mode, increasing coarse burdens from 0.47 in DBCLL_duAlk to 0.78 Tg. Consequently, this leads to higher total NO_3^- deposition rates, rising from 54 to 62 Tg/y. Including both dust and SS alkalinity results in a notable agreement for total NO_3^- (1.07 Tg) and $HNO_{3(g)}$ (2.53 Tg) burdens with values reported in the literature. This improvement highlights the importance of considering both dust and SS alkalinity in accurately ~~modeling~~ modelling NO_3^- formation and deposition rates in atmospheric chemistry simulations.

Some differences emerge when comparing the NO_3^- size distribution against references that report fine and coarse NO_3^- budgets. Specifically, the fine NO_3^- burden tends to be on the lower end of the references range (0.28 Tg vs. 0.39 Tg on average), while the coarse NO_3^- burden is on the higher end (0.78 Tg vs. 0.54 Tg on average), although ~~it should be considered~~ the relatively high variability between the references in both modes should be considered. Despite these variations, accounting for alkalinity significantly improves the agreement of NO_3^- lifetime (3.1 days) with AeroCom (5.0±2.3 days), Rémy et al. (2022) (3.0 days) and Jones et al. (2021) (3.2 days).

To delve into the differences observed between simulations employing constant dust alkalinity derived from Journet et al. (2014) (DBCLL_du-ssAlk) and from Claquin et al. (1999) (DBCLL_ClaqAlk, discussed in Supplementary Section S5) as shown in Table 5, it becomes evident that DBCLL_ClaqAlk results in a noticeable shift towards fine NO_3^- formation (from 0.28 Tg to 0.40 Tg), with fine NO_3^- increasing its lifetime (2.3 to 3.5 days) and coarse NO_3^- decreasing it (3.6 to 2.8 days). Also, we observe a slightly higher burden of $HNO_{3(g)}$ (from 2.53 Tg to 2.58 Tg) and a lower burden of $NH_{3(g)}$ (from 0.35 Tg to 0.31 Tg) (see Supplementary Tables S9 and S10). This can be attributed to the higher fraction of Ca^{2+} NVC in the fine mode derived from Journet et al. (2014) (5.73%) compared to Claquin et al. (1999) (3.68%)~~, while both datasets present closer fractions of calcium~~ . Both datasets present more similar fractions of Ca^{2+} for the coarse mode (4.61% vs. 3.74%) (see Supplementary Tables S4 and S6). This underscores the important role that Ca^{2+} NVC plays in heterogeneous chemistry~~, surpassing the higher~~ . As a matter of fact, Ca^{2+} fractions surpasses the fractions of other NVC in the Claquin et al. (1999) dataset (0.07% Na, 0.78% K and 0.43% Mg, Tables S3 to S6). ~~Also, we observe a slightly higher burden of (from 2.53 Tg to 2.58 Tg) and a lower burden of (from 0.35 Tg to 0.31 Tg) (see Supplementary Tables S9 and S10). This~~ The comparison between DBCLL_du-ssAlk and DBCLL_ClaqAlk provides a quantification of the impact that mineral distributions among dust sources (especially calcite) has on gas-aerosol partitioning, specially in the formation of particulate NO_3^- ~~, and~~ . It also highlights the importance of advancing on the representation of mineralogical dust composition at the global scale and its regional variability.

Finally, we compare the outcomes from the DBCLL_du-ssAlk simulation with those reported by the EMAC model, which employs a similar approach to the DBCLL mechanism and also accounts for dust and SS alkalinity (see Section 3.1.3). The analysis is performed against ~~the~~ two studies where EMAC budgets were reported: the AeroCom intercomparison nitrate experiment (Bian et al., 2017) and Karydis et al. (2016) (Table 5). It's notable that the total NO_3^- burden (1.07 Tg) in DBCLL_du-ssAlk exceeds both the EMAC results from AeroCom (0.67 Tg) and Karydis et al. (2016) (0.44 Tg), although our findings show reasonable agreement with observations, especially over Asia (see Section 3.2). Regarding the total budget of $HNO_{3(g)}$

(2.53 Tg), despite our result closely matching the AeroCom experiment average (2.50±1.83 Tg, Table S9), it is below the values reported by EMAC in this experiment (3.10 Tg) while significantly exceeding results from Karydis et al. (2016) (1.65 Tg). These outcomes reveal intrinsic differences in the rates of $HNO_{3(g)}$ condensation on dust and SS between both models. Conversely, the $NH_{3(g)}$ burden (0.35 Tg) in our simulation falls below those reported by both studies (0.85 and 0.82 Tg, respectively), potentially due to the high formation of particulate NO_3^- over dust and SS NVC in our study. Nevertheless, the resulting burdens for NH_4^+ align with both references (0.22 vs. 0.19 and 0.17 Tg for EMAC in AeroCom and Karydis et al. (2016), respectively). Various factors could explain the differences observed between EMAC and the DBCLL_du-ssAlk simulation: the different simulated periods between our study, Karydis et al. (2016) and AeroCom (2018 vs. 2005-2008 average and 2008, respectively), the varying NVC content assumed for dust and SS between DBCLL_du-ssAlk and EMAC (Section 3.1.3), and the intrinsic differences in the heterogeneous chemistry mechanisms employed in both models (DIFFLIM and DBCLL in MONARCH and bulk TEQ followed by DIFFLIM used in ~~Karydis et al. (2016)~~EMAC). Despite their conceptual equivalence, our results demonstrate that these mechanisms may yield different outcomes.

4 Conclusions

In this study, we conducted a comprehensive exploration of the processes driving nitrate formation on fine and coarse particles ~~globally~~ at a global scale using the MONARCH atmospheric model. Our sensitivity simulations incorporated state-of-the-art dust heterogeneous chemistry mechanisms, including reversible condensation-evaporation through thermodynamic equilibrium (TEQ) and irreversible uptake reactions (UPTK) between gas and aerosol phases. Three mechanisms for particulate nitrate formation were implemented: (1) fTEQ, which considers ~~reversible condensation-evaporation focusing on fine nitrate without accounting for~~ fine nitrate formation through reversible TEQ reactions and neglects coarse nitrate; (2) HYB, where fine nitrate forms via TEQ with a subsequent irreversible uptake of $HNO_{3(g)}$ on coarse particles; and (3) DBCLL, which allows for both fine and coarse nitrate formation through ~~a reversible process~~ reversible TEQ processes with kinetic gas limitation.

Key assumptions such as uptake coefficients, reversible partitioning, and the inclusion of dust and sea-salt alkalinity were thoroughly assessed. Global average dust alkalinity was sourced from previous dust mineralogy simulations (Gonçalves Ageitos et al., 2023) using Journet et al. (2014) and Claquin et al. (1999) mineral atlases, while globally homogeneous sea-salt alkalinity values are derived from Seinfeld and Pandis (2006). We evaluated annual cycle surface concentrations against observations for various atmospheric species and compared global spatial distributions and budgets with existing literature. Additionally, we investigated the partitioning of nitrogen species and assessed the impact of dust and sea-salt heterogeneous chemistry on total nitrogen budgets.

Neglecting coarse nitrate formation (fTEQ_du-ssAlk run) results in ~~fine nitrate~~ budgets and distributions of fine nitrate that closely match observational surface concentrations of total nitrate (-0.09 $\mu g\ m^{-3}$ bias, 0.88 correlation). This good agreement suggests that observational stations are dominated by fine nitrate concentrations or that fine nitrate formation is overestimated in this run. Since this mechanism aligns with references forming both fine and coarse nitrate (Bian et al., 2017; Rémy et al.,

2019; Hauglustaine et al., 2014), it likely compensates for the lack of coarse nitrate formation through the instantaneous TEQ of gas species in the fine mode, thus not accurately reflecting the size distribution of particles.

The formation of coarse nitrate through the irreversible uptake of $HNO_{3(g)}$ on coarse particles (HYB methodologies) is highly sensitive to whether the $HNO_{3(g)}$ uptake is assumed to occur solely on dust or on both dust and sea-salt particles. The uptake solely on dust (HYB_duUPTK run) closely reproduces fine and total particulate nitrate seasonality (correlations of 0.8 and 0.9, respectively), although it slightly overestimates observations (+0.29 $\mu g\ m^{-3}$ bias), particularly over Asia, and nitrate budgets compared to the literature (1.15 vs. 0.74 Tg on average). An excessively efficient $HNO_{3(g)}$ uptake on dust particles could explain such a performance~~that~~, which could be improved through more accurate scaling factors adopted for alkalinity. However, the lack of information in the literature poses a challenge in implementing such adjustments.

The introduction of the $HNO_{3(g)}$ uptake on sea-salt (HYB_du-ssUPTK run) further increases the formation of coarse nitrate, exceeding the reported burdens in the literature (1.75 vs. 0.74 Tg from the references' average) and overestimating observational surface concentrations (+1.50 $\mu g\ m^{-3}$ bias). Moreover, some deviations with respect to references are observed in the latitude and magnitude of the transatlantic transport of coarse nitrate formed during long-range transport of dust and sea-salt. These findings indicate the need for a revision of the $HNO_{3(g)}$ uptake coefficients on sea-salt. A potential alternative could involve its implementation as a function of relative humidity and particle size, aligning it with experimental data from Liu et al. (2007), although discrepancies with earlier experimental studies present difficulties in determining consistent uptake coefficients for sea-salt.

The reversible condensation-evaporation of gas species on both fine and coarse modes of dust and sea-salt (DBCLL mechanism) highlights the paramount importance of accounting for alkalinity to derive consistent results both globally and across continents. Remarkably, the DBCLL_du-ssAlk run, which accounts for dust and sea-salt alkalinity, effectively captures monthly global concentrations of fine and total nitrate, with correlations of 0.82 and 0.78 and concentrations slightly underestimated with -0.18 and -0.10 $\mu g\ m^{-3}$ bias, respectively. These good results extend to particulate ammonium for both fine and total fractions (-0.02 and 0.08 $\mu g\ m^{-3}$ bias, respectively). The consistent excessive formation of total $PM_{2.5}$ (+20 $\mu g\ m^{-3}$ bias) over Asia across the experiments may be explained by the absence of anthropogenic coarse dust emissions in the employed CAMS inventory. This omission leads to the overestimation of fine particulate matter formation, compensating for the misrepresentation of coarse particulate matter.~~Accounting for~~ Including both dust and sea-salt alkalinity in the DBCLL mechanism ~~substantially increases~~ significantly raises global pH levels, which enhances particulate nitrate formation by 94% in comparison to the same mechanism with no alkalinity~~, and decreases~~. This incorporation also reduces NO_x budgets and lowers the reduced nitrogen burden due to an increase of ammonium formation. Moreover, the sole inclusion of sea-salt alkalinity is identified as responsible of substantially shifting the size partitioning of particulate nitrate from fine (-72%) to coarse (+63%), along with the rise in wet deposition of particulate nitrate due to high scavenging rate of sea-salt particles, overall reducing the total aerosol nitrate atmospheric lifetime from 4.9 to 3.1 days.

Comparison with references reveals that while surface concentrations in the DBCLL_du-ssAlk simulation align well with observations, its global burden (1.07 Tg) sits at the upper limit of AeroCom's reported range (0.63±0.56 Tg) and slightly exceeds the average reported by other studies (0.74 Tg). Fundamental differences between the models, like the alkalinity

factors, intrinsic differences in the heterogeneous chemistry, aerosol representation and transport processes can partly explain the wide range of results reported in the literature. Overall, the DBCLL_du-ssAlk scheme demonstrates the best accuracy compared to the other tested configurations, as evidenced by its closer alignment with observations.

A comparison between runs adopting the two different dust alkalinity fractions derived from averaging simulations using ~~Claquin et al. (1999) and Journet et al. (2014)~~ Journet et al. (2014) and Claquin et al. (1999) soil mineralogy datasets as described in Gonçalves Ageitos et al. (2023) reveals that assumptions on the dust composition are crucial, particularly influencing particulate nitrate size distribution. A decrease from 5.17% to 3.68% in ~~Ca~~ ionic Ca^{2+} fractions, along with slight increases in Na, K and Mg between Journet et al. (2014) and Claquin et al. (1999) leads to a +35% increase in fine and -21% decrease in coarse nitrate formation. This high sensitivity is especially attributed to the lower calcite content and its different size distribution in the Claquin et al. (1999) database compared to Journet et al. (2014).

~~Comparison with references reveals that while surface concentrations in the DBCLL_du-ssAlk simulation align well with observations, its global burden (1.07 Tg) sits at the upper limit of AeroCom's reported range (0.63±0.56 Tg) and slightly exceeds the average reported by other studies (0.74 Tg). Fundamental differences between the models, like the alkalinity factors, intrinsic differences in the heterogeneous chemistry, aerosol representation and transport processes can partly explain the wide range of results reported in~~ It is important to note that our computational cost analysis reveals highly similar processing times across the sensitivity runs, with a standard variation of only 5%. This is within the estimated variability of the supercomputing resources utilized for the present work. Consequently, the ~~literature~~computational cost does not indicate a clear advantage in efficiency for any of the methodologies assessed.

This study establishes a crucial benchmark for future investigations into the impact of incorporating regional variations in dust alkalinity, as derived from Claquin et al. (1999), Journet et al. (2014), and the upcoming spectroscopically-based EMIT surface mineralogical dataset (Green et al., 2018; Thompson et al., 2024; Brodrick et al., 2023), on the formation of particulate nitrate and atmospheric composition. The findings also evaluate the significance of dust and sea-salt alkalinity in inorganic aerosol heterogeneous chemistry, providing insights into the optimal representation of dust alkalinity in atmospheric models. Ultimately, these results aim to enhance the capability of atmospheric and climate models to simulate the formation of aerosol nitrate, ammonium, and sulfate, potentially improving our ability to estimate the radiative effects of these species in climate projections.

Code availability. The MONARCH code is available at https://earth.bsc.es/gitlab/es/monarch (last access: 21 July 2024) and the HERMESv3_GR code is accessible at https://earth.bsc.es/gitlab/es/hermesv3_gr (last access: 21 July 2024).

Data availability. The GHOST dataset is made freely available via the following repository: https://doi.org/10.5281/zenodo.10637449 (Bowdalo et al., 2024). The model output used in this work is available in the Zenodo data repository at https://doi.org/10.5281/zenodo.12789730 (Sousse, 2024).

Author contributions. RS, OJ and CPG-P developed the model, designed the methodology and the conceptualization, and performed the investigation and analysis of the results. RS designed and conducted the sensitivity simulations, and the results' postprocessing, validation and visualization, assisted by OJ and CP. MGA provided the simulations with the average mineralogy from the utilized mineral dust datasets. DB provided the observational evaluation data under request, developed the GHOST dataset and the evaluation software. MGV provided the CAMS-ANTv4.2 emission dataset under request and developed the HERMESv3_GR emission model. RS wrote the manuscript, which was re-edited by OJ and CPG-P, with contributions from all other co-authors.

Competing interests. The authors declare that they have no competing interests.

Acknowledgements. This work was funded by the European Research Council (ERC) under the Horizon 2020 research and innovation program through the ERC Consolidator Grant FRAGMENT (grant agreement no. 773051). We additionally acknowledge support from the AXA Research Fund through the AXA Chair on Sand and Dust Storms at the Barcelona Supercomputing Center (BSC), the Spanish Ministerio de Economía y Competitividad through the HEAVY project (grant PID2022-140365OB-I funded by MICIU/AEI/10.13039/501100011033 and by ERDF, EU), the European Union's Horizon 2020 research and innovation program under grant agreement no. 821205 (FORCeS) and the Department of Research and Universities of the Government of Catalonia via the Research Group Atmospheric Composition (code 2021 SGR 01550). RS was funded by the predoctoral program AGAUR-FI ajuts (2023 FI-3 00065) Joan Oró, which is backed by the Secretariat of Universities and Research of the Department of Research and Universities of the Generalitat of Catalonia, as well as the European Social Plus Fund.

The authors acknowledge the computer resources at Marenostrum and the technical support provided by Barcelona Supercomputing Center (RES-AECT-2022-3-0013, RES-AECT-2023-2-0008, RES-AECT-2023-3-0026), with special mention to Alejandro García, Carles Tena, Gilbert Montane and Albert Vila.

References

Adebiyi, A., Kok, J. F., Murray, B. J., Ryder, C. L., Stuut, J. B. W., Kahn, R. A., Knippertz, P., Formenti, P., Mahowald, N. M., García-Pando, C. P., Klose, M., Ansmann, A., Samset, B. H., Ito, A., Balkanski, Y., Biagio, C. D., Romanias, M. N., Huang, Y., and Meng, J.: A review of coarse mineral dust in the Earth system, Aeolian Research, 60, https://doi.org/10.1016/j.aeolia.2022.100849, 2023.

Adebiyi, A. A. and Kok, J. F.: Climate models miss most of the coarse dust in the atmosphere, Science Advances, 6, 1–10, https://doi.org/10.1126/sciadv.aaz9507, 2020.

Athanasopoulou, E., Tombrou, M., Pandis, S. N., and Russell, A. G.: The role of sea-salt emissions and heterogeneous chemistry in the air quality of polluted coastal areas, Atmospheric Chemistry and Physics, 8, 5755–5769, https://doi.org/10.5194/acp-8-5755-2008, 2008.

Badia, A., Jorba, O., Voulgarakis, A., Dabdub, D., García-Pando, C. P., Hilboll, A., Gonçalves, M., and Janjic, Z.: Description and evaluation of the Multiscale Online Nonhydrostatic AtmospheRe CHemistry model (NMMB-MONARCH) version 1.0: gas-phase chemistry at global scale, Geosci. Model Dev, 10, 609–638, https://doi.org/10.5194/gmd-10-609-2017, 2017.

Bauer, S. E., Balkanski, Y., Schulz, M., Hauglustaine, D. A., and Dentener, F.: Global modeling of heterogeneous chemistry on mineral aerosol surfaces: Influence on tropospheric ozone chemistry and comparison to observations, Journal of Geophysical Research: Atmospheres, 109, 2304, https://doi.org/https://doi.org/10.1029/2003JD003868, 2004.

Bauer, S. E., Mishchenko, M. I., Lacis, A. A., Zhang, S., Perlwitz, J., and Metzger, S. M.: Do sulfate and nitrate coatings on mineral dust have important effects on radiative properties and climate modeling?, Journal of Geophysical Research: Atmospheres, 112, 6307, https://doi.org/10.1029/2005JD006977, 2007.

Bauer, S. E., Tsigaridis, K., and Miller, R.: Significant atmospheric aerosol pollution caused by world food cultivation, Geophysical Research Letters, 43, 5394–5400, https://doi.org/10.1002/2016GL068354, 2016.

Bellouin, N., Rae, J., Jones, A., Johnson, C., Haywood, J., and Boucher, O.: Aerosol forcing in the Climate Model Intercomparison Project (CMIP5) simulations by HadGEM2-ES and the role of ammonium nitrate, Journal of Geophysical Research Atmospheres, 116, https://doi.org/10.1029/2011JD016074, 2011.

Benduhn, F., Schallock, J., and Lawrence, M. G.: Early growth dynamical implications for the steerability of stratospheric solar radiation management via sulfur aerosol particles, Geophysical Research Letters, 43, 9956–9963, https://doi.org/https://doi.org/10.1002/2016GL070701, 2016.

Bergas-Massó, E., Ageitos, M. G., Myriokefalitakis, S., Miller, R. L., van Noije, T., Sager, P. L., Pinto, G. M., and García-Pando, C. P.: Pre-Industrial, Present and Future Atmospheric Soluble Iron Deposition and the Role of Aerosol Acidity and Oxalate Under CMIP6 Emissions, Earth's Future, 11, https://doi.org/10.1029/2022ef003353, 2023.

Betts, A. K. and Miller, M. J.: A new convective adjustment scheme. Part II: Single column tests using GATE wave, BOMEX, ATEX and arctic air-mass data sets, Quarterly Journal of the Royal Meteorological Society, 112, 693–709, https://doi.org/10.1002/QJ.49711247308, 1986.

Bian, H., Chin, M., Rodriguez, J. M., Yu, H., Penner, J. E., and Strahan, S.: Sensitivity of aerosol optical thickness and aerosol direct radiative effect to relative humidity, Atmospheric Chemistry and Physics, 9, 2375–2386, https://doi.org/10.5194/ACP-9-2375-2009, 2009.

Bian, H., Chin, M., Hauglustaine, D. A., Schulz, M., Myhre, G., Bauer, S. E., Lund, M. T., Karydis, V. A., Kucsera, T. L., Pan, X., Pozzer, A., Skeie, R. B., Steenrod, S. D., Sudo, K., Tsigaridis, K., Tsimpidi, A. P., and Tsyro, S. G.: Investigation of global particulate nitrate from the AeroCom phase III experiment, Atmospheric Chemistry and Physics, 17, 12 911–12 940, https://doi.org/10.5194/acp-17-12911-2017, 2017.

Boucher, O., Randall, D., Artaxo, P., Bretherton, C., Artaxo, P., Bretherton, C., Feingold, G., Forster, P., Kerminen, V.-M., Kondo, Y., Liao, H., Lohmann, U., Rasch, P., Satheesh, S., Sherwood, S., Stevens, B., and Zhang, X.-Y.: Clouds and Aerosols. In: Climate Change 2013: The Physical Science Basis. Contribution of Working Group I to the Fifth Assessment Report of the Intergovernmental Panel on Climate Change, 2013.

Bowdalo, D., Basart, S., Guevara, M., Jorba, O., Pérez García-Pando, C., Jaimes Palomera, M., Rivera Hernandez, O., Puchalski, M., Gay, D., Klausen, J., Moreno, S., Netcheva, S., and Tarasova, O.: GHOST: A globally harmonised dataset of surface atmospheric composition measurements, Earth System Science Data Discussions, 2024, 1–137, https://doi.org/10.5194/essd-2023-397, 2024.

Brodrick, P., Okin, G., Ochoa, F., Thompson, D., Clark, R., Ehlmann, B., Keebler, A., Miller, R., Mohawald, N., Ginoux, P., Garcia-Pando, C., Goncalves, M., and Green, R.: EMIT L3 Aggregated Mineral Spectral Abundance and Uncertainty 0.5 Deg V001 [Data set], https://doi.org/10.5067/EMIT/EMITL3ASA.001, [Online; Accessed 2024-03-13], 2023.

Burkholder, J. B., Sander, S. P., Abbatt, J. P. D., Barker, J. R., Cappa, C., Crounse, J. D., Dibble, T. S., Huie, R. E., Kolb, C. E., Kurylo, M. J., Orkin, V. L., Percival, C. J., Wilmouth, D. M., and Wine, P. H.: Chemical Kinetics and Photochemical Data for Use in Atmospheric Studies Evaluation Number 19 NASA Panel for Data Evaluation, 2020.

Byun, D.: Dynamically Consistent Formulations in Meteorological and Air Quality Models for Multiscale Atmospheric Studies. Part I: Governing Equations in a Generalized Coordinate System, Journal of the Atmospheric Sciences, 56, 3789–3807, https://api.semanticscholar.org/CorpusID:121915583, 1999.

Capaldo, K. P., Pilinis, C., and Pandis, S. N.: A computationally efficient hybrid approach for dynamic gas/aerosol transfer in air quality models, Atmospheric Environment, 34, 3617–3627, https://doi.org/10.1016/s1352-2310(00)00092-3, 2000.

Chin, M., Ginoux, P., Kinne, S., Torres, O., Holben, B. N., Duncan, B. N., Martin, R. V., Logan, J. A., Higurashi, A., and Nakajima, T.: Tropospheric Aerosol Optical Thickness from the GOCART Model and Comparisons with Satellite and Sun Photometer Measurements, http://weather.engin.umich.edu/, 2002.

Claquin, T., Schulz, M., and Balkanski, Y. J.: Modeling the mineralogy of atmospheric dust sources, Journal of Geophysical Research: Atmospheres, 104, 22 243–22 256, https://doi.org/10.1029/1999JD900416, 1999.

Crowley, J. N., Ammann, M., Cox, R. A., Hynes, R. G., Jenkin, M. E., Mellouki, A., Rossi, M. J., Troe, J., and Wallington, T. J.: Atmospheric Chemistry and Physics Evaluated kinetic and photochemical data for atmospheric chemistry: Volume V-heterogeneous reactions on solid substrates, Atmos. Chem. Phys, 10, 9059–9223, https://doi.org/10.5194/acp-10-9059-2010, 2010.

Dassios, K. G. and Pandis, S. N.: The mass accommodation coefficient of ammonium nitrate aerosol, 33, 2993–3003, https://doi.org/10.1016/S1352-2310(99)00079-5, 1999.

Denier van der Gon, H., Gauss, M., Granier, C., Arellano, S., Benedictow, A., Darras, S., Dellaert, S., Guevara, M., Jalkanen, J.-P., Krueger, K., Kuenen, J., Liaskoni, M., Liousse, C., Markova, J., Perez, A. P., Quack, B., Simpson, D., Sindelarova, K., and Soulie, A.: Documentation of CAMS emission inventory products, https://atmosphere.copernicus.eu/node/1054, 2023.

Dentener, F. J., Carmichael, G. R., Zhang, Y., Lelieveld, J., and Crutzen, P. J.: Role of mineral aerosol as a reactive surface in the global troposphere, Journal of Geophysical Research Atmospheres, 101, 22 869–22 889, https://doi.org/10.1029/96jd01818, 1996.

Ek, M. B., Mitchell, K. E., Lin, Y., Rogers, E., Grunmann, P., Koren, V., Gayno, G., and Tarpley, J. D.: Implementation of Noah land surface model advances in the National Centers for Environmental Prediction operational mesoscale Eta model, Journal of Geophysical Research: Atmospheres, 108, 8851, https://doi.org/10.1029/2002JD003296, 2003.

Emanuel, K. A. and Živković Rothman, M.: Development and Evaluation of a Convection Scheme for Use in Climate Models, Journal of the Atmospheric Sciences, 56, 1766 – 1782, https://doi.org/https://doi.org/10.1175/1520-0469(1999)056<1766:DAEOAC>2.0.CO;2, 1999.

Fagerli, H., Tsyro, S., Simpson, D., Schulz, M., Gauss, M., Jonson, J. E., Benedictow, A., Wind, P., Ágnes Nyíri, Steensen, B. M., Valiyaveetil, S., Aas, W., Hjellbrekke, A.-G., Solberg, S., Stebel, K., Tørseth, K., Yttri, K. E., Mareckova, K., Wankmüller, R., Pinterits, M., Ullrich, B., Posch, M., van der Gon, H. D., Alastuey, A., and Theys, N.: Transboundary particulate matter, photo-oxidants, acidifying and eutrophying components. EMEP Status Report 2015., 2015.

Fairlie, T. D., Jacob, D. J., Dibb, J. E., Alexander, B., Avery, M. A., van Donkelaar, A., and Zhang, L.: Impact of mineral dust on nitrate, sulfate, and ozone in transpacific Asian pollution plumes, Atmospheric Chemistry and Physics, 10, 3999–4012, https://doi.org/10.5194/acp-10-3999-2010, 2010.

Feng, Y. and Penner, J. E.: Global modeling of nitrate and ammonium: Interaction of aerosols and tropospheric chemistry, Journal of Geophysical Research Atmospheres, 112, 1–24, https://doi.org/10.1029/2005JD006404, 2007.

Fenter, F. F., Caloz, F., and Rossi, M. J.: Atmospheric, Science Ltd, 29, 3365–3372, 1995.

Ferrier, B. S., Jin, Y., Lin, Y., Black, T., Rogers, E., and Dimego, G.: Implementation of a new grid-scale cloud and precipitation scheme in the NCEP Eta model, 15th Conf. on Numerical Weather Prediction, pp. 280–283, 2002.

Foley, K. M., Roselle, S. J., Appel, K. W., Bhave, P. V., Pleim, J. E., Otte, T. L., Mathur, R., Sarwar, G., Young, J. O., Gilliam, R. C., Nolte, C. G., Kelly, J. T., Gilliland, A. B., and Bash, J. O.: Incremental testing of the Community Multiscale Air Quality (CMAQ) modeling system version 4.7, Geoscientific Model Development, 3, 205–226, https://doi.org/10.5194/gmd-3-205-2010, 2010.

Fountoukis, C. and Nenes, A.: ISORROPIAII: A computationally efficient thermodynamic equilibrium model for K+-Ca2+-Mg2+-NH4+-Na+-SO42–NO3–Cl–H2O aerosols, Atmospheric Chemistry and Physics, 7, 4639–4659, https://doi.org/10.5194/acp-7-4639-2007, 2007.

Ginoux, P., Chin, M., Tegen, I., Prospero, J. M., Holben, B., Dubovik, O., and Lin, S. J.: Sources and distributions of dust aerosols simulated with the GOCART model, Journal of Geophysical Research Atmospheres, 106, 20 255–20 273, https://doi.org/10.1029/2000JD000053, 2001.

Ginoux, P., Prospero, J. M., Gill, T. E., Hsu, N. C., and Zhao, M.: Global-scale attribution of anthropogenic and natural dust sources and their emission rates based on MODIS Deep Blue aerosol products, Reviews of Geophysics, 50, https://doi.org/https://doi.org/10.1029/2012RG000388, 2012.

Gonçalves Ageitos, M., Obiso, V., Miller, R. L., Jorba, O., Klose, M., Dawson, M., Balkanski, Y., Perlwitz, J., Basart, S., Di Tomaso, E., Escribano, J., Macchia, F., Montané, G., Mahowald, N. M., Green, R. O., Thompson, D. R., and Pérez García-Pando, C.: Modeling dust mineralogical composition: sensitivity to soil mineralogy atlases and their expected climate impacts, Atmospheric Chemistry and Physics, 23, 8623–8657, https://doi.org/10.5194/acp-23-8623-2023, 2023.

Goodman, A. L.: A laboratory study of the heterogeneous reaction of nitric acid on calcium carbonate particles, Journal of Geophysical Research Atmospheres, 105, 29 053–29 064, https://doi.org/10.1029/2000JD900396, 2000.

Green, R. O., Mahowald, N. M., Clark, R. N., Ehlmann, B. L., Ginoux, P. A., Kalashnikova, O. V., Miller, R. L., Okin, G., Painter, T. H., Pérez García-Pando, C., Realmuto, V. J., Swayze, G. A., Thompson, D. R., Middleton, E., Guanter, L., Ben Dor, E., and Phillips, B. R.: NASA's Earth Surface Mineral Dust Source Investigation, in: AGU Fall Meeting Abstracts, vol. 2018, pp. A24D–01, 2018.

Guenther, A., Karl, T., Harley, P., Wiedinmyer, C., Palmer, P. I., and Geron, C.: Estimates of global terrestrial isoprene emissions using MEGAN (Model of Emissions of Gases and Aerosols from Nature), Atmospheric Chemistry and Physics, 6, 3181–3210, https://doi.org/10.5194/ACP-6-3181-2006, 2006.

Guerschman, J. P., Scarth, P. F., McVicar, T. R., Renzullo, L. J., Malthus, T. J., Stewart, J. B., Rickards, J. E., and Trevithick, R.: Assessing the effects of site heterogeneity and soil properties when unmixing photosynthetic vegetation, non-

photosynthetic vegetation and bare soil fractions from Landsat and MODIS data, Remote Sensing of Environment, 161, 12–26, https://doi.org/https://doi.org/10.1016/j.rse.2015.01.021, 2015.

Guevara, M., Tena, C., Porquet, M., Jorba, O., and García-Pando, C. P.: HERMESv3, a stand-alone multi-scale atmospheric emission modelling framework-Part 1: Global and regional module, Geoscientific Model Development, 12, 1885–1907, https://doi.org/10.5194/GMD-12-1885-2019, 2019.

Guevara, M., Jorba, O., Tena, C., Denier van der Gon, H., Kuenen, J., Elguindi, N., Darras, S., Granier, C., and Pérez García-Pando, C.: Copernicus Atmosphere Monitoring Service TEMPOral profiles (CAMS-TEMPO): global and European emission temporal profile maps for atmospheric chemistry modelling, Earth System Science Data, 13, 367–404, https://doi.org/10.5194/essd-13-367-2021, 2021.

Guimbaud, C., Arens, F., Gutzwiller, L., Gäggeler, H. W., and Ammann, M.: Uptake of HNO3 to deliquescent sea-salt particles: A study using the short-lived radioactive isotope tracer 13N, Atmospheric Chemistry and Physics, 2, 249–257, https://doi.org/10.5194/acp-2-249-2002, 2002.

Hanisch, F. and Crowley, J. N.: The heterogeneous reactivity of gaseous nitric acid on authentic mineral dust samples, and on individual mineral and clay mineral components, Physical Chemistry Chemical Physics, 3, 2474–2482, https://doi.org/10.1039/b101700o, 2001.

Hanisch, F. and Crowley, J. N.: Heterogeneous reactivity of NO and HNO3 on mineral dust in the presence of ozone, Physical Chemistry Chemical Physics, 5, 883–887, https://doi.org/10.1039/b211503d, 2003.

Hauglustaine, D. A., Balkanski, Y., and Schulz, M.: A global model simulation of present and future nitrate aerosols and their direct radiative forcing of climate, Atmospheric Chemistry and Physics, 14, 11 031–11 063, https://doi.org/10.5194/acp-14-11031-2014, 2014.

Herich, H., Tritscher, T., Wiacek, A., Gysel, M., Weingartner, E., Lohmann, U., Baltensperger, U., and Cziczo, D. J.: Water uptake of clay and desert dust aerosol particles at sub- and supersaturated water vapor conditions, Physical Chemistry Chemical Physics, 11, 7804–7809, https://doi.org/10.1039/b901585j, 2009.

Hersbach, H., Bell, B., Berrisford, P., Biavati, G., Horányi, A., Muñoz Sabater, J., Nicolas, J., Peubey, C., Radu, R., Rozum, I., Schepers, D., Simmons, A., Soci, C., Dee, D., and Thépaut, J.-N.: ERA5 hourly data on single levels from 1940 to present, https://doi.org/10.24381/cds.adbb2d47, [Online; accessed 11 March 2024], 2023.

Hodzic, A., Bessagnet, B., and Vautard, R.: A model evaluation of coarse-mode nitrate heterogeneous formation on dust particles, Atmospheric Environment, 40, 4158–4171, https://doi.org/10.1016/j.atmosenv.2006.02.015, 2006.

Hsu, N. C., Tsay, S.-C., King, M. D., and Herman, J. R.: Aerosol properties over bright-reflecting source regions, IEEE Transactions on Geoscience and Remote Sensing, 42, 557–569, https://doi.org/10.1109/TGRS.2004.824067, 2004.

Iacono, M. J., Delamere, J. S., Mlawer, E. J., Shephard, M. W., Clough, S. A., and Collins, W. D.: Radiative forcing by long-lived greenhouse gases: Calculations with the AER radiative transfer models, Journal of Geophysical Research: Atmospheres, 113, 13 103, https://doi.org/10.1029/2008JD009944, 2008.

Jacob, D. J.: Heterogeneous chemistry and tropospheric ozone, 2000.

Jaeglé, L., Quinn, P. K., Bates, T. S., Alexander, B., and Lin, J. T.: Global distribution of sea salt aerosols: New constraints from in situ and remote sensing observations, Atmospheric Chemistry and Physics, 11, 3137–3157, https://doi.org/10.5194/ACP-11-3137-2011, 2011.

Janjic, Z.: Nonlinear Advection Schemes and Energy Cascade on Semi-Staggered Grids, AMS, https://doi.org/https://doi.org/10.1175/1520-0493(1984)112<1234:NASAEC>2.0.CO;2, 1984.

Janjic, Z. and Gall, R.: Scientific Documentation of the NCEP Nonhydrostatic Multiscale Model on the B grid (NMMB). Part 1 Dynamics, http://www.ucar.edu/library/collections/technotes/technotes.jsp, 2012.

Janjic, Z. I.: The Mellor-Yamada level 2.5 turbulence closure scheme in the NCEP Eta Model, World Meteorological Organization-Publications-WMO TD, pp. 4–14, 1996.

Janjić, Z. I.: Comments on "Development and Evaluation of a Convection Scheme for Use in Climate Models", Journal of the Atmospheric Sciences, 57, 3686 – 3686, https://doi.org/https://doi.org/10.1175/1520-0469(2000)057<3686:CODAEO>2.0.CO;2, 2000.

Janjić, Z. I.: Nonsingular Implementation of the Mellor-Yamada Level 2.5 Scheme in the NCEP Meso model, 2001.

Jones, A. C., Hill, A., Remy, S., Abraham, N. L., Dalvi, M., Hardacre, C., Hewitt, A. J., Johnson, B., Mulcahy, J. P., and Turnock, S. T.: Exploring the sensitivity of atmospheric nitrate concentrations to nitric acid uptake rate using the Met Office ' s Unified Model, Atmospheric Chemistry and Physics, 21, 1–48, https://doi.org/10.5194/acp-21-15901-2021, 2021.

Jorba, O., Dabdub, D., Blaszczak-Boxe, C., Pérez, C., Janjic, Z., Baldasano, J. M., Spada, M., Badia, A., and Gonçalves, M.: Potential significance of photoexcited NO2 on global air quality with the NMMB/BSC chemical transport model, Journal of Geophysical Research: Atmospheres, 117, 13 301, https://doi.org/10.1029/2012JD017730, 2012.

Jordan, C. E., Dibb, J. E., Anderson, B. E., and Fuelberg, H. E.: Uptake of nitrate and sulfate on dust aerosols during TRACE-P, 108, https://doi.org/10.1029/2002JD003101, 2003.

Journet, E., Balkanski, Y., and Harrison, S. P.: A new data set of soil mineralogy for dust-cycle modeling, Atmospheric Chemistry and Physics, 14, 3801–3816, https://doi.org/10.5194/ACP-14-3801-2014, 2014.

Kaiser, J. W., Heil, A., Andreae, M. O., Benedetti, A., Chubarova, N., Jones, L., Morcrette, J.-J., Razinger, M., Schultz, M. G., Suttie, M., and Werf, G. R. V. D.: Biomass burning emissions estimated with a global fire assimilation system based on observed fire radiative power, Biogeosciences, 9, 527–554, https://doi.org/10.5194/bg-9-527-2012, 2012.

Karydis, V. A., Tsimpidi, A. P., Pozzer, A., Astitha, M., and Lelieveld, J.: Effects of mineral dust on global atmospheric nitrate concentrations, Atmospheric Chemistry and Physics, 16, 1491–1509, https://doi.org/10.5194/acp-16-1491-2016, 2016.

Karydis, V. A., Tsimpidi, A. P., Pozzer, A., and Lelieveld, J.: How alkaline compounds control atmospheric aerosol particle acidity, Atmos. Chem. Phys, 21, 14 983–15 001, https://doi.org/10.5194/acp-21-14983-2021, 2021.

Klose, M., Jorba, O., Ageitos, M. G., Escribano, J., Dawson, M. L., Obiso, V., Tomaso, E. D., Basart, S., Pinto, G. M., Macchia, F., Ginoux, P., Guerschman, J., Prigent, C., Huang, Y., Kok, J. F., Miller, R. L., and García-Pando, C. P.: Mineral dust cycle in the Multiscale Online Nonhydrostatic AtmospheRe CHemistry model (MONARCH) Version 2.0, Geosci. Model Dev, 14, 6403–6444, https://doi.org/10.5194/gmd-14-6403-2021, 2021.

Krueger, B. J., Grassian, V. H., Laskin, A., and Cowin, J. P.: The transformation of solid atmospheric particles into liquid droplets through heterogeneous chemistry: Laboratory insights into the processing of calcium containing mineral dust aerosol in the troposphere, Geophysical Research Letters, 30, 1148, https://doi.org/10.1029/2002GL016563, 2003.

Krueger, B. J., Grassian, V. H., Cowin, J. P., and Laskin, A.: Heterogeneous chemistry of individual mineral dust particles from different dust source regions: The importance of particle mineralogy, Atmospheric Environment, 38, 6253–6261, https://doi.org/10.1016/j.atmosenv.2004.07.010, 2004.

Lana, A., Bell, T. G., Simó, R., Vallina, S. M., Ballabrera-Poy, J., Kettle, A. J., Dachs, J., Bopp, L., Saltzman, E. S., Stefels, J., Johnson, J. E., and Liss, P. S.: An updated climatology of surface dimethlysulfide concentrations and emission fluxes in the global ocean, Global Biogeochem. Cycles, p. 1004, https://doi.org/10.1029/2010GB003850, 2011.

Li, J., Wang, Z., Zhuang, G., Luo, G., Sun, Y., and Wang, Q.: Mixing of Asian mineral dust with anthropogenic pollutants over East Asia: A model case study of a super-duststorm in March 2010, Atmospheric Chemistry and Physics, 12, 7591–7607, https://doi.org/10.5194/acp-12-7591-2012, 2012.

Li, W. J. and Shao, L. Y.: Observation of nitrate coatings on atmospheric mineral dust particles, Atmospheric Chemistry and Physics, 9, 1863–1871, https://doi.org/10.5194/acp-9-1863-2009, 2009.

Li, X., Yu, Z., Yue, M., Liu, Y., Huang, K., Chi, X., Nie, W., Ding, A., Dong, X., and Wang, M.: Impact of mineral dust photocatalytic heterogeneous chemistry on the formation of the sulfate and nitrate: A modelling study over East Asia, 316, 120 166, https://doi.org/10.1016/j.atmosenv.2023.120166, 2024.

Li, Y., Schichtel, B. A., Walker, J. T., Schwede, D. B., Chen, X., Lehmann, C. M., Puchalski, M. A., Gay, D. A., and Collett, J. L.: Increasing importance of deposition of reduced nitrogen in the United States, Proceedings of the National Academy of Sciences of the United States of America, 113, 5874–5879, https://doi.org/10.1073/pnas.1525736113, 2016.

Liao, H., Adams, P. J., Chung, S. H., Seinfeld, J. H., Mickley, L. J., and Jacob, D. J.: Interactions between tropospheric chemistry and aerosols in a unified general circulation model, Journal of Geophysical Research: Atmospheres, 108, https://doi.org/10.1029/2001jd001260, 2003.

Liu, T. and Abbatt, J. P. D.: Oxidation of sulfur dioxide by nitrogen dioxide accelerated at the interface of deliquesced aerosol particles, Nature Chemistry 2021, pp. 1–5, https://doi.org/10.1038/s41557-021-00777-0, 2021.

Liu, Y., P., C. J., Wang, H., and Laskin, A.: Kinetic Study of Heterogeneous Reaction of Deliquesced NaCl Particles with Gaseous HNO 3, J. Phys. Chem. A, 111, 10 026–10 043, 2007.

Liu, Y., Gibson, E. R., Cain, J. P., Wang, H., Grassian, V. H., and Laskin, A.: Kinetics of heterogeneous reaction of CaCO3 particles with gaseous HNO3 over a wide range of humidity, Journal of Physical Chemistry A, 112, 1561–1571, https://doi.org/10.1021/jp076169h, 2008.

Liu, Y., Zhan, J., Zheng, F., Song, B., Zhang, Y., Ma, W., Hua, C., Xie, J., Bao, X., Yan, C., Bianchi, F., Petäjä, T., Ding, A., Song, Y., He, H., and Kulmala, M.: Dust emission reduction enhanced gas-to-particle conversion of ammonia in the North China Plain, Nature Communications, 13, https://doi.org/10.1038/s41467-022-34733-4, 2022.

Luo, G., Yu, F., and Schwab, J.: Revised treatment of wet scavenging processes dramatically improves GEOS-Chem 12.0.0 simulations of surface nitric acid, nitrate, and ammonium over the United States, Geoscientific Model Development, 12, 3439–3447, https://doi.org/10.5194/gmd-12-3439-2019, 2019.

Lurmann, F. W., Wexler, A. S., Pandis, S. N., Musarra, S., Kumar, N., and Seinfeld, J. H.: Modelling urban and regional aerosols—II. Application to California's South Coast Air Basin, Atmospheric Environment, 31, 2695–2715, https://doi.org/10.1016/S1352-2310(97)00100-3, 1997.

Ma, Q., Zhong, C., Ma, J., Ye, C., Zhao, Y., Liu, Y., Zhang, P., Chen, T., Liu, C., Chu, B., and He, H.: Comprehensive Study about the Photolysis of Nitrates on Mineral Oxides, Environmental Science and Technology, 55, 8604–8612, https://doi.org/10.1021/ACS.EST.1C02182/SUPPL_FILE/ES1C02182_SI_001.PDF, 2021.

Mahowald, N., Albani, S., Kok, J. F., Engelstaeder, S., Scanza, R., Ward, D. S., and Flanner, M. G.: The size distribution of desert dust aerosols and its impact on the Earth system, Aeolian Research, 15, 53–71, https://doi.org/10.1016/j.aeolia.2013.09.002, 2014.

Mashburn, C. D., Frinak, E. K., and Tolbert, M. A.: Heterogeneous uptake of nitric acid on Na-montmorillonite clay as a function of relative humidity, Journal of Geophysical Research Atmospheres, 111, https://doi.org/10.1029/2005JD006525, 2006.

Meng, Z. and Seinfeld, J. H.: Time scales to achieve atmospheric gas-aerosol equilibrium for volatile species, Atmospheric Environment, 30, 2889–2900, https://doi.org/10.1016/1352-2310(95)00493-9, 1996.

Metzger, S., Dentener, F., Pandis, S., and Lelieveld, J.: Gas/aerosol partitioning: 1. A computationally efficient model, 107, 4312, https://doi.org/10.1029/2001JD001102, 2002.

Milousis, A., Tsimpidi, A. P., Tost, H., Pandis, S. N., Nenes, A., Kiendler-Scharr, A., and Karydis, V. A.: Implementation of the ISORROPIA-lite aerosol thermodynamics model into the EMAC chemistry climate model (based on MESSy v2.55): implications for aerosol composition and acidity, Geoscientific Model Development, 17, 1111–1131, https://doi.org/10.5194/gmd-17-1111-2024, 2024.

Monin, A. S. and Obukhov, A. M.: Basic laws of turbulent mixing in the surface layer of the atmosphere, 1954.

Myhre, G., Grini, A., and Metzger, S.: Modelling of nitrate and ammonium-containing aerosols in presence of sea salt, Atmospheric Chemistry and Physics, 6, 4809–4821, https://doi.org/10.5194/acp-6-4809-2006, 2006.

Möhler, O., Field, P. R., Connolly, P., Benz, S., Saathoff, H., Schnaiter, M., Wagner, R., Cotton, R., Krämer, M., Mangold, A., and Heymsfield, A. J.: Efficiency of the deposition mode ice nucleation on mineral dust particles, www.atmos-chem-phys.net/6/3007/2006/, 2006.

Navarro-Barboza, H., Pandolfi, M., Guevara, M., Enciso, S., Tena, C., Via, M., Yus-Díez, J., Reche, C., Pérez, N., Alastuey, A., Querol, X., and Jorba, O.: Uncertainties in source allocation of carbonaceous aerosols in a Mediterranean region, Environment International, 183, 108 252, https://doi.org/10.1016/j.envint.2023.108252, 2024.

Nenes, A., Pandis, S. N., and Pilinis, C.: ISORROPIA: A New Thermodynamic Equilibrium Model for Multiphase Multicomponent Inorganic Aerosols, Aquatic Geochemistry 1998 4:1, 4, 123–152, https://doi.org/10.1023/A:1009604003981, 1998.

Pai, S., Heald, C., Pierce, J., Farina, S., Marais, E., Jimenez, J., Campuzano-Jost, P., Nault, B., Middlebrook, A., Coe, H., Shilling, J., Bahreini, R., Dingle, J., and Vu, K.: An evaluation of global organic aerosol schemes using airborne observations, An evaluation of global organic aerosol schemes using airborne observations, pp. 1–39, https://doi.org/10.5194/acp-2019-331, 2019.

Pai, S. J., Heald, C. L., Pierce, J. R., Farina, S. C., Marais, E. A., Jimenez, J. L., Campuzano-Jost, P., Nault, B. A., Middlebrook, A. M., Coe, H., Shilling, J. E., Bahreini, R., Dingle, J. H., and Vu, K.: An evaluation of global organic aerosol schemes using airborne observations, Atmospheric Chemistry and Physics, 20, 2637–2665, https://doi.org/10.5194/acp-20-2637-2020, 2020.

Paulot, F., Ginoux, P., Cooke, W. F., Donner, L. J., Fan, S., Lin, M.-Y., Mao, J., Naik, V., and Horowitz, L. W.: Sensitivity of nitrate aerosols to ammonia emissions and to nitrate chemistry: implications for present and future nitrate optical depth, Atmos. Chem. Phys, 16, 1459–1477, https://doi.org/10.5194/acp-16-1459-2016, 2016.

Phadnis, M. J. and Carmichael, G. R.: Numerical investigation of the influence of mineral dust on the tropospheric chemistry of east Asia, Journal of Atmospheric Chemistry, 36, 285–323, https://doi.org/10.1023/A:1006391626069, 2000.

Pratte, P. and Rossi, M. J.: Nitric acid uptake on NaCl and sea salt aerosol at relative humidities in the range 2 . 8 to 25 1–22, https://doi.org/10.13140/2.1.2053.4562, 2006.

Prince, A. P., Kleiber, P., Grassian, V. H., and Young, M. A.: Heterogeneous interactions of calcite aerosol with sulfur dioxide and sulfur dioxide–nitric acid mixtures, Physical Chemistry Chemical Physics, 9, 3432–3439, https://doi.org/10.1039/B703296J, 2007.

Pringle, K. J., Tost, H., Message, S., Steil, B., Giannadaki, D., Nenes, A., Fountoukis, C., Stier, P., Vignati, E., and Lelieveld, J.: Description and evaluation of GMXe: A new aerosol submodel for global simulations (v1), Geoscientific Model Development, 3, 391–412, https://doi.org/10.5194/gmd-3-391-2010, 2010.

Pérez, C., Haustein, K., Janjic, Z., Jorba, O., Huneeus, N., Baldasano, J. M., Black, T., Basart, S., Nickovic, S., Miller, R. L., Perlwitz, J. P., Schulz, M., and Thomson, M.: Atmospheric dust modeling from meso to global scales with the online NMMB/BSC-Dust model ndash; Part 1: Model description, annual simulations and evaluation, Atmospheric Chemistry and Physics, 11, 13 001–13 027, https://doi.org/10.5194/acp-11-13001-2011, 2011.

Randall, D., Artaxo, P., Bretherton, C., Feingold, G., Forster, P., m Kerminen, V., Kondo, Y., Liao, H., Lohmann, U., Rasch, P., Satheesh, S., Sherwood, S., Stevens, B., Zhang, X., Qin, D., k Plattner, G., Tignor, M., Allen, S., Boschung, J., Nauels, A., Xia, Y., Bex, V., Midgley, P., Boucher, O., and Randall, D.: Clouds and Aerosols. In: Climate Change 2013: The Physical Science Basis. Contribution of Working

Group I to the Fifth Assessment Report of the Intergovernmental Panel on Climate Change Coordinating Lead Authors: Lead Authors, 2013.

Raupach, M. R., Gillette, D. A., and Leys, J. F.: The effect of roughness elements on wind erosion threshold, Journal of Geophysical Research: Atmospheres, 98, 3023–3029, https://doi.org/https://doi.org/10.1029/92JD01922, 1993.

Rea, D. K.: The paleoclimatic record provided by eolian deposition in the deep sea: The geologic history of wind, Reviews of Geophysics, 32, 159–195, https://doi.org/10.1029/93RG03257, 1994.

Riemer, N., Vogel, H., Vogel, B., Schell, B., Ackermann, I., Kessler, C., and Hass, H.: Impact of the heterogeneous hydrolysis of N2O5 on chemistry and nitrate aerosol formation in the lower troposphere under photosmog conditions, Journal of Geophysical Research: Atmospheres, 108, 4144, https://doi.org/10.1029/2002JD002436, 2003.

Riemer, N., Ault, A. P., West, M., Craig, R. L., and Curtis, J. H.: Aerosol Mixing State: Measurements, Modeling, and Impacts, Reviews of Geophysics, 57, 187–249, https://doi.org/10.1029/2018RG000615, 2019.

Rémy, S., Kipling, Z., Flemming, J., Boucher, O., Nabat, P., Michou, M., Bozzo, A., Ades, M., Huijnen, V., Benedetti, A., Engelen, R., Peuch, V.-H., and Morcrette, J.-J.: Description and evaluation of the tropospheric aerosol scheme in the European Centre for Medium-Range Weather Forecasts (ECMWF) Integrated Forecasting System (IFS-AER, cycle 45R1), Geoscientific Model Development, 12, 4627–4659, https://doi.org/10.5194/gmd-12-4627-2019, 2019.

Rémy, S., Kipling, Z., Huijnen, V., Flemming, J., Nabat, P., Michou, M., Ades, M., Engelen, R., and Peuch, V. H.: Description and evaluation of the tropospheric aerosol scheme in the Integrated Forecasting System (IFS-AER, cycle 47R1) of ECMWF, Geoscientific Model Development, 15, 4881–4912, https://doi.org/10.5194/gmd-15-4881-2022, 2022.

Saul, T. D., Tolocka, M. P., and Johnston, M. V.: Reactive uptake of nitric acid onto sodium chloride aerosols across a wide range of relative humidities, Journal of Physical Chemistry A, 110, 7614–7620, https://doi.org/10.1021/jp060639a, 2006.

Schwartz, S. E.: Mass-Transport Considerations Pertinent to Aqueous Phase Reactions of Gases in Liquid-Water Clouds, pp. 415–471, Springer Berlin Heidelberg, 1986.

Seinfeld, J. and Pandis, S.: Atmospheric Chemistry and Physics: From Air Pollution to Climate Change. 2nd Edition,, https://www.scirp.org/reference/ReferencesPapers?ReferenceID=1345321, 2006.

Seinfeld, J. H. and Pandis, S. N.: Atmospheric Chemistry and Physics: From Air Pollution to Climate Change, Environment: Science and Policy for Sustainable Development, 40, 26–26, https://doi.org/10.1080/00139157.1999.10544295, 1998.

Semeniuk, K. and Dastoor, A.: Current state of atmospheric aerosol thermodynamics and mass transfer modeling: A review, Atmosphere, 11, 1–71, https://doi.org/10.3390/atmos11020156, 2020.

Song, C. H. and Carmichael, G. R.: A three-dimensional modeling investigation of the evolution processes of dust and sea-salt particles in east Asia, Journal of Geophysical Research Atmospheres, 106, 18 131–18 154, https://doi.org/10.1029/2000JD900352, 2001.

Song, C. H., Kim, C. M., Lee, Y. J., Carmichael, G. R., Lee, B. K., and Lee, D. S.: An evaluation of reaction probabilities of sulfate and nitrate precursors onto East Asian dust particles, J. Geophys. Res, 112, 18 206, https://doi.org/10.1029/2006JD008092, 2007.

Song, S., Gao, M., Xu, W., Shao, J., Shi, G., Wang, S., Wang, Y., Sun, Y., and McElroy, M. B.: Fine-particle pH for Beijing winter haze as inferred from different thermodynamic equilibrium models, Atmospheric Chemistry and Physics, 18, 7423–7438, https://doi.org/10.5194/acp-18-7423-2018, 2018.

Soulie, A., Granier, C., Darras, S., Zilbermann, N., Doumbia, T., Guevara, M., Jalkanen, J. P., Keita, S., Liousse, C., Crippa, M., Guizzardi, D., Hoesly, R., and Smith, S. J.: Global anthropogenic emissions (CAMS-GLOB-ANT) for the Copernicus Atmosphere Monitoring Service

simulations of air quality forecasts and reanalyses, Earth System Science Data, 16, 2261–2279, https://doi.org/10.5194/ESSD-16-2261-2024, 2024.

Sousse, R.: "A Comprehensive Global Modelling Assessment of Nitrate Heterogeneous Formation on Desert Dust":Column loads monthly means per species., https://doi.org/10.5281/zenodo.12789730, 2024.

Spada, M.: Development and Evaluation of an Atmospheric Aerosol Module Implemented Within the Nmmb/Bsc-Ctm Michele Spada Phd Thesis 2015, 2015.

Spada, M., Jorba, O., García-Pando, C. P., Janjic, Z., and Baldasano, J. M.: Modeling and evaluation of the global sea-salt aerosol distribution: Sensitivity to emission schemes and resolution effects at coastal/orographic sites, Atmospheric Chemistry and Physics, 13, 11 735–11 755, https://doi.org/10.5194/ACP-13-11735-2013, 2013.

Sulprizio, M.: Chemistry instability introduced by ISORROPIA v2.2, http://wiki.seas.harvard.edu/geos-chem/index.php/ISORROPIA_II#Chemistry_instability_introduced_by_ISORROPIA_v2.2, 2022.

Suman, A., Zanini, N., Vulpio, A., and Pinelli, M.: Apparatus and methods for the calibration and correction of a polydispersed dust feeding system applied in multiphase flow experiments, Experimental Thermal and Fluid Science, 151, 111 074, https://doi.org/https://doi.org/10.1016/j.expthermflusci.2023.111074, 2024.

Thompson, D., Green, R., Bradley, C., Brodrick, P., Mahowald, N., Ben-Dor, E., Bennett, M., Bernas, M., Carmon, N., Chadwick, K. D., Clark, R., Coleman, R., Cox, E., Diaz, E., Eastwood, M., Eckert, R., Ehlmann, B., Ginoux, P., Gonçalves Ageitos, M., and Zandbergen, S.: On-orbit calibration and performance of the EMIT imaging spectrometer, Remote Sensing of Environment, 303, 113 986, https://doi.org/10.1016/j.rse.2023.113986, 2024.

Tolocka, M. P., Saul, T. D., and Johnston, M. V.: Reactive Uptake of Nitric Acid into Aqueous Sodium Chloride Droplets Using Real-Time Single-Particle Mass Spectrometry, Journal of Physical Chemistry A, 108, 2659–2665, https://doi.org/10.1021/jp036612y, 2004.

Trump, E. R., Fountoukis, C., Donahue, N. M., and Pandis, S. N.: Improvement of simulation of fine inorganic PM levels through better descriptions of coarse particle chemistry, Atmospheric Environment, 102, 274–281, https://doi.org/10.1016/j.atmosenv.2014.11.059, 2015.

Uno, I., Wang, Z., Itahashi, S., Yumimoto, K., Yamamura, Y., Yoshino, A., Takami, A., Hayasaki, M., and Kim, B.-G. G.: Paradigm shift in aerosol chemical composition over regions downwind of China, Scientific Reports, 10, 1–11, https://doi.org/10.1038/s41598-020-63592-6, 2020.

Usher, C. R., Al-Hosney, H., Carlos-Cuellar, S., and Grassian, V. H.: A laboratory study of the heterogeneous uptake and oxidation of sulfur dioxide on mineral dust particles, Journal of Geophysical Research: Atmospheres, 107, https://doi.org/10.1029/2002JD002051, 2002.

Usher, C. R., Michel, A. E., and Grassian, V. H.: Reactions on Mineral Dust, Chemical Reviews, 103, 4883–4939, https://doi.org/10.1021/cr020657y, 2003.

Vignati, E., Wilson, J., and Stier, P.: M7: An efficient size-resolved aerosol microphysics module for large-scale aerosol transport models, Journal of Geophysical Research D: Atmospheres, 109, 1–17, https://doi.org/10.1029/2003JD004485, 2004.

Vlasenko, A., Sjogren, S., Weingartner, E., Stemmler, K., Gäggeler, H. W., and Ammann, M.: Atmospheric Chemistry and Physics Effect of humidity on nitric acid uptake to mineral dust aerosol particles, www.atmos-chem-phys.net/6/2147/2006/, 2006.

Vlasenko, A., Huthwelker, T., Gäggeler, H. W., and Ammann, M.: Kinetics of the heterogeneous reaction of nitric acid with mineral dust particles: An aerosol flowtube study, Physical Chemistry Chemical Physics, 11, 7921–7930, https://doi.org/10.1039/b904290n, 2009.

Wang, Z., Pan, X., Uno, I., Li, J., Wang, Z., Chen, X., Fu, P., Yang, T., Kobayashi, H., Shimizu, A., Sugimoto, N., and Yamamoto, S.: Significant impacts of heterogeneous reactions on the chemical composition and mixing state of dust particles: A case study during dust events over northern China, Atmospheric Environment, 159, 83–91, https://doi.org/10.1016/j.atmosenv.2017.03.044, 2017.

Wei, C.: Modeling the effects of heterogeneous reactions on atmospheric Modeling the effects of heterogeneous reactions on atmospheric chemistry and aerosol properties chemistry and aerosol properties, https://doi.org/10.17077/etd.2xewzpnz, 2010.

Wesely, M.: Parameterization of surface resistances to gaseous dry deposition in regional-scale numerical models, Atmospheric Environment (1967), 23, 1293–1304, https://doi.org/https://doi.org/10.1016/0004-6981(89)90153-4, 1989.

Wexler, A. S. and Seinfeld, J. H.: The distribution of ammonium salts among a size and composition dispersed aerosol, 24, 1231–1246, https://doi.org/10.1016/0960-1686(90)90088-5, 1990.

Whitten, G. Z., Heo, G., Kimura, Y., McDonald-Buller, E., Allen, D. T., Carter, W. P., and Yarwood, G.: A new condensed toluene mechanism for Carbon Bond: CB05-TU, Atmospheric Environment, 44, 5346–5355, https://doi.org/10.1016/J.ATMOSENV.2009.12.029, 2010.

Wild, O., Zhu, X., and Prather, M. J.: Fast-J: Accurate Simulation of In- and Below-Cloud Photolysis in Tropospheric Chemical Models, Journal of Atmospheric Chemistry 2000 37:3, 37, 245–282, https://doi.org/10.1023/A:1006415919030, 2000.

Yarwood, G., Rao, S., Yocke, M., and Whitten, G. Z.: UPDATES TO THE CARBON BOND CHEMICAL MECHANISM: CB05, https://camx-wp.azurewebsites.net/Files/CB05_Final_Report_120805.pdf, 2005.

Yu, Z., Jang, M., and Park, J.: Modeling atmospheric mineral aerosol chemistry to predict heterogeneous photooxidation of SO₂, 17, 10 001–10 017, https://doi.org/10.5194/acp-17-10001-2017, 2017.

Yue, Y., Cheng, J., Lee, K. S., Stocker, R., He, X., Yao, M., and Wang, J.: Effects of relative humidity on heterogeneous reaction of SO2 with CaCO3 particles and formation of CaSO4·2H2O crystal as secondary aerosol, Atmospheric Environment, 268, https://doi.org/10.1016/J.ATMOSENV.2021.118776, 2022.

Zakoura, M. and Pandis, S. N.: Overprediction of aerosol nitrate by chemical transport models: The role of grid resolution, Atmospheric Environment, 187, 390–400, https://doi.org/10.1016/j.atmosenv.2018.05.066, 2018.

Zaveri, R. A., Easter, R. C., Fast, J. D., and Peters, L. K.: Model for Simulating Aerosol Interactions and Chemistry (MOSAIC), Journal of Geophysical Research Atmospheres, 113, 1–29, https://doi.org/10.1029/2007JD008782, 2008.

Zaveri, R. A., Easter, R. C., Singh, B., Wang, H., Lu, Z., Tilmes, S., Emmons, L. K., Vitt, F., Zhang, R., Liu, X., Ghan, S. J., and Rasch, P. J.: Development and Evaluation of Chemistry-Aerosol-Climate Model CAM5-Chem-MAM7-MOSAIC: Global Atmospheric Distribution and Radiative Effects of Nitrate Aerosol, Journal of Advances in Modeling Earth Systems, 13, https://doi.org/10.1029/2020MS002346, 2021.

Zhai, S., Jacob, D. J., Pendergrass, D. C., Colombi, N. K., Shah, V., Yang, L. H., Zhang, Q., Wang, S., Kim, H., Sun, Y., Choi, J.-S., Park, J.-S., Luo, G., Yu, F., Woo, J.-H., Kim, Y., Dibb, J. E., Lee, T., Han, J.-S., Anderson, B. E., Li, K., and Liao, H.: Coarse particulate matter air quality in East Asia: implications for fine particulate nitrate, 23, 4271–4281, https://doi.org/10.5194/acp-23-4271-2023, publisher: Copernicus GmbH, 2023.

Zilitinkevich, S. S.: Bulk characteristics of turbulence in the atmospheric planetary boundary layer, vol. 167, Trudy GGO, 1965.